# UNIVERSITY OF SOUTHAMPTON

FACULTY OF PHYSICAL SCIENCES AND ENGINEERING

Electronics and Computer Science

# Screen-printed free-standing structures on textile and flexible substrate

by

**Nursabirah Jamel**

Thesis for the degree of Doctor of Philosophy

August 2017

UNIVERSITY OF SOUTHAMPTON

# ABSTRACT

FACULTY OF PHYSICAL SCIENCES AND ENGINEERING

ELECTRONICS AND COMPUTER SCIENCE

Doctor of Philosophy

## SCREEN-PRINTED FREE-STANDING STRUCTURES ON TEXTILE AND FLEXIBLE SUBSTRATE

By Nursabirah Jamel

This thesis had demonstrated free-standing structures fabricated solely using screen-printing technique on textile and flexible substrate. Since the screen-printing method provides more flexibility in terms of design and fabrication, this method was employed as a method of choice for the fabrication process compared to knitting and weaving techniques. This thesis is intended to explore the fabrication of small scale (tens of microns to mm) three dimensional (3D) structures using standard printing process and the application of the 3D printing process on three different structures.

This research investigated in detail the comparison between two different removal sacrificial material which are thermal and water removed sacrificial materials. Both of these sacrificial materials are compatible with textile as the temperature process is lower than 200°C and the solvents used are not corrosive which will not alter the properties of the textile. However, because thermal sacrificial material has ragged edges and reacts with the structural layer, the water removed sacrificial layer is selected. The water removed sacrificial material is based on polyvinyl alcohol (PVA) and can be cured at 80°C for 3 minutes, providing a solid foundation for subsequent printed layers. This sacrificial layer can be removed in 90°C agitate water to form free-standing structure. Minico M 7000 Blue A is the thermally cured structural material used with the sacrificial material. The Minico had the highest mechanical properties (5523 MPa) compared to another four structural materials. This is important as this layer is the main structure of the design. Hence, the stiffest material will provide the most durable free-standing structure. The feasibility of the screen-printing process on textile had been demonstrated by fabricating three different free-standing structures which are cantilever, encastre beam and diaphragm structure. The cantilever structure was demonstrated as energy harvesting application on textile with power output of 27.9 nW excited at frequency of 201 Hz. A printed encastre beam was tested on one side of piezoelectric elements using the electromechanical shaker and the maximum output generated was 0.1545 volt at natural frequency of 3.835 kHz had also been demonstrated. The final structure which is the free-standing diaphragm was evaluated and had successfully demonstrated the sound pressure level of 74 decibel between 12 kHz to 19 kHz with 15mm microphone distance from circular diaphragm structure. These applications are the first of its kind being reported and fabricated directly on textile and flexible substrate.

# Contents

# List of tables

# List of figures

# DECLARATION OF AUTHORSHIP

I, Nursabirah Jamel declare that the thesis entitled '**Screen-printed free-standing structures on textile and flexible substrate**' and the work presented in the thesis are both my own, and have been generated by me as the result of my own original research. I confirm that:

- this work was done wholly or mainly while in candidature for a research degree at this University;
- where any part of this thesis has previously been submitted for a degree or any other qualification at this University or any other institution, this has been clearly stated;
- where I have consulted the published work of others, this is always clearly attributed;
- where I have quoted from the work of others, the source is always given. With the exception of such quotations, this thesis is entirely my own work;
- I have acknowledged all main sources of help;
- where the thesis is based on work done by myself jointly with others, I have made clear exactly what was done by others and what I have contributed myself;
- none of this work has been published before submission, or [delete as appropriate] parts of this work have been published as: [please list references]

Signed: ..........................................................................

Date:.........17 August 2017............................................................

# Acknowledgements

Alhamdulillah, I thank God Almighty, who has sustained me through these, the best and the toughest years of my life, and without which I had lost. I would also like to express my sincere gratitude and appreciation to Prof. Steve P Beeby and Dr John Tudor for their endless guidance and encouragement throughout my PhD process. I am greatly in debt to both of your effort and expertise since the beginning of my journey.

I gratefully acknowledge the contribution of Dr Russel Torah and Dr Kai Yang for showing and training me all the equipment in PrintLab; Dr Dibin Zhu and Dr Ahmed Al-mussalam for allowing me to use the shaker and poling rig for sample characterisation.

I would like to thank the University Malaysia Perlis (UniMaP) and Ministry of Higher Education Malaysia for the opportunity and scholarship award to purse this PhD.

Special thanks to my fellow colleagues, Joseph, Komolafe, Yi, Yang, Zhuo, Yi2,Gordan, HuiHui, Poy, Sangchai, Zeeshan, Mark, Monika, Malaysian communities and members in Smart fabric and ECS group, who have been involved directly and indirectly in my PhD and making the journey enjoyable.

Finally and most importantly, my special appreciations goes to my parents; Prof. Jamel Ariffin, Hjh. Ku Faizah Ku Ahmad, Hj. Md Salleh Abdul Wahab and Hjh. Zaharah Man, and family members especially my husband, Dr Ahmad Fakhruddin Md Salleh for the encouragement, understanding, love and all the supports given throughout the journey. To my daughters, Ayra Harlyna and Hana Zahra thank you for always being there and understand ibu’s work. For my family and my children, I dedicated this thesis for you.

Thank you very much.

Nursabirah Jamel
Southampton, 2017.

# Abbreviations

| | |
|---|---|
| **3D** | Three dimensional |
| **1M2P** | 1-methyl-2-pyrolidone |
| **2D** | Two dimensional |
| **CVD** | Chemical vapour deposition |
| **E-textile** | Electronic textile |
| **E-yarn** | Electronic yarns |
| **FEM** | Finite element modelling |
| **GBL** | Gamma-butyrolacton |
| **HCl** | Hydrochloric-acid |
| **HF** | Hydrofluoric-acid |
| **IC** | Integrated circuits |
| **ICD+** | Industrial Clothing Division Plus |
| **IDT** | Interdigitated |
| **IPA** | Isopropyl alcohol |
| **LED** | Light emitting diodes |
| **LPCVD** | low pressure chemical vapour deposition |
| **LTCC** | Low Temperature Cofired Ceramic |
| **MEK** | Methyl-ethyl ketone |
| **MEMS** | Micro Electro Mechanical system |
| **NNDMAA** | N,N-Dimenthylacetamide |
| **PAA** | Poly(acrylic acid) |
| **PAN** | Personal area network |
| **PEC** | Poly(ethylene) carbonat |
| **PET** | Polyethylene terephthalate |
| **PGMEA** | Propylene glycon methyl ether acetate |
| **PMMA** | Poly(methyl methacrylate) |
| **PPC** | Poly(propylene) carbonate |
| **PPMA** | Poly(n-propyl methscrylate) |
| **PSG** | Phosphosilicate glass |
| **PVA** | Poly(vinyl alcohol) |
| **PZT** | Lead zirconate titanate |
| **SEM** | Scanning electron microscope |
| **SFT** | Smart fabric transducer |
| **SPL** | Sound pressure level |
| **SU8** | Epoxy based photoresist |
| **Textile/Fabric** | Any filament, fiber, or yarn which can be made into fabric. Textile and fabric will be used as same meaning and interchangeable. |
| **TME** | Trimethylolethane |
| **TMP** | Trimethylolpropane |
| **UV** | Ultra violet |

# Nomenclature

| | |
|---|---|
| $\Upsilon_{sl}$ | liquid-solid interface |
| $\Upsilon_{lv}$ | liquid-vapour interface |
| $R_{cla}$ | Roughness of centre line average |
| $L$ | Sampling length |
| $Z$ | Sampling height |
| $n$ | Sampling number |
| $E$ | Young's modulus |
| $\sigma$ | Tensile stress |
| $\varepsilon$ | Extension due to that stress |
| $d_{31}$ | Piezoelectric charge constant at 3-polarisation and 1-stress applied direction |
| $d_{33}$ | Piezoelectric charge constant at 3-polarisation and 3-stress applied direction |
| $L$ | Length of cantilever |
| $W$ | Width of cantilever |
| $f$ | Frequency |
| $V$ | Voltage |
| $V_{rms}$ | Root mean square voltage |
| $\Delta f$ | Bandwidth frequency |
| $f_0$ | Resonant frequency |
| $Q$ | Quality factor |
| $V_{pp}$ | Peak to peak voltage |

# 1. Introduction

## 1.1 Overview of research

Standard electronics technology has advanced in terms of size, power and efficiency leading to smaller, affordable and portable electronic devices such as mobile phone, notebook computers, and tablets. As we move into an increasingly electronic future, the prospect of these devices being flexible and possibly even integrated into textiles is revolutionary. Adding electronic functionality to textiles is an attractive option as textiles have been a fundamental part of our daily lives for many years. Consequently, E-textiles (electronic textile), also known as smart fabrics, is the subject of considerable ongoing research.

E-textiles are textiles that have electronic functionality but retain the physical properties of fabrics. Generally, e-textiles are designed to sense, process and respond to specific external stimuli from the environment. In order to sense or respond to external stimulations, the textiles must incorporate sensors or actuators to produce a smart fabric transducer (SFTs) [1]. In the early development of e-textiles, such devices were unwieldy, not user friendly and unreliable as standard electronics component were attached directly to the textile [2]. However, various smart clothes products were marketed [3] and new applications were explored [4].

A survey conducted on the potential of e-textiles showed that health and safety, communication and entertainment were perceived as major interests for these specialized textile [5]. Example of wearable medical devices are demonstrated by Lifeshirt system which was developed by VivoMetrics, whereby it monitors respiration flow, heart rate, breathing regularity and other vital signals [6]. Applications are not only confined to wearable applications, as demonstrated by *Yongsang et al* and Fibretronic™. *Yongsang et al* have successfully demonstrated passive devices using printing techniques for health monitoring applications [7], while, the Fibretronic™ offers range of switches, sensors and lighting systems for automotive and interior product applications [8]. These demonstrate the wide range of applications where it is possible to be applied e-textiles.

There are 4 main methods used to integrate electronic functionality into an e-textile. These are weaving, knitting, sewing (or embroidery) and printing. Weaving, knitting or sewing involve the addition of electronic functional yarns into the textile during or after its manufacture. Functionality is defined by the type of e-yarn used but in practice this is typically limited to conductive, although there is considerable on going research on other types (e.g. solar, supercapacitor, piezoelectric). Weaving and knitting processes also constrain the location and direction of the e-yarns. In contrast, printing provides a complete freedom for the design layout, since it does not need to follow the fabric structure [9, 10]. The type of ink printed defines functionality and several functions have been demonstrated on textiles such as conductive, piezoresistive, piezoelectric and electroluminescent. Most printed e-textiles are two dimensional (2D) thick-film structures, such as capacitors and resistors [7]. Thus, this thesis is intended to explore the fabrication of small scale (tens of microns to mm) three dimensional (3D) structures using standard printing process and the application of the 3D printing process on three different structures. The evaluation of materials, fabrication processes of the devices on flexible substrate and device performance are presented.

The conventional approach for fabricating small scale 3D structures on a planar substrate is based upon surface micromachining or bulk micromachining used in Micro Electro Mechanical System (MEMS). These fabrication techniques cannot be implemented on textiles due to the requirements of the various processes, which require a smooth flat surface to pattern and which uses corrosive solvents, acids and alkalis which can damage the fabric. However, the concept of surface micromachining, which involves building up structural and sacrificial layers on a silicon wafer substrate and etching the sacrificial layer to produce a free standing structure, can be applied to printed e-textiles [11].

Printing techniques involve the deposition of pastes on to a textile, and is a straightforward deposition process suitable for replicating the surface micromachining processes on fabric. Combining the two concepts of sacrificial layer fabrication and the screen-printing process offers a promising approach for fabricating 3-D structures on fabrics. The printing process also has the advantage of being widely used in the textile industry. However, the requirements for the inks used in e-textiles applications will be very different to the inks used for patterning textiles. Selecting suitable materials and formulating pastes that deliver the required functionality and are compatible with the fabric and processing constraints imposed (e.g. low processing temperatures) is a necessary step towards realising this process.

The realisation of free-standing MEMS on textiles involves several challenges. The challenges can be divided into five main categories which are: substrate or textile sensitivity to temperature and surface roughness of the textile, paste and material compatibilities, and deposition process, sacrificial layer removal and finally device fabrication and evaluation.

- Substrate sensitivity and roughness:
  As the substrate is a fabric, low temperature processing is required at every stage to prevent damage and the surface roughness of the fabric must be addressed. The temperatures used in this process must remain below 200°C and by printing an interface layer, the surface roughness can be improved. These factors will be discussed in Chapter 3.
- Paste and material compatibility:
  The pastes used in this work must be compatible with one another and at the same time must not damage the fabrics. They must exhibit the materials properties required to perform the desired function.
- Deposition process:
  Screen-printing is the only deposition process used in this work. All deposited materials need to be compatible with this process. The deposition of each device is discussed separately in each device chapter.
- Sacrificial layer removal:
  The sacrificial layer should be completely removed while leaving an intact structural layer adhering well to the fabric. The removal mechanism also needs to be compatible with the fabric/textile substrate.
- Device evaluation and fabrication:
  The modelling, fabrication and experimental evaluation of the devices were conducted based on the structure and application of the device. Each of the devices is discussed separately in Chapter 4, Chapter 5 and Chapter 6.

## 1.2 Objective and motivation of the research

The main aim of this research is to fabricate MEMS like structures and devices on flexible substrate such as fabric using fully screen-printing method. To achieve such aim, the following objectives had been investigated:

- Evaluating mechanical properties and process compatibility of potential structural materials (e.g. Minico M 7000 and SU8).
- Investigate removal process and surface wettability of the sacrificial materials: Trimethylolethane (TME) and polyvinyl alcohol (PVA).

- Both structural and sacrificial materials need to be compatible with process and other materials to avoid crosslinking between printed layers. Low temperature curing (<200°C) is essential to avoid damage of the fabric substrate.
- Three structures with different boundary conditions: cantilever, encastre beam and diaphragm structures were selected to demonstrate the feasibility of the process.
- The cantilever structures has to be demonstrated as potential machinery energy harvesting applications. An energy harvester on textile could be used to power an e-textile application and will be discuss more in chapter 4.
- Evaluate and optimise printing parameter for the encastre beam and test as excitation and detection resonator.
- Evaluate diaphragm structure as a buzzer on flexible substrate. The buzzer could be implement as an alarm which can be directly fabricated on fabric.
- Miniaturise the structure to minimise the effect of bending on textile.

## 1.3 Thesis structure

Chapter 2 provides a literature review of the textile and conventional fabrication techniques for electronic garments, as well as sacrificial technology and its applications. This chapter also outlines the details of the screen-printing fabrication process and the equipment used. MEMS devices fabrication are also examined.

Chapter 3 provides details of the materials used in this work in order to fabricate the small scale structures and devices on fabric. This chapter presents the evaluation of suitable sacrificial materials and potential structural material that can be fabricated on textile.

Chapter 4 demonstrates the fabrication, design and testing of screen-printed free-standing piezoelectric cantilever device. Two additional materials, which are silver conductive and a piezoelectric pastes, are introduced. The device was tested as an energy harvesting device with and without a tungsten mass on the tip of the cantilever.

Chapter 5 presents an encastre beam fabricated using the screen-printing process. This is combined with the piezoelectric material to fabricate a resonant sensor with integrated drive and detection mechanisms.

Chapter 6 explores a diaphragm structure that is fixed to the substrate around the edge of the diaphragm, which makes it difficult to remove the sacrificial layer. Outlets through the side wall were introduced in the design and the diaphragm was tested in an anechoic room as a piezoelectric buzzer. The preliminary result of the diaphragm performance is presented.

Chapter 7 presents the general conclusions of the research which includes evaluation of the structural and sacrificial materials, discusses the feasibility of the printing process and the performance of the devices. It also presents some suggestions to improve in this research.

# 2. Literature review: E-textiles and fabrication technology for free-standing devices

## 2.1 Introduction

Research in designing and fabricating free-standing piezoelectric devices on fabric solely using screen-printing involves multidisciplinary approaches. Understanding the concept of a sacrificial layer in the surface micromachining process is one of the requirements although the fabrication technique and materials used are completely different for fabrics. This chapter provides understanding and knowledge as the research foundation and scope.

This chapter is divided into the three main topics of e-textiles, sacrificial and structural technology, and finally examples of free-standing applications using both screen-printing and conventional fabrication. The construction of a textile is also introduced as textile is used as the substrate in this research. The classification and fabrication techniques of e-textiles is first reviewed followed by relevant examples of e-textiles using various fabrication methods to further understand the process.

Sacrificial technology which is mainly used in a surface micromachining process enables a free-standing structure to be formed. It is however, not only confined to surface micromachining but is also used in screen-printing technology. In general, the sacrificial material can be categorised into three main groups which are: silicon MEMS related, water or solvent removal and thermally removed sacrificial materials.

## 2.2 Definition and classification of E-textiles

### 2.2.1 Textile

Textile or fabric has been a fundamental component of our daily lives for many years. Generally, there are three integration levels in order to produce a textile. The first level of integration starts with the smallest unit in textile which are called fibers. Each type of fiber has unique characteristics which determine the properties of the textile. Fibers can also be natural or man-made. These units of fibers are then interlaced to form thread or yarn which is considered as the second level of integration. Some thread or yarn are dyed at this stage to form a colourful thread to be used for embroidery or other sewing process.

The third level of integration involves the yarns to be used in different techniques such as weaving and knitting to form a textile. Generally, woven textiles are composed with two sets of yarns, which are either the same or different, interlaced together at right angles. A higher level, fourth integration involves dyeing process or pattern printing while fifth level concerns finishing processes such as anti-crease treatment to enhance aesthetics and functionality of the textile. Figure 2-1 summaries the level structure from fiber to finishing process.

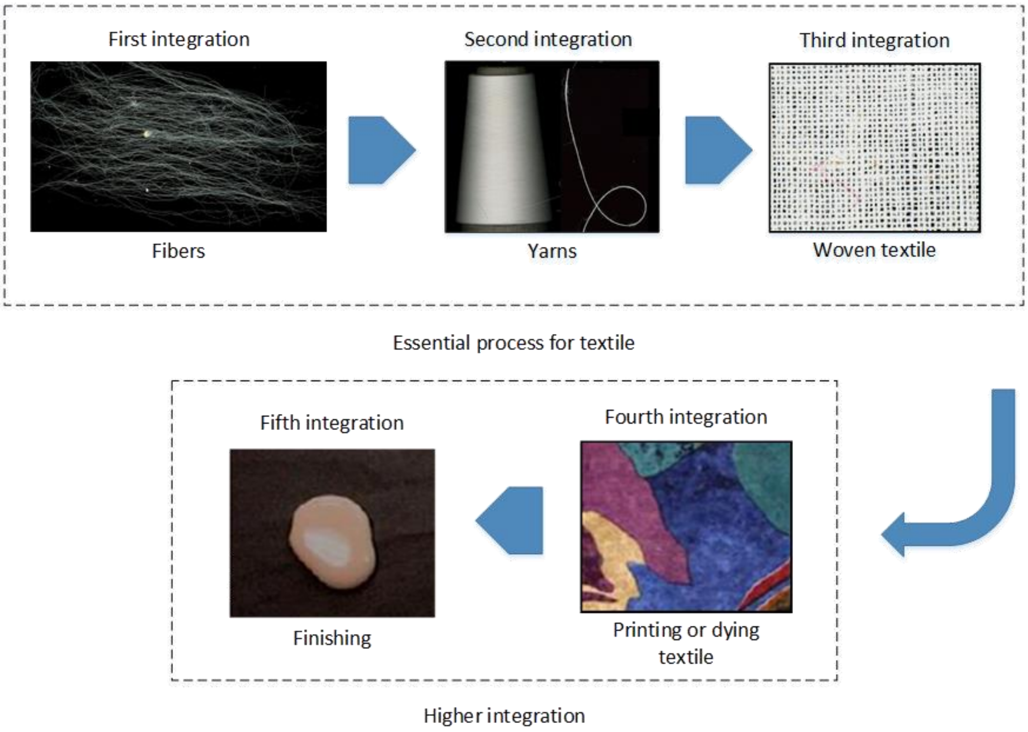

Figure 2-1: Textile integration process to form textile.

In this work, a woven polyester cotton fabric is used as the substrate because this type of textile is commonly used in the textile industry. The working environment of the textile is limited as textile is very sensitive to acidic solvent and high temperature processes (e.g. >200˚C).

### 2.2.2 E-textile

E-textiles are materials or systems that have electronic or electrical functionality but have the physical properties of fabrics. The fabrics are capable of sensing stimuli from the environment, and then react or adapt to the circumstances [12]. The development of E-textiles initially derived from an application where the fabrics only provide a platform. This technology has evolved to incorporate many functions; for example Philip Electronics and Levi Strauss have collaborated in producing the first commercial wearable electronic garment called ICD+ which stands for Industrial Clothing Division Plus [13]. This garment allows the attachment of an MP3 player, a cell phone, a headset and a small remote control. The ICD+ jacket is equipped with a personal area network (PAN). An electronic circuit wired onto the jacket that serves as the backbone for various devices that can be clipped onto it. However, this product proved to be inconvenient as the user needs to detach all the electronic devices before washing.

Electronic textile applications are not just limited to entertainment. *Suh et al* [4] state that the major applications of electronic textile can be categorised into: military, medical devices, communication, entertainment and sport. Electronic textile technology can emerge significantly into the market if the realisation provides flexibility, comfort and convenience to the user.

## 2.3 Fabrication techniques of E-textile

E-textiles are a technology that will have an impact on both the textile and electronics industries. There are standard ways to fabricate electronic textiles that have been reported in the literature. These are weaving, knitting, embroidery and printing.

### 2.3.1 Weaving

Weaving is a technique in which multiple yarns are held in tension perpendicular to each other, known as the weft and warp. The weft yarn forms the width of the fabric while the warp yarn forms the length of the fabric. Most woven fabrics cannot be stretched along the length of the fabric (lengthwise grain) and have minimal elasticity along the width of the fabric (crosswise grain). As a result, the weaving technique provides a very stable and less stretchable fabric structure.

This technique has been demonstrated by *Post et al* [14] from MIT Media Laboratory as shown in Figure 2-2.

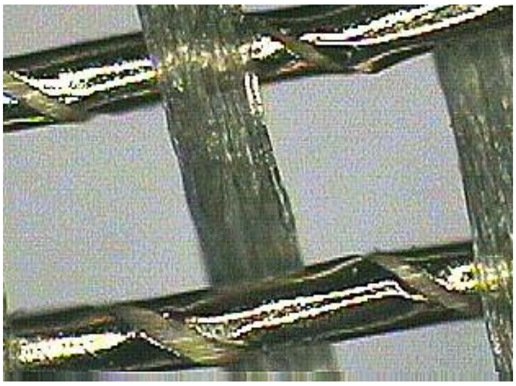

Figure 2-2: Silk thread wrapped with copper foil [14].

Copper foil wrapped around silk threads and ordinary silk threads were used to fabricate conductive fabric tracks. Their work demonstrates E-textiles fabricated in this way in which components such as resistors and capacitors are attached separately using conventional soldering techniques. However, since the weaving only allows an orthogonal wiring construction, it causes restrictions in the design and fabrication of the E-textile.

### 2.3.2 Knitting

Knitting is a technique in which conductive yarns are used to form interconnecting loops. These structures have high stretchability in all directions compared to woven fabrics. This technique, however, requires more flexible yarns in order to form the interconnecting loops.

*Zhang et al* [15] demonstrated a strain gauge fabricated with knitted electronic textiles using two different conductive yarns: stainless steel and carbon fibre. The carbon fibre used was specially treated to allow the formation of a knitted fabric. Their work showed that the carbon fibre is a more appropriate material than stainless steel for knitting due to its smooth surface and ability to return after stretching. Figure 2-3 shows the carbon and stainless steel materials used in knitting.

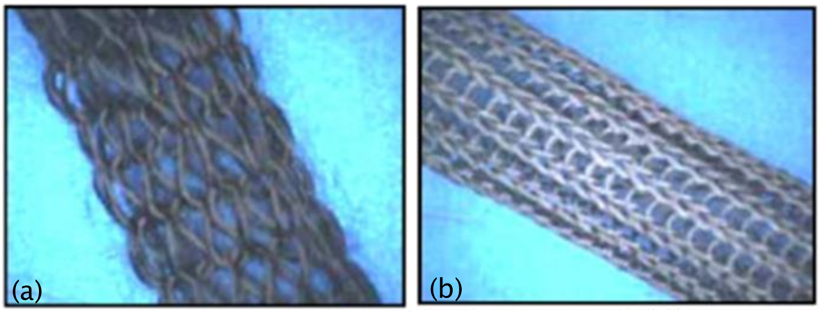

Figure 2-3: (a) Knitted carbon fibre, (b) Knitted stainless steel [15].

### 2.3.3 Embroidery

Embroidery is a combination of stitching or sewing techniques for adding decorations to fabric. The same technique has been adopted to produce conductive patterns using conductive threads. MIT laboratory produced a keypad using this technique. Figure 2-4 shows a keypad that has been embroidered using stainless steel thread and a polyester composite thread. This keypad uses a capacitive sensing technique to sense button presses [16].

Figure 2-4: Embroidered fabric keypad [16].

### 2.3.4 Printing

Screen-printing is a technique that is traditionally used in the textile industry to deposit paste in a desired pattern on fabric for decorative purposes. This technique can also be used to fabricate electronic devices on fabric since it provides less restrictions in terms of the design and fabrication of devices. In 2010, *Yongsang et al* [7] successfully demonstrated screen-printed resistors, inductors and capacitors on fabric by using screen-printing technique. Other components, such as Light emitting diodes (LED) and Integrated circuits (IC), are then bonded directly on to the printed fabric. Figure 2-5 below shows planar structures printed on textile.

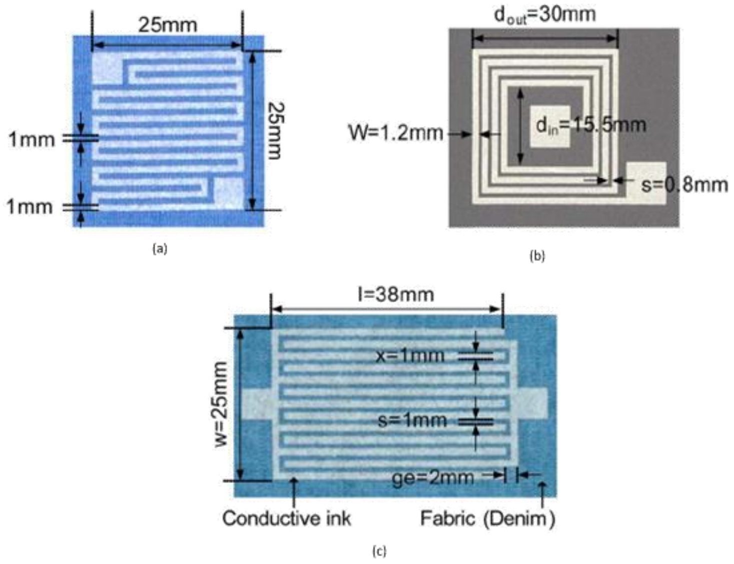

Figure 2-5: Printed (a) resistor, (b) inductor and (c) capacitor [7].

There is a large amount of literature on the various fabrication techniques used to produce electronic textiles. Table 2-1 shows typical devices that use different fabrication techniques to produce electronic textiles.

Table 2-1: Summary of various fabrication techniques for electronic textiles.

| **Device** | **Substrate** | **Fabrication technique** | **Performance** | **Application** | **Reference** |
|---|---|---|---|---|---|
| Antenna | Woven fabric | Plated nickel | Permitivity $\varepsilon_r$ 1.15+/-0.02 at frequency of 2.4GHz. | Monitoring patients | [17] |
| Patch antenna | Fabric | Screen-printing | Worked at desired frequency (2.4-2.45 GHz) with low return loss. | Wireless gas sensor | [18] |
| Battery | Coated fiber | Woven | Not reported. | Electrical energy generation or storage | [19] |
| Transistor | Coated fiber | Woven | Clear field effect current is very low. | Electric circuits | [20] |
| Inductive fiber meshed transducer | Coated fiber | Knitting | Normalized induced voltage at 60 degree arm bending was 0.25 W. | Rehabilitation | [21] |
| Fabric switches | Conductive polymer yarns | Knitting | Closed circuit when electrode were touched. | Alarm switches or keypad | [21] |
| Capacitor | Interface fabric | Screen-printing | 3.94 pF to 7.59 pF for different size of electrodes. | Motion detector | [22] |
| Capacitor | Fabric | Inkjet printing | Values varies at different frequency 163 pF at 100 Hz and 113 pF at 9 GHz. | Proximity or touch sensor | [23] |

| | | | | | |
|---|---|---|---|---|---|
| Micropump | Kapton | Screen-printing | Maximum flow rate of 67 μL/min at frequency of 600kHz. | Drug delivery | [24] |
| Electroluminescent Lamps | Fabric | Dispenser printing | Illuminated at 400 Hz at driven voltage of 180Vac. | Safety workwear | [25] |
| Electrical connections | Fabric | Screen-printing | The optimum thickness for strain gauge are 400 μm and 700 μm for different types of fabric. | Strain gauge | [26] |
| Strain sensor | Elastic fabric | Coating | Real-time monitoring of human motions, such as bending of finger and rotation of wrist, was achieved. | Monitoring patients | [27] |
| Biofuel cell | Elastic fabric | Screen-printing | Generated the maximum power densities of 160 and 250 mW cm$^{-2}$. | Self-powered sensor | [28] |
| Shoe-insole energy harvesting | Fabric | Screen-printing | Experimental results show that one element produced 2V. | Wearable energy harvesting | [29] |
| Thermoelectric generator | Glass textile | Screen-printing | Seebeck coefficient ranges from 163.1 to 229.3 μV/K. | Body temperature energy harvesting | [30] |

Although the approaches described above can be used to fabricate components for electronic textiles, there remain a number of challenges in this area such as achieving reliable and robust interconnections to the device and maintaining the textile's inherent characteristics such as flexibility, washability [31] and durability [10]. Furthermore, most of devices previously fabricated on textiles are 2D or planar devices. There is a research gap in terms of the development of 3D or free-standing structures. The only literature found that describes such a process is work by *Wei et al* [32] who fabricated a cantilever structure for use as a motion detector on fabric. This work will be discussed in section 2.4.4.

Weaving techniques are not appropriate for this application as this process needs to incorporate active materials (e.g. conductive yarn) in the fabrication technique and they are not capable of forming a 3D structure [33]. There is a disadvantage using weaving technique as reported by *Post et al* [34], that is, the steel or steel composite threads tend to bunch up as they are fed through a sewing machine.

In the research described in this thesis, screen-printing is considered the most suitable fabrication technique to produce free-standing structures on fabric. Screen-printing is a cost effective and fast process. In addition, this process allows more design freedom and provides the ability to produce arrays of printed devices on the same substrate [22], which is more appropriate than the other described techniques for mass production.

## 2.4 Sacrificial and structural technology achieved by screen-printing

Screen-printing techniques have traditionally been used in the textile industry to create decorative patterns on fabric before it was adopted in thick-film technology [35]. Screen-printing is considered to be more versatile, simple, fast and cost effective compared to other processes such as lithography and low pressure chemical vapour deposition (LPCVD). This process does not require expensive equipment, yet a variety of sizes, shapes and materials can be deposited [33, 36].

### 2.4.1 Overview of screen-printing

The first stage in a screen-printing process is the deposition of ink onto a substrate through an open mesh. A paste is placed on the top of the screen and spread across the screen in a process known as 'flooding'. A squeegee is then passed transversely across the screen with a controlled pressure exerted downwards on the squeegee. The screen is, in this way, pressed into contact with the substrate, forcing the paste through the gaps in the screen and depositing paste in a pattern onto the substrate. This process is illustrated in Figure 2-6.

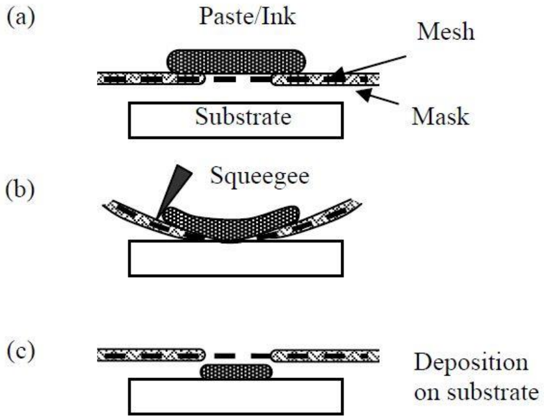

Figure 2-6: Screen-printing process [37].

The second stage of the screen-printing process is evaporating the organic solvent in the printed paste. This is usually performed either by thermal or UV curing, depending on the paste properties. The dried layer is then relatively resistant to smudging and the substrate can be handled or manipulated easily. Another layer can then be printed directly on the dried layer in order to build up the required thickness.

### 2.4.2 Definition sacrificial and structural technology

Sacrificial and structural technologies are based on surface micromachining process which involves etching and deposition of different functional layers extended above the surface of the substrate. In order to fabricate a free-standing structure, sacrificial technology is essential. This technology enables not only free-standing structures but also more complex structures as proven by Sandia National Laboratories [38]. They had fabricated a complex 5 layer polycrystalline silicon device with layers of thickness 1-2 µm, using silicon dioxide and polycrystalline silicon as the sacrificial layers and structural layers respectively. This technology is not only implemented in a conventional process (surface micromachining) but also in screen-printing.

Sacrificial technology is a method whereby an underlying layer called ‘sacrificial layer’ is deposited to serve as a temporary support platform or “placeholder” for a subsequent layer. This layer is then ‘sacrificed’ or dissolved in order to form a free-standing structure [11].

The free-standing structure is the main and important mechanical structure that is used solely for mechanical purposes. It is also defined as any material of which the primary function is to be loaded or stress bearing [39]. Silicon is the main mechanical material used in the conventional process while ceramic or polymer are used in screen-printing process. Each type of structural material selected is specific to, and suitable for, the application or process. There are no generic structural materials suitable for all applications or processes. However, there are certain criteria and properties for sacrificial and structural materials. Table 2-2 shows the properties and criteria of both of these material types.

Table 2-2: Similarities and differences of both sacrificial and structural material for screen-printing process.

| **Similarities** | |
|---|---|
| • Ease of deposition and patterning<br>• Compatible with substrate and subsequent layer | |
| **Differences** | |
| **Sacrificial** | **Structural** |
| • Total removal to prevent stiction | • Provide a solid foundation of the structure<br>• Strong adhesion to the substrate and subsequent layer |

The priority for both materials are ease of deposition and patterning. The printed layers should also be compatible with the substrate, process and subsequent layers. Another important criteria is the processing temperature so that the substrate, structural, sacrificial and functional layers withstand one other processes without any reaction. There are two types of process which are high temperature (e.g. >850˚C) and low temperature (e.g. < 200˚C) process to achieve sacrificial and structural technology by screen-printing. These processes are reviewed in the next section.

### 2.4.3 High temperature process

Screen-printing process as explained in section 2.4.1, involves printing and curing processes which are repeated until the desired thickness is achieved. Each printed layer is cured to solidify the printed paste and also provide a foundation for subsequent layer(s). The printed layers are cured based on the recommended process temperature and usually material which contains either a glass binder or ceramic require higher curing temperature process. Table 2-3 summaries the high curing temperature process for a screen-printed free-standing structure.

Table 2-3: Screen-printed free-standing structure achieved by high temperature curing process.

| **Structural material** | **Sacrificial material** | **Structure** | **Removal process** | **Curing conditions** | **Ref** |
|---|---|---|---|---|---|
| Au/PZT/Au<br>(Au from ESL8836) | Strontium carbonate (SrCO3) | Cantilever<br>Bridge | Submerge in phosphoric acid ($H_3PO_4$) solution | 920ºC, 15 min | [40] |
| Electrode/PZT ceramic/Electrode | Graphite paste<br>(Sigma-Aldrich 28,286-3) | Cantilever | Removed during curing process | 850ºC, 15 min | [41, 42] |
| ESL Dielectric/Au/ ESL Piezoresistive | EPOXY with Strontium carbonate (SrCO3) | Cantilever | Submerge in phosphoric acid ($H_3PO_4$) solution | 850ºC | [43] |
| Dielectric material | Undefined sacrificial material | Cantilever | Chemically removed with potassium iodide | 850ºC, 15 min | [44] |

Ceramic materials such as alumina ($Al_2O_3$), beryllia (BeO) and aluminium nitride (AlN) are examples of ceramic materials which are commonly used in screen-printing technology. Alumina is used in hybrid microelectronic devices due to its excellent properties such as chemically resistance, robust and ability to withstand a high temperature process greater than 800ºC. A glass binder are usually used to increase density and to form a homogeneous solid layer. A glass binder had been used and demonstrated by *Debeda et.al.* [40] to fabricate bridge and cantilever structures. The main structural material consisted of PZT powder which was combined with 5% wt of borosilicate glass-frit and sandwiched with gold electrodes. Both free-standing structures were achieved by printing a strontium carbonate sacrificial layer which remained after a 15 minute 920ºC firing process. The samples were then isostatically pressed and the sacrificial layer was removed in a weak acidic solution. The devices fabricated are shown in Figure 2-7.

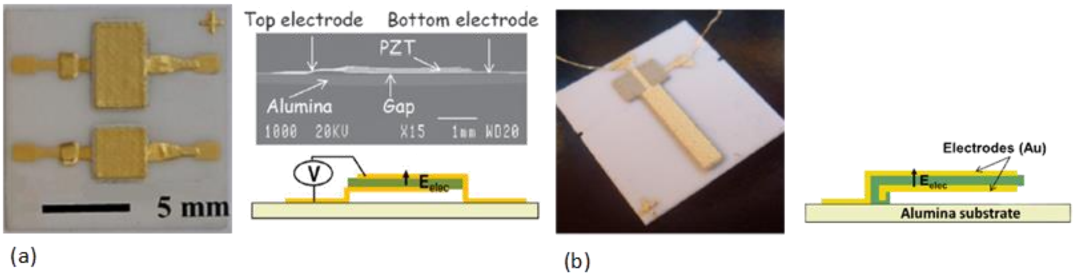

Figure 2-7: Screen-printed free-standing (a) bridge and (b) cantilever structure fabricated at high temperature [40].

A similar method had been adapted by *Kok et.al.* [41] to fabricate a free-standing cantilever for energy harvesting. A graphite powder was used as the sacrificial material and for the structural material PZT with a glass binder was used. The structure suffered delamination and shrinkage due to different thermal expansion coefficient between the materials after the removal process. However, these issues were solved by screen-printing and firing a multilayer arrangement of PZT and electrode layers at 850ºC for 10 minutes. Figure 2-8 (a) and Figure 2-8(b) shows the delaminated and multilayer cantilever structure respectively.

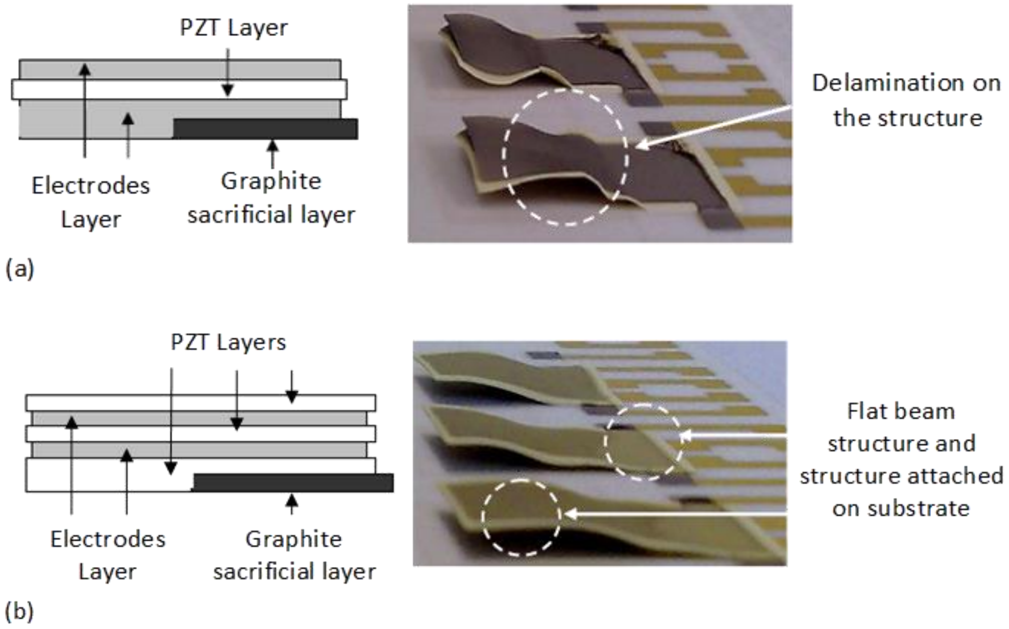

Figure 2-8: Cantilever device fabricated (a) with delamination on structure and (b) with multilayer electrodes and PZT layers [41].

A unique approach to fabricate a free-standing diaphragm structure for high temperature applications was demonstrated by *Sippola et al.* [44] The fabrication process of a diaphragm starts with laser drilling an alumina substrate to create an outlet for the sacrificial layer. A bottom electrode followed by a dielectric layer was then printed on top of the alumina substrate. Next, a sacrificial layer was printed and dried. Then, the same dielectric was printed covering the sacrificial layer, followed by top electrode. Once all the layers were cured, the sacrificial layer was chemically removed by using potassium iodide solution and the outlet was sealed using a dielectric material. Figure 2-9(a) shows pre and post sacrificial layer removal and Figure 2-9(b) is the cross section of the printed device.

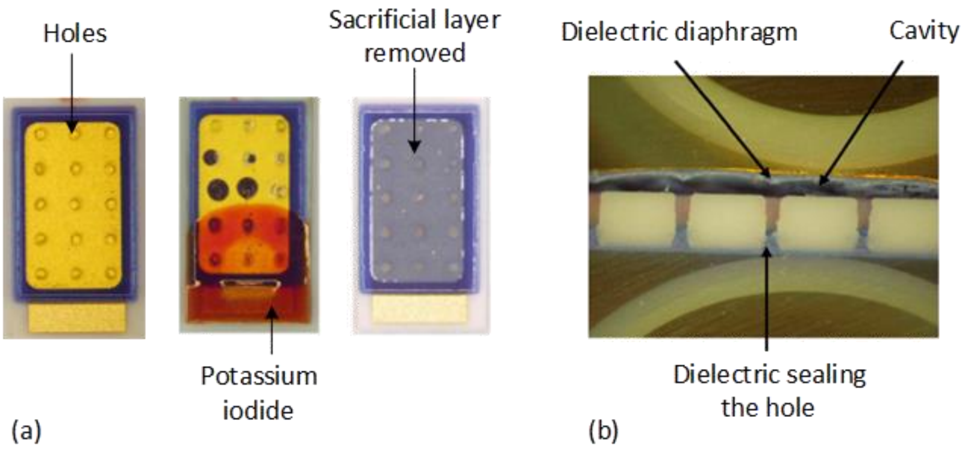

Figure 2-9: (a) Diaphragm structure before and after sacrificial removal and (b) cross section of diaphragm structure [44].

The high curing temperature and required removal solutions means that ceramic paste and glass binders are not suitable to be used in this research. This is due to the textile properties being degraded at high temperature and decomposed in acidic solution. A low temperature process is important to enable the fabrication process to be conducted on textile.

### 2.4.4 Low temperature process

The substrate targeted in this research is polyester cotton textile. This textile is sensitive to chemical solvent and high temperature. As described in Chapter 3 section 3.2.3, polyester cotton is able to withstand temperature up to 200°C for short curing period (less than 3 minutes) while, strong chemical solvents such as hydrochloric-acid (HCl) are corrosive and able to decay the properties of the fabric. However, some removal processes and the temperatures required are suitable for textiles. These are reviewed and concluded in Table 2-4.

Table 2-4: Free-standing structure fabricated using screen-printing method.

| **Structural material** | **Sacrificial material** | **Structure** | **Removal process** | **Curing conditions** | **Ref** |
|---|---|---|---|---|---|
| Silver epoxy | Polyvinyl alcohol (PVA) | Cantilever | Submerge in Water | 160 ºC, 60 minutes | [45] |
| Electra EFV4/4965 | Polyvinyl alcohol (PVA) | Cantilever | Submerge in water | UV cured, 60 seconds | [46] |
| Electra Polymers EFV4 | Trimethylolethane (TME) | Diaphragm cantilever | Sublime at 160 ºC for 30 minutes | UV cured | [22, 24] |

Water soluble materials or solvents are commonly used in everyday usage especially for fabrics. Polyvinyl alcohol (PVA) is used as sacrificial material since it is easily dissolved in warm water. *Rivadeneyra et al* [45] demonstrated a free-standing structure with this sacrificial layer using screen-printing and bonding techniques as shown in Figure 2-10.

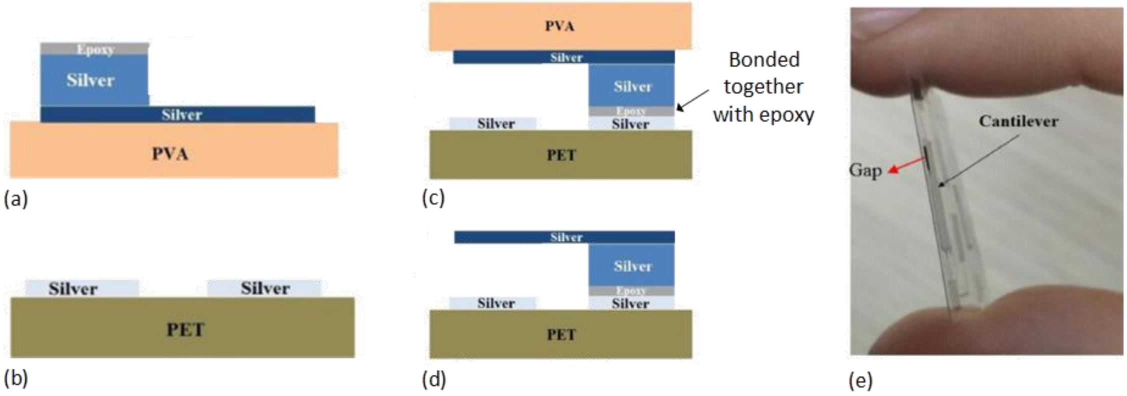

Figure 2-10: Two parts were printed separately (a) on PVA and (b) on PET and (c) both structures were bonded with epoxy. Finally (d) sacrificial was removed and (e) the actual device [45].

The sacrificial layer implemented was applied on the beam of the structure rather than between the structures. Two separate parts were printed on a PET flexible substrate and PVA. Then, these parts are aligned and bonded together using an epoxy (EPO-TEK H20E) at 80ºC for 30 minutes. The device was then submerged in water to remove the sacrificial layer.

The same sacrificial material was demonstrated by *Yang et al.* [46] using only screen-printing. A capacitive cantilever device was directly printed and cured on fabric without damaging the properties of the substrate as shown in Figure 2-11.

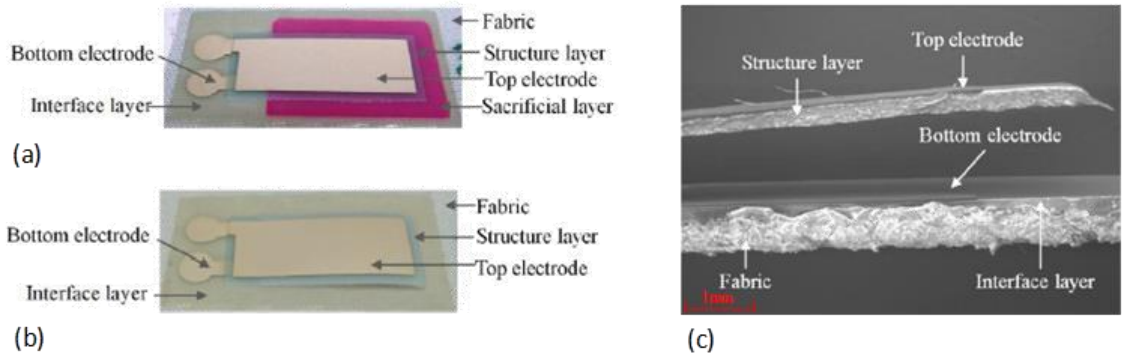

Figure 2-11: Cantilever structure (a) before removal, (b) after removal and (c) SEM image [46].

An interface layer (Fabink-UV-IF1004) was used to reduce the surface roughness of the fabric followed by a bottom silver electrode. Then, the PVA sacrificial layer was printed and cured at 100ºC for 3 minutes. The structural layer and top electrode were the final layers printed before the sacrificial was removed in water. The process conducted by *Yang et al* are compatible with fabric as the highest temperature used was 120˚C. The removal process did not use strong acidic solvent but was removed by hot water ranging between 80˚C to 100˚C. Further evaluation on the sacrificial is of interest as the process and materials are compatible with fabric.

The research conducted by *Wei et al.* [24] is also on fabric. However, a different sacrificial layer which used a thermal removal process was implemented. The main material used was Trimethylolethane (TME), which is a plastic crystalline material which begins to sublimate at a relatively low temperature (87˚C). This material was previously reported by *Serra et al* [47] which fabricated microchannel, cantilever and bridge structures to demonstrate the feasibility of the process on alumina.

In comparison to *Serra et al* , who applied a TME sacrificial layer on an alumina substrate, *Wei et al* [22] implemented the sacrificial layer by screen-printing it on a fabric substrate. To demonstrate the feasibility of the TME sacrificial material, *Wei et al* fabricated a pump structure on Kapton [24] and a cantilever structure on fabric [22]. Figure 2-12(a) and Figure 2-12(b) show the pump structure and the cross section of the pump after the removal process respectively.

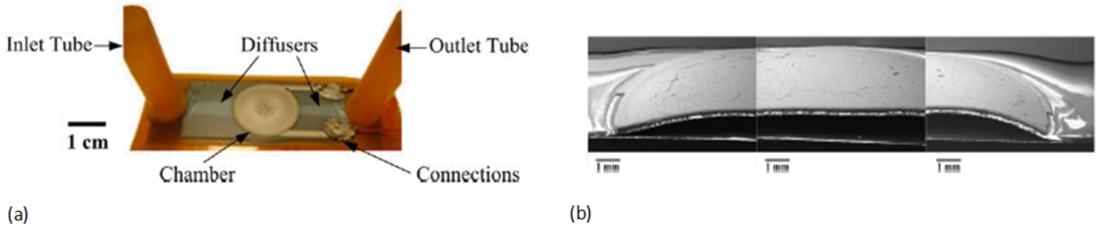

Figure 2-12: (a) Micropump structure fabricated using the TME sacrificial material and (b) cross-section of micropump after removal [24].

The free-standing cantilever structure demonstrated by *Wei et al* [48] shows wavy edges and poor resolution as illustrated in Figure 2-13. It is important to have structural materials that have good mechanical properties to prevent deformation after removal. Further examination and selection of structural materials will be discussed in Chapter 3 section 3.4.

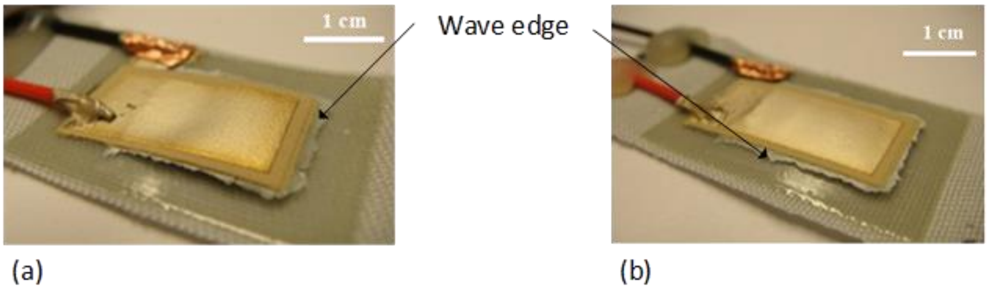

Figure 2-13: Wave edge reported by *Wei et al* from two different length of cantilever (a) 12mm and (b) 15mm [48].

In comparison with a high temperature process, low temperature processes are more suitable and compatible with sensitive substrate such as textile. Both water removal (PVA) and thermal removal (TME) sacrificial material are of interest due to the low temperature process and water based removal which retain the properties of the substrate. Although, both of the sacrificial materials were previously successfully fabricated on fabric, a further comparison between both sacrificial materials was not presented. A commercially available structural material is of interest to extend the applicability of the process.

## 2.5 Free-standing devices based on sacrificial technology

### 2.5.1 Introduction

A free-standing structure is defined as one that stands alone, or on its own foundation. The structure is free from external support or attachment to a non-electrically-active platform. This structure can have a variety of forms based on its boundary conditions ranging from a simple cantilever to complex structures like honeycombs.

The mechanical structure or boundary conditions of the structure determine the type of the structure. For example, a cantilever structure is confined with one end of the structure fixed while the other end is free to move. A bridge structure, also known as encastre beam, is a structure in which both ends are fixed while the centre part of the structure is free to vibrate. More complicated structures such as a diaphragm have all edges of the structure fixed, leaving a cavity beneath the structure free.

The wide applications and integration of microelectronics and micromechanical systems (MEMS) have led to the development of free-standing micromechanical devices. Generally, these free-standing MEMS devices had been fabricated with two main methods which are bulk and surface micromachining process. Further details and examples are discussed in section 2.5.3. Screen-printing technology had been used for many years to print patterns on fabric, but very limited MEMS structure fabricated using this method. This opens research possibilities and development process especially for a low temperature process for application on textile. Section 2.5.2 presents screen-printed devices both on rigid and flexible substrates.

### 2.5.2 Screen-printing fabrication techniques

Screen-printing technique has been introduced in section 2.4.1, consisting of a repetitive process of printing and drying or curing to solidify the printed paste to achieve the desired thicknesses. Most of the screen-printing process is conducted either directly on an alumina substrate or a flexible substrate supported by an alumina tile. This is because an alumina tile is able to withstand high temperature process and able to resist harsh chemicals. The rigid, sturdy and flat surface of alumina tile is suitable for supporting flexible substrates such as Kapton and fabric.

A free-standing structure is possible to achieve by using a sacrificial layer as used in conventional MEMS processing technologies as described in section 2.5.3. A simple cantilever or a complicated diaphragm structure is possible to fabricate by implementing this technique in a screen-printing process.

#### 2.5.2.1 Cantilever structure for screen-printing

One of the most commonly fabricated structures is a cantilever. This is due to its simple geometry and vast applications. One of the examples of screen-printing fabrication using this structure has been demonstrated using strontium carbonate epoxy as sacrificial material. Three different applications shown in Figure 2-14 have been demonstrated using (a) copper, (b) gold and (c) silver-palladium (AgPd) as the structural material. A sacrificial layer pad was first printed and cured for 25 minutes at 125ºC prior to the screen-printing of each respective structural layer. The sample was then cured for 15 minutes at a temperature of 850ºC under ambient air and finally immersed for 5 min in a phosphoric aqueous solution to remove the sacrificial layer. Figure 2-14 also shows the cross section of the devices from SEM images [49].

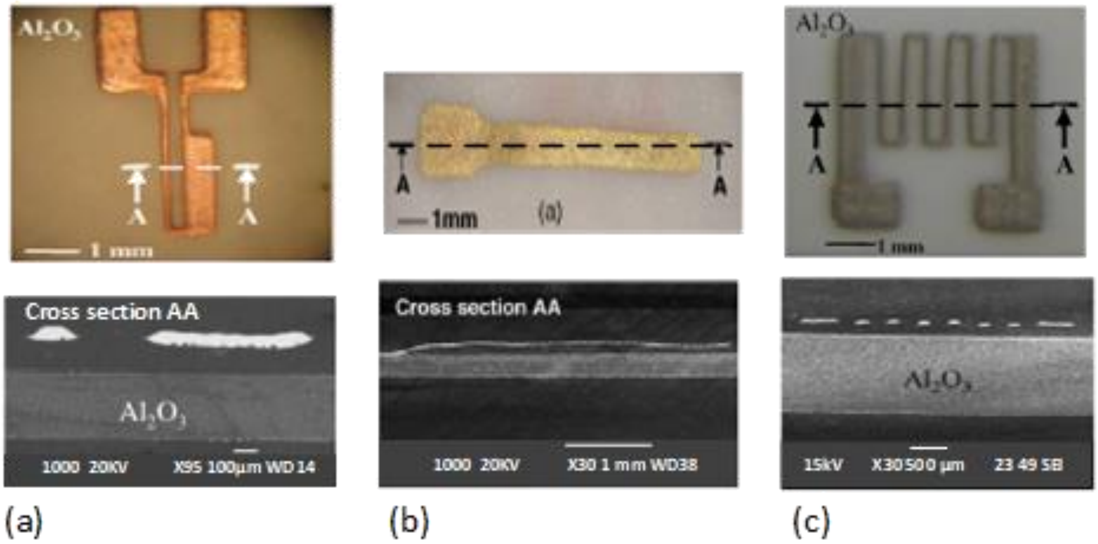

Figure 2-14: Free-standing structure with (a) copper, (b) with gold and (c) with silver palladium[49].

As presented prevously in section 2.4.4, *Yang et al* [46] and *Wei et al* [50] had also used the cantilever structure to fabricate a free-standing capacitive device. Both cantilever structures were 15 mm x 10 mm and used the same structural material but different sacrificial removal method. There were 135 Hz differences of frequency reported by *Yang et al* and *Wei et al*. This might be due to variation of thickness of printed layers. Figure 2-15 shows fabricated cantilever device on fabric.

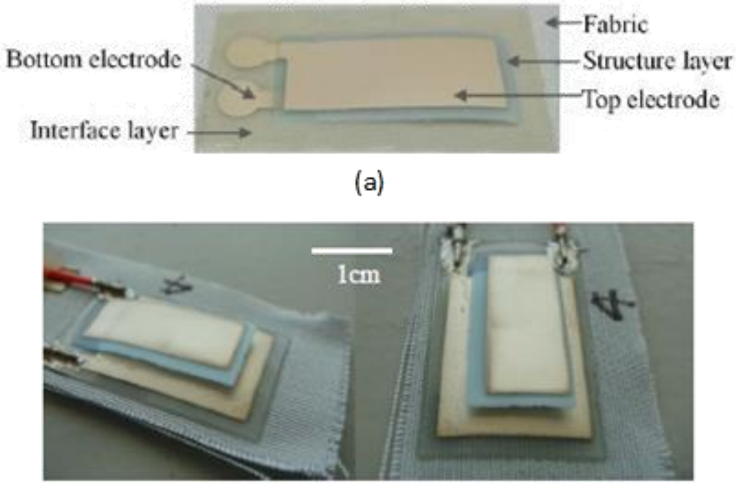

(a)

(b)

Figure 2-15: Cantilever device fabricated by (a) *Yang et al* [46] and (b) *Wei et al [50]* on fabric.

A gas sensor had been fabricated by *Debéda et al* [51] by screen-printing technique. The same strontium carbonate epoxy was used for sacrificial layer and the highest temperature was used to cure the sample was 900°C for 2 hours. Incorporating a sacrificial layer in the process allows a free-standing piezoelectric cantilever to be achieved. A sensitive layer was drop coated on the cantilever structure to detect toluene gas in room temperature. Figure 2-16 shows the fabricated piezoelectric cantilever device as toluene gas sensor.

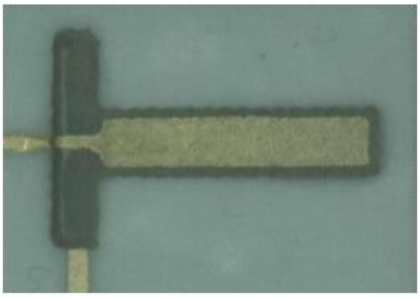

Figure 2-16: Piezoelectric cantilever device with 8 mm length 2 mm wide fabricate using screen-printing method as toluene gas sensor [51].

A free-standing energy harvesting cantilever structure had been demonstrated together with carbon based sacrificial material. A PZT ceramic and silver/palladium (Ag/Pd) was used as piezoelectric layer and electrodes respectively. The sample was cured at 850°C for 10 minutes while the sacrificial layers were burnt out through the curing process.

Figure 2-17 shows the free-standing structure dimensions of 18 mm long by 9 mm wide and thickness of 50 µm fabricated solely using screen-printing technique.

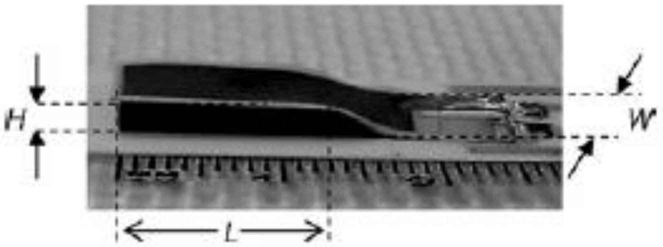

Figure 2-17: Piezoelectric cantilever for energy harvesting application [42].

#### 2.5.2.2 Encastre beam structure for screen-printing

There are very few screen-printed encastre beam reported compared to cantilevers. One of the bridge structure fabricated using screen-printing method was reported by *Serra et al [47]*.

The bridge structure was fabricated to evaluate the compatibility between the structural and the sacrificial material used. Ethylcellulose was chosen as the structural layer and a mixture of TME and TMP as the sacrificial material. Both sacrificial and structural material work very well together, a complete removal of the sacrificial layer can be observed leaving a clean and relatively well preserved structure. Figure 2-18 shows the bridge structure fabricated on an alumina substrate.

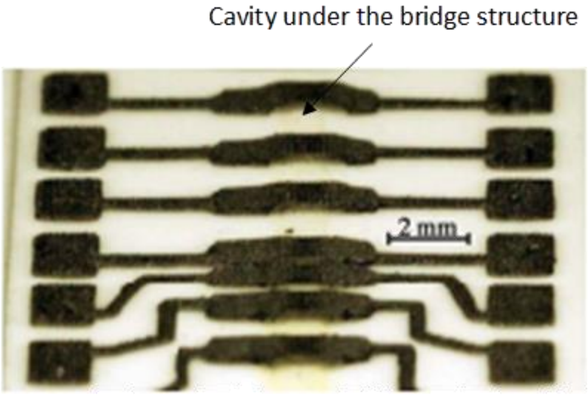

Figure 2-18: Bridge structure fabricated using ethylcellulose as structural material on alumina substrate [47].

#### 2.5.2.3 Diaphragm structure

A diaphragm structure is more complicated structure compared to the cantilever and encastre beam. This is due to all edges of the diaphragm being clamped, leaving the middle of diaphragm to be free-standing. It is difficult to fabricate a diaphragm structure using screen-printing method. However, it is possible by implementing an outlet or channel through which the sacrificial is removed. There are very few reported diaphragm structures fabricated using screen-printing.

The diaphragm structures fabricated by *Sippola et al* [52] was reported previously in section 2.4.3. The capacitive diaphragm was fabricated using screen-printing method instead of low temperature co-fired ceramic (LTCC) technique on an alumina substrate. The implementation of sacrificial layer in screen-printing technique gives the flexibility to control the thickness of the cavity compared to LTCC technique which uses commercially available green tapes that come in standard thicknesses of 114, 165 and 254 µm. The initial thickness of the diaphragm was 32µm and was fabricated with two different sacrificial thicknesses which were 12 and 22µm. Figure 2-19(a) and Figure 2-19(b) show the top view and cross-section of the diaphragm structure respectively.

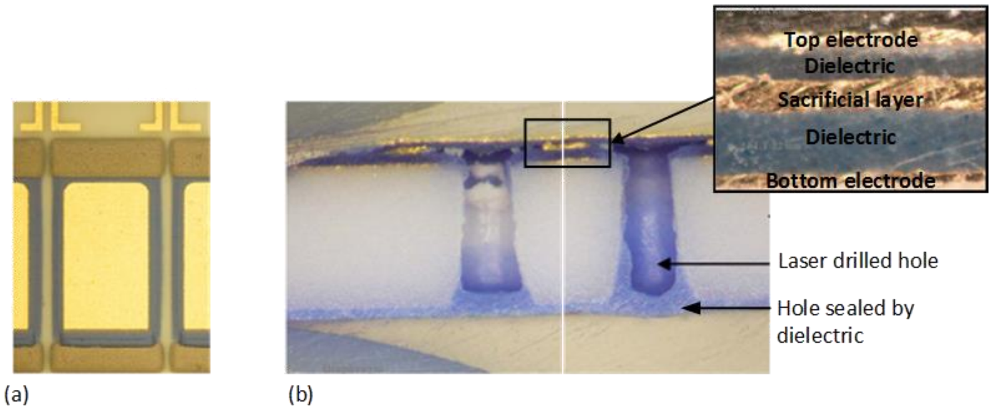

Figure 2-19: (a) Top view of diaphragm structure and (b) cross-section image of the structure [53].

*Wei et al* [24] on the other hand, used screen-printing method to fabricated diaphragm structure at low temperature process. The piezoelectric diaphragm was fabricated on Kapton with the outlet channel located at each end of the structure to remove the sacrificial layer. The piezoelectric diaphragm was successfully tested to transport water from one side of the diaphragm to the other. Figure 2-20 shows the micropump fabricated on Kapton using a low temperature process.

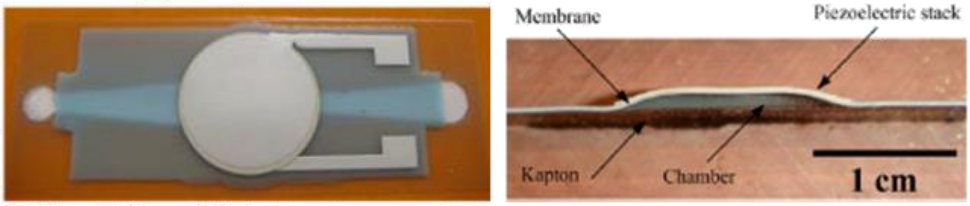

Figure 2-20: Diaphragm structure fabricated on Kapton [24].

The devices in this section are solely fabricated using screen-printing technique. Most of the fabricated structures are not compatible with fabric application as the curing temperature, in excess of 800˚C which will destroy the fabric properties. However, the process demonstrated by *Yang et al* and *Wei et al.* is of interest as the temperature and material used in the process are compatible fabric. There are very limited applications using low temperature process (<200˚C) being reported either on fabric or Kapton.

### 2.5.3 Conventional fabrication techniques

Conventional micromachining techniques involve the process of transferring a pattern from a master mask to another surface on the substrate which is usually silicon. The pattern protects the selected areas of the substrate during the etching process and further areas are selectively removed later based on the structure desired. There are two major classifications of micromachining techniques which are bulk micromachining and surface micromachining.

Bulk micromachining techniques primarily use accurate and precise machining of a thick substrate. This process selectively removes significant amount of silicon from a substrate to form a structure which requires a physical movement such as cantilevers or membranes. This technique involves either etching silicon in all directions at the same rate known as isotropic wet etching or removing silicon at the rate that depends on the orientation of the crystal lattice structure known as anisotropic wet etching.

A piezoelectric generator based on cantilever structure had been presented by *Fang et al* [54] using bulk micromachining techniques. The fabrication process is as shown in Figure 2-21.

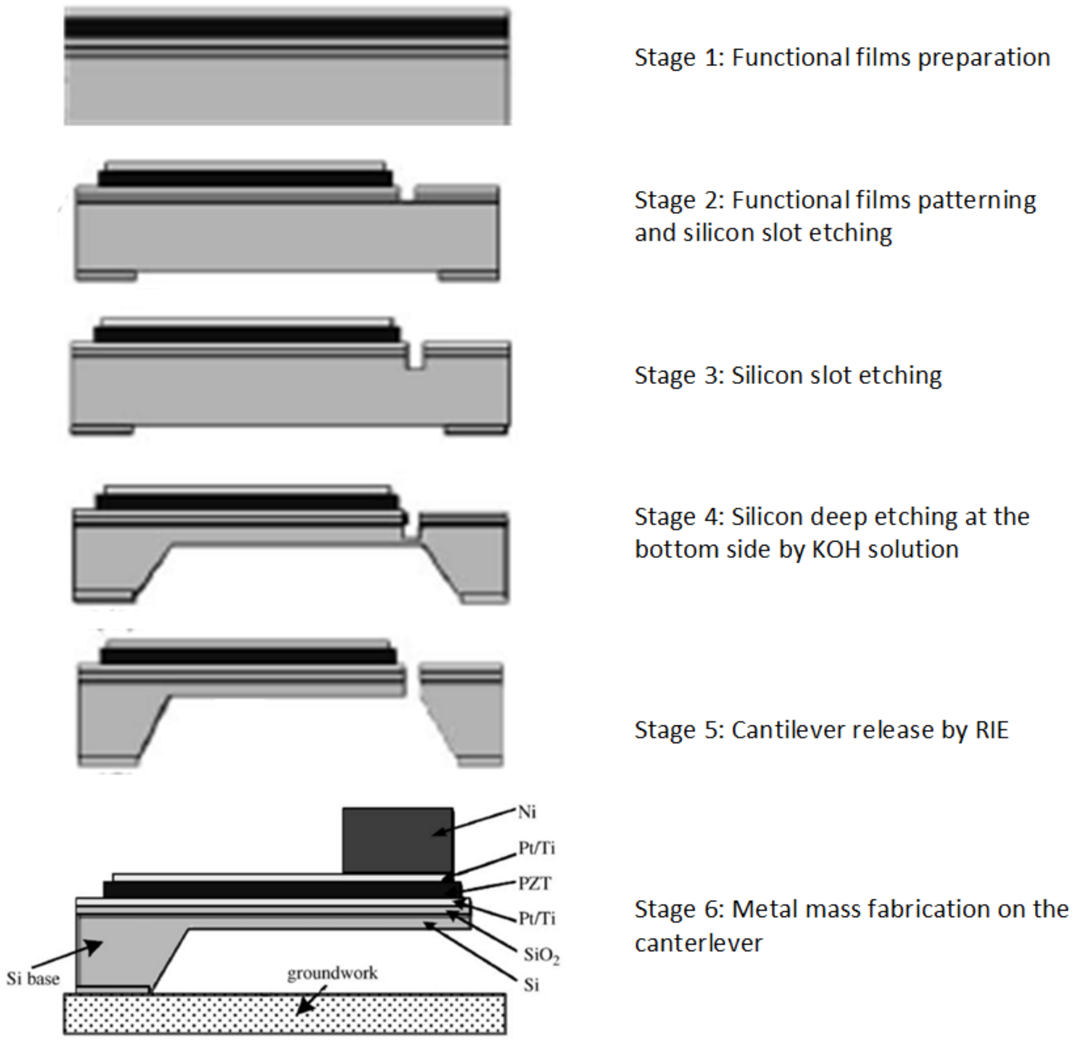

Figure 2-21: Bulk micromachining process for piezoelectric cantilever structure [54].

In contrast to bulk micromachining process, surface micromachining builds up layer by layer on top of the substrate surface [11]. A sacrificial layer technique is usually used whereby the mechanical structure which forms the moving structures is deposited on a temporary support platform. The support platform is then removed by chemically etching away this material. This platform is known as a sacrificial layer. Unlike bulk micromachining, where a silicon substrate is selectively etched to produce a free-standing structure, surface micromachining is based on the deposition of different materials on top of the substrate. Therefore, a variety of substrates such as glass can also be used as substrate compared to those used in bulk micromachining. Figure 2-22 shows the fabrication steps for surface micromachining.

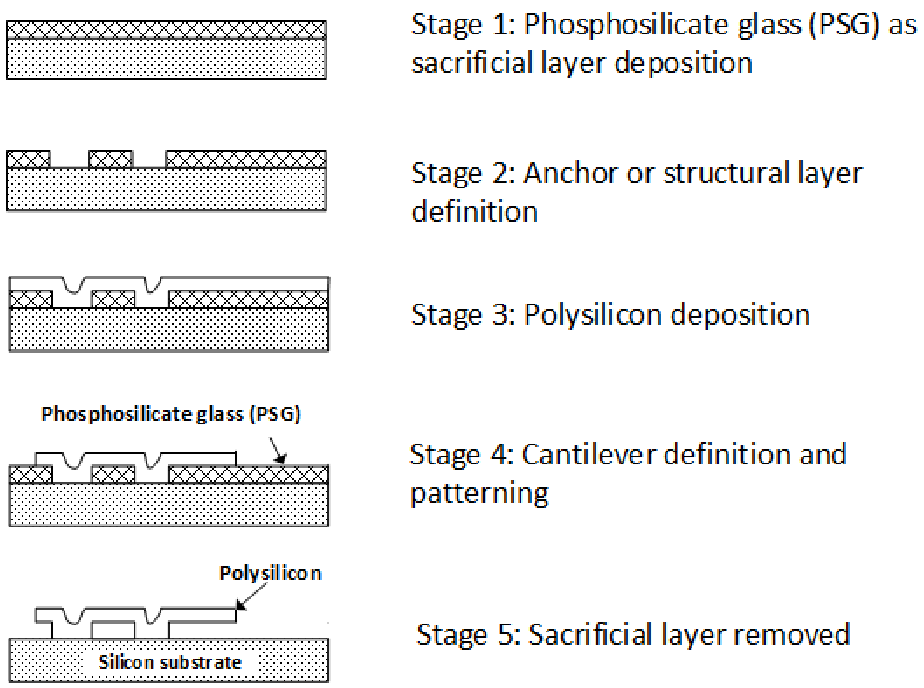

Figure 2-22: Simplified surface micromachining process [11].

Additionally, this concept is suitable to be implemented with screen-printing allowing a free-standing structure to be produced at minimal cost. This is because screen-printing can be conducted without a clean room and requires simple machinery compared to both types of micromachining process.

However, it is essential to know that similar structures can be fabricated using surface micromachining process as this concept can be applied to screen-printing. In this section, cantilever structure for energy harvesting, encastre beam used in resonator and diaphragm structure fabricated using this process are presented and reviewed.

#### 2.5.3.1 Cantilever structure

Various research groups have investigated the cantilever structure for various applications including energy harvesting. Energy harvesting or energy scavenging has become a growing interest of researchers to replace energy supply from electrochemical batteries. The limitation of energy capacity and periodically battery replacement are some of the reasons for scavenging energy from external source. The ambient energy sources such as solar, thermal, mechanical vibration and human movement are some of the energy sources available. In this section, piezoelectric cantilever device fabricated especially for energy harvesting application is reviewed. Table 2-5 shows some of the cantilever structure fabricated using conventional fabrication process for energy harvesting application.

Table 2-5: Sumarry of piezoelectric cantilever fabricated for energy harvesting application.

| **Cantilever type** | **Fabrication** | **Power output** | **Frequency** | **Ref** |
|---|---|---|---|---|
| Bimorph cantilever | Surface and bulk micromachining<br>Screen-printing | 7.35μW and 33.2μW | 344 Hz | [55] |
| Unimorph cantilever | Surface micromachining<br>Screen-printing | 7.56μWs$^4$/m$^2$ | 515 Hz | [56] |
| ZnO Unimorph cantilever | Surface and bulk micromachining | 0.98μW | 1300 Hz | [57] |

A typical piezoelectric energy harvester consists an active piezoelectric elements with metal electrodes on top or both sides depending on either unimorph or bimorph cantilever beam configuration on a passive mechanical support structure. The structure is anchored at one end and attached to a proof mass at the other as illustrated in Figure 2-23.

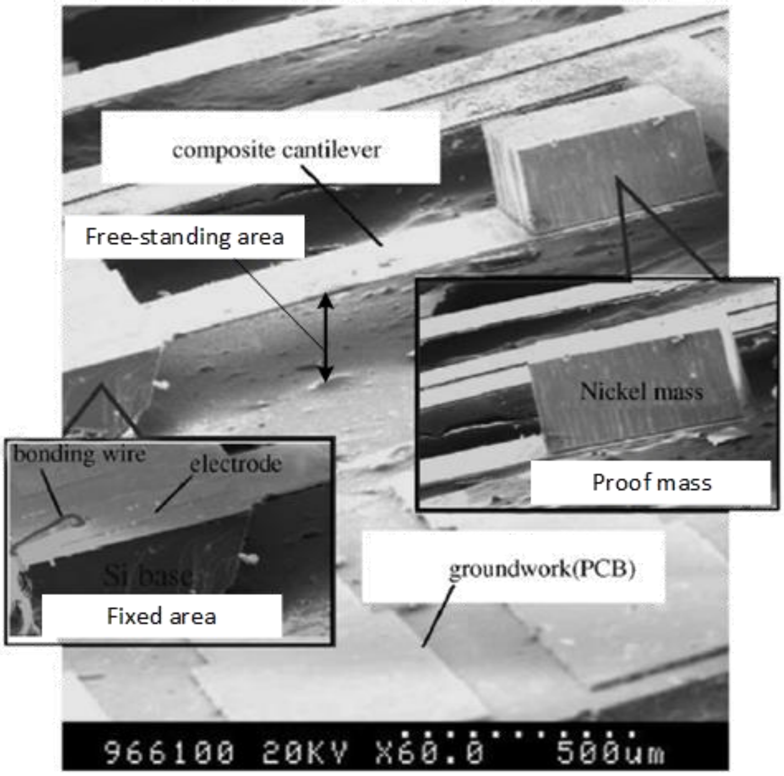

Figure 2-23: Cantilever fabricated using MEMS technology [54].

The power output of piezoelectric cantilever structure is highly influenced by the resonant frequency of the structure tuned with the ambient frequency. If the frequency does not match, the output power level will decrease dramatically [58]. The performance of piezoelectric elements is also influence by the output power level as reported in [55]. The piezoelectric elements which is subject to high pressure treatment shows higher power output level with 33.2 μW compared to 7.35 μW without the treatment.

### 2.5.3.2 Encastre beam structure

Encastre beam was demonstrated by *Zhang et al.* [59] which had fabricated a microbridge structure. The fabrication process started with the deposition of the Cr gate on the substrate by thermal evaporation, followed by patterning by photolithography and wet etching. An Al sacrificial layer was deposited by sputtering and patterned on top of the Cr gate by photolithography and wet etching. The conductive polymer film was then spin coated and patterned. Finally, the Al sacrificial layer was selectively removed by either phosphoric acid or a mixture of phosphoric acid and nitric acid to form a free-standing structure as in Figure 2-24.

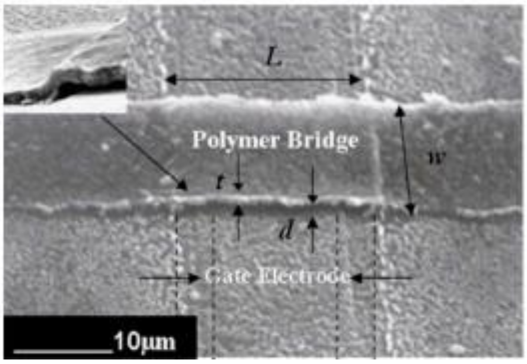

Figure 2-24: Polymer bridge structure fabricated on glass substrate [59].

In another work, *Olivares et al* [60] had demonstrated a microbridge consisting of a structural layer of silicon nitride supporting a piezoelectric actuator. The microbridges were fabricated by surface micromachining, using a silicon dioxide film deposited by photo-induced CVD as the sacrificial layer. This low density material has the advantage of being etched easily at room temperature using BHF. The microbridge structure was 350 μm-long by 80 μm-wide. The maximum deflection achieved by the microbridge is 3.5μm in the upward direction for an actuation voltage of 16V as shown in Figure 2-25.

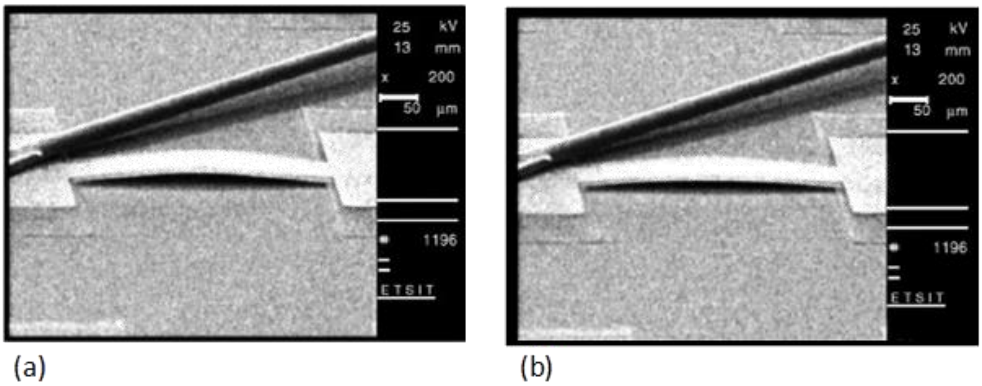

Figure 2-25: (a) Microbridge bended after applying voltage and (b) its equilibrium state [60].

An RF MEMS Bridge is another device fabricated using surface micromachining. *Mafinejad et al* [61] demonstrated an improved method to reduce the surface roughness of the device. A standard photolithography technique was used to fabricate RF MEMS switches. The sacrificial layer (AZ1512) should be sufficiently stable so it is not dissolved in acetone during the bridge patterning but also be able to be removed at the last fabrication step to release the bridge structure. A dry release method with an optimized recipe successfully released the bridge structure without buckling and no residues were left on the structure as in Figure 2-26.

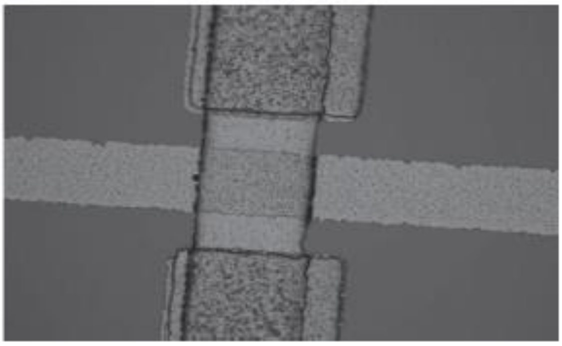

Figure 2-26: Bridge structure of RF MEMS switch fabricated using surface micromachining process [61].

#### 2.5.3.3 Diaphragm structure

In most cases, diaphragm structure is fabricated either using bulk micromachining or combination of 2 techniques which are surface and bulk micromachining.

*Dejaeger et. al.* [62] demonstrated MEMS digital loudspeaker fabricated using both surface and bulk micromachining. The digital loudspeaker consists of a set of acoustic transducer called speaklets. Each individual speaklet was deposited with a piezoelectric material sandwiched between the upper and lower electrodes, respectively in platinum and gold. Finally, the membrane was released by back side etching of the bulk silicon. Several variants of speaklets were presented with radius ranging from 400 to 2500 microns. The speaklets were produced on the same wafer as shown in Figure 2-27.

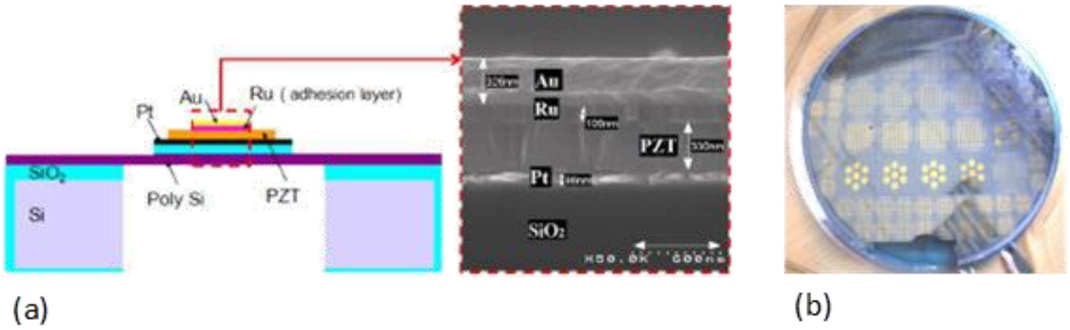

Figure 2-27: (a) Speaklet cross section and (b) various speaklet on the same wafer [62].

A circular and square diaphragm was fabricated and developed as a piezoelectric microphone by *Lee et al.* [63] A comparison between circular and square diaphragm showed that the sensitivity of a circular diaphragm is 197% higher than a square diaphragm. Figure 2-28 shows the simplified fabrication process of the diaphragms.

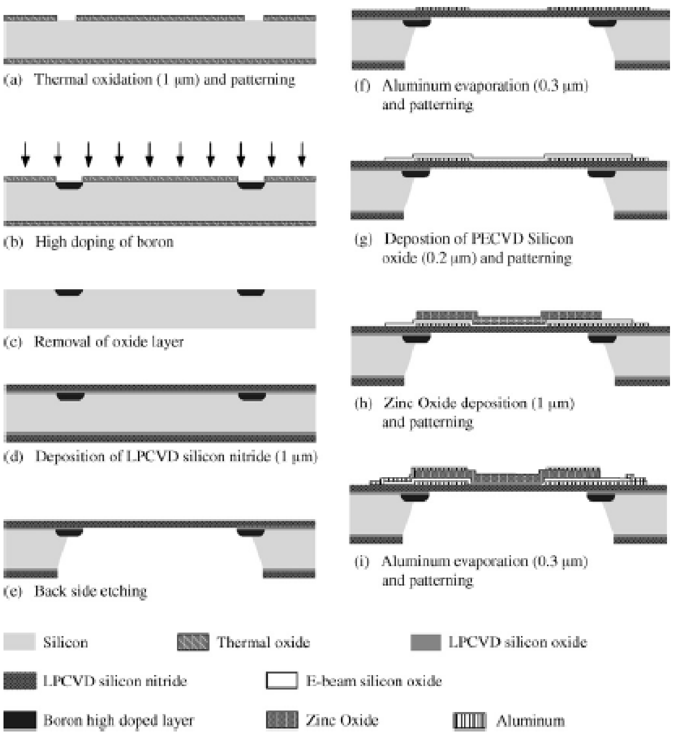

Figure 2-28: The fabrication process of piezoelectric microphone [63].

The conventional fabrication technique used to fabricate cantilever, encastre beam and diaphragm structure are not compatible with the fabric applications as the process such as spin coating and etching jeopardise the fabric properties.

## 2.6 Conclusions

The integration of electronic functions into textiles, while still preserving the intrinsic properties of fabrics, is very challenging. The integration and fabrication techniques play an important role in defining the properties of the resulting electronic textiles. For example a knitted textile is usually more stretchable compared to one realised using weaving techniques. Specialised yarns are needed in this technique to enable electronic functions. In comparison to other methods, screen-printing offers a promising solution due to its simplicity and the design flexibility that it offers. However, most printed e-textiles to date are planar structures with very limited three dimensional structure reported. It is, however, possible to fabricate simple 3 dimensional structures by implementing a sacrificial process using screen-printing techniques.

Sacrificial technology is commonly used in silicon MEMS fabrication processes. However, most of the silicon MEMS removal agents, used in surface micromachining processes, are not compatible with fabric substrates. Most of the materials used for removal are either acidic or toxic substances such as hydrofluoric-acid or toluene. Water soluble sacrificial materials such as PVA and low temperature processes such as TME are preferred as they are suitable for a textile substrate. Low temperature processes for structural materials compatible substrate and the other materials are limited when compared with MEMS materials. This layer will determine the mechanical properties of the resulting device. Selecting a structural material which has the appropriate properties and is compatible with the process is critical. Most of the pastes developed for screen-printing applications are formulated to suit the performance and application of the device. In this work, the implementation of low temperature curing and non-hazardous chemicals is necessary to retain the intrinsic properties of the fabric while achieving a 3D functional electronic textile.

This chapter also reviewed three different free-standing structures which are cantilever, encastre beam and diaphragm. Most of the structures reported in the literature are fabricated using conventional fabrication methods. These free-standing structure can also be achieved by screen-printing. High temperature process up to 920ºC, are not suitable for a sensitive substrate such as fabric. Curing temperatures of below 200ºC are more compatible for fabric substrates. However a limited number of devices have been demonstrated on fabrics. To date only applications such as a free-standing cantilever motion sensor on fabric and a micropump on Kapton have been presented. Comparison between PVA and TME sacrificial material also has not been evaluated. By using suitable materials, the feasibility to extend the applications on fabric using different structures (e.g. energy harvesting) are possible only by using screen-printing.

# 3. Substrate, structural and sacrificial material's evaluation and process optimisation

## 3.1 Introduction

The screen-printing process generally starts with paste selection or formulation, deposition, drying and curing and finally the characterisation process. The major difference in this study is the fabrication of the device on a flexible substrate using a low temperature process and also the application of sacrificial technology by screen-printing in order to produce a three dimensional free-standing structure. The materials used need to be compatible with fabric. Three different types of substrates are used, these being alumina, Kapton and fabric. Further investigation into the fabric surface roughness and the fabric properties is evaluated as this is the main substrate used in this work. Each of the substrates is used for different purposes and is discussed further in section 3.2.

There are different types of sacrificial material used to form a free-standing structure which have been previously discussed in chapter 2. However, there are two main types of sacrificial material which are low temperature processable and compatible with fabric. There are: sacrificial material 1 which is a thermally removed Trimethylolethane (TME) paste and sacrificial material 2, a water removed polyvinyl alcohol (PVA) paste. The printability, wettability and surface roughness of these sacrificial materials are investigated since there is little reported literature in this area.

Commercially available structural materials were used and investigated to illustrate the diversity of the process. There are four types of structural materials which are; Minico M 7000 Blue A dielectric, Gwent D2100824D2, SU8 and EFV4/4965 and these are categorised by the two main curing mechanisms used. There are ultra-violet (UV) curable structural material; SU8 and EFV4/4965, and thermally cured structural material; Minico M 7000 Blue A dielectric and Gwent D2100824D2. Each of the potential structural materials was evaluated mechanically and the two with the highest mechanical properties were further investigated; SU8 and Minico M 7000 Blue A.

The structural materials Minico and SU8 dielectric were evaluated for use with these sacrificial materials. Both sacrificial and structural layers were tested individually after which both sacrificial materials were investigated with both structural materials.

## 3.2 Substrate selection

The selection of a substrate is one of the most important factors to be considered in a screen-printing process. Differences in surface roughness, flexibility and working temperature will influence the printing parameters, the selection of printing materials and the quality of the print. There are three types of substrate used in this thesis. These are alumina, polyimide film (Kapton) and polyester cotton fabric.

### 3.2.1 Alumina substrate

Alumina ceramics, also known as aluminium oxide, are widely used in the field of microelectronics for packaging, sensors, actuators and passives. Ceramics with alumina content in the range of 94 to 97 % have been found to be suitable for the vast majority of applications.

An alumina substrate has the advantages of chemically stability, and has a working temperature of above 1000 °C. This makes alumina substrates suitable for screen-printing a wide variety of pastes with a range of curing temperatures. In addition, an alumina substrate provides a strong and rigid support for printed structures which will be the main purpose of the alumina substrate in this work. Table 3-1 shows the properties of a 96% alumina substrate.

Table 3-1: Alumina substrate properties [64].

| **Properties** | **ALSIMAG 614 $Al_2O_3$** |
|---|---|
| Maximum Working temperature °C | 1550 |
| Young's modulus $kg/cm^2$ | $3.3 \times 10^6$ |
| Thermal coefficient of linear expansion (below 300 °C) | $6.4 \times 10^{-6}$ / °C |

### 3.2.2 Kapton®

Kapton® is a flexible polyimide film. It has a unique combination of properties such as excellent chemical resistance and a wide range of working temperatures from -269℃ to 400℃. This makes it ideal for various applications including electrical insulation and flexible circuits [65].

In this work, Kapton substrate is attached to alumina substrate and used to fabricate the device. The smooth surface, high surface energy and chemical resistance allows wide range of pastes to be printed and evaluated. The smooth surface of the substrate also allows straight forward evaluation without effects arising from the surface roughness of the fabric. However, the surface roughness of the fabric can be reduced by printing an interface layer on the fabric surface and this is discussed further in the next section.

### 3.2.3 Fabrics

Fabrics, or textiles, are one of the most frequently encountered materials in daily life. Fabrics have a wide range of applications including clothing, fashion accessories such as bags and shoes and also furniture. Fabric can be classified into three types which are woven, non-woven and knitted yarns [66].

Woven fabrics are made by holding yarns in tension, known as the warp yarns, and weaving weft yarns between them. These yarns can be organic, synthetic, or a combination of the two.

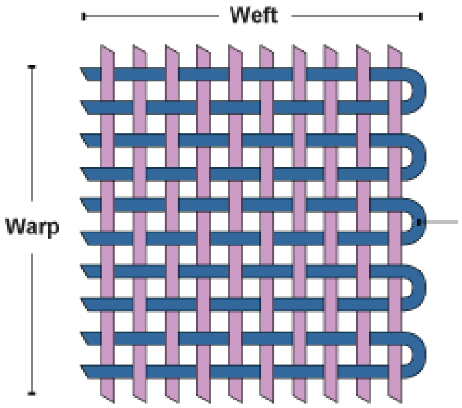

Figure 3-1: A weft and warp of the woven fabric.

Non-woven fabric is a material which is treated mechanically, thermally or chemically to bond a web of loose threads or fibres to form a fabric [33]. Non-woven fabrics have lower strength compared to woven fabrics and are usually used as filters or disposable masks.

Knitted fabric is constructed by looping together horizontally or vertically long lengths of yarn to form the fabric. This type of fabric is more stretchable compared to woven and non-woven fabrics.

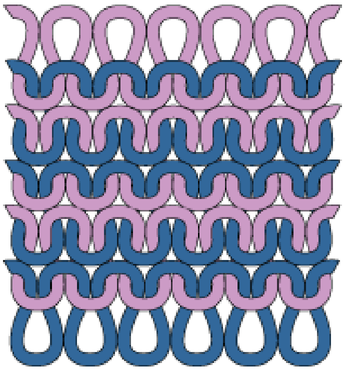

Figure 3-2: A construction of knitted fabric.

In this work, both Kapton and polyester cotton fabric were glued onto the alumina substrate. The alumina substrate provides a very strong support for the printing process. Kapton is used as an intermediate substrate, to evaluate flexibility without needing to work with the uneven surface of the fabric substrate. Thus, most of the work in this chapter will be printed on Kapton for evaluation. However, the polyester cotton fabric will be used in the final stage of the work.

A woven fabric composed of 65% polyester and 35% cotton has been selected as it is widely used in the clothing industry. Using a fabric substrate is more challenging due to the surface roughness of fabrics and their low working temperature.

#### 3.2.3.1 Surface roughness

To overcome the surface roughness problem, the fabric will be screen-printed with UoS-IF-UV4 paste which is patented and formulated at the University of Southampton. This forms a thin layer, known as an interface layer, which has been proven to greatly reduce surface roughness compared with the non-printed textile as illustrated in Figure 3-3.

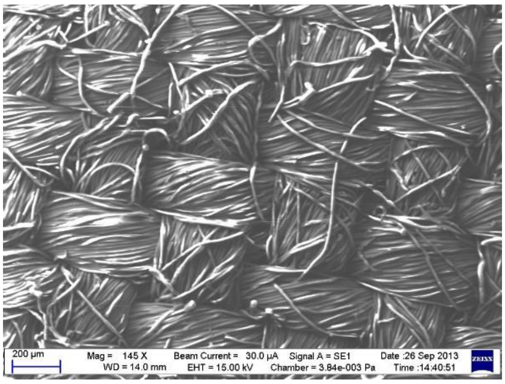

Figure 3-3: SEM image of polyester cotton without interface layer.

The first and second deposits of the interface layer are focusing on filling the woven gaps in the fabric. Figure 3-4 shows the condition of first deposit on fabric where by the woven structure and threads still can be observed. The second deposit was added and the woven structure visibility decreased compared to the first deposit as shown in Figure 3-5.

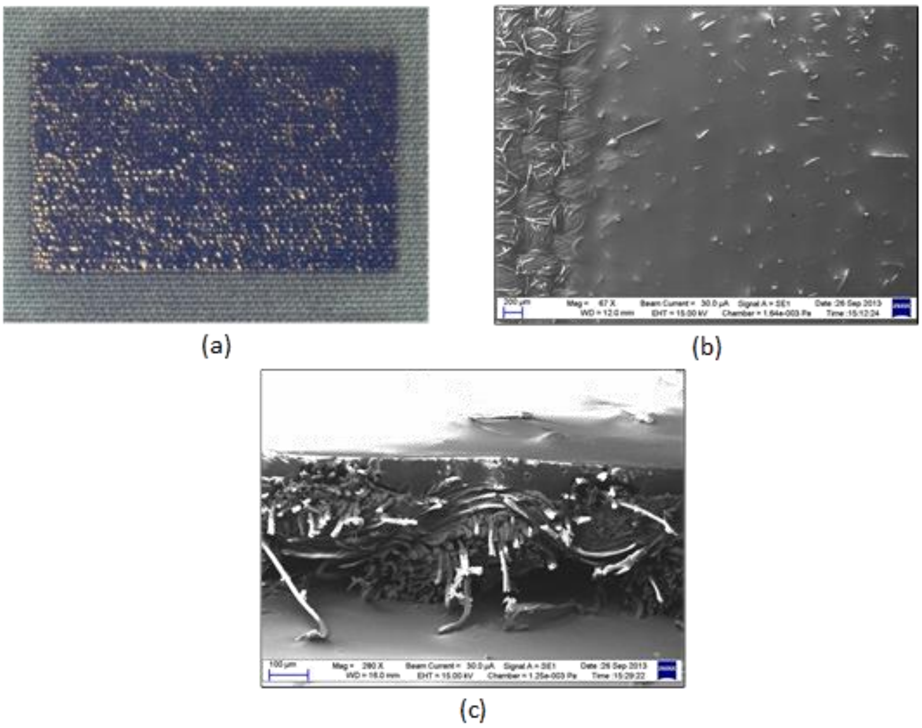

Figure 3-4: First deposit of (a) top down image of polyester cotton, (b) SEM image of printed interface and (c) cross section of printed layer.

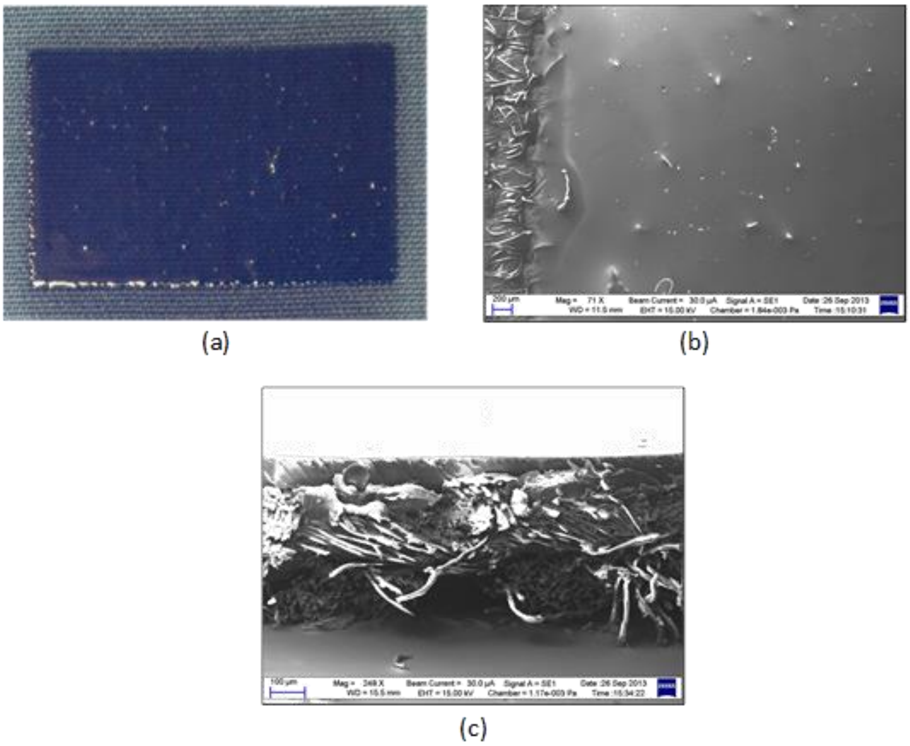

(a) (b)

(c)

Figure 3-5: Second deposit of (a) polyester cotton, (b) SEM image of printed surface and (c) cross section of printed interface layer.

The process continues with printing third and fourth deposit of interface layer. These layers are mainly to reduce the surface roughness and build up the thickness. As shown in Figure 3-6(b) and Figure 3-7(b) the surface roughness decreases with each layers and four deposits were found to be the optimal number to provide a smooth surface while retaining the intrinsic properties of the fabric [10].

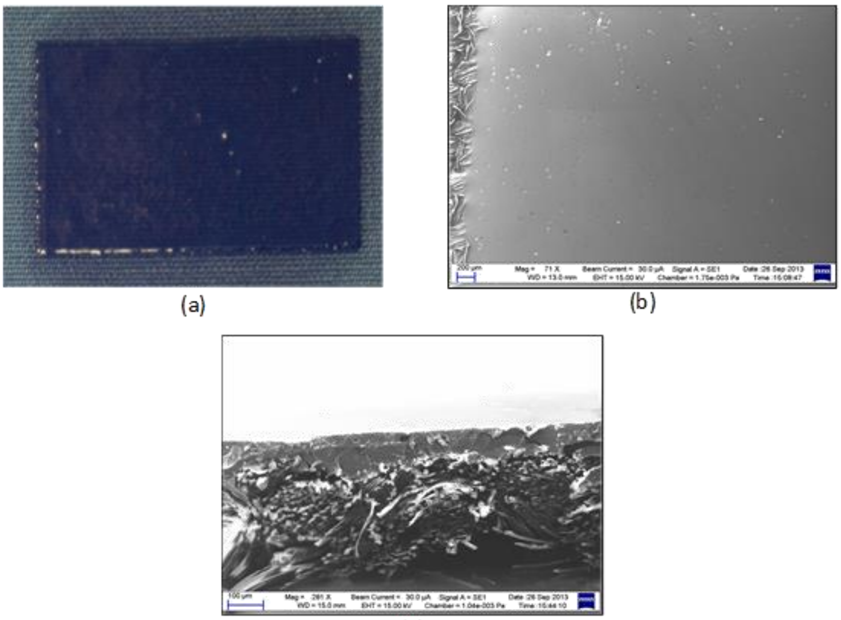

(a) (b)

(c)

Figure 3-6: Third deposit of interface layer on (a) polyester cotton, (b) top and (c) cross section image of SEM.

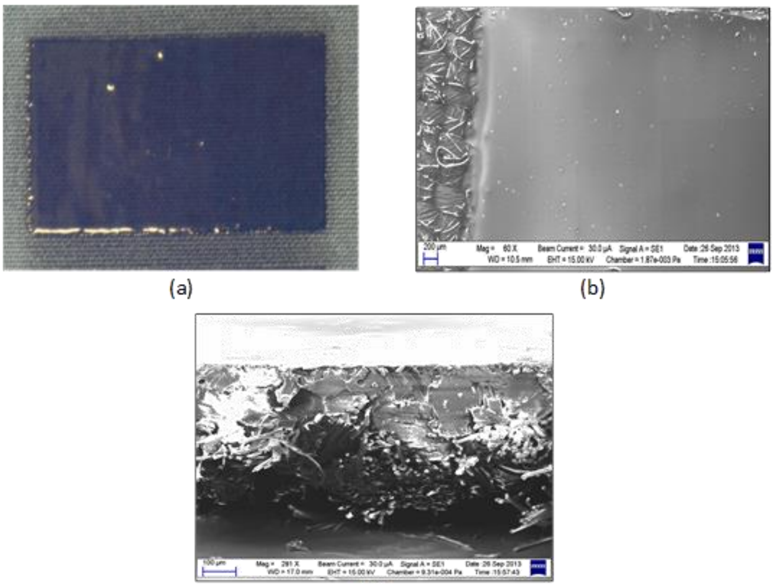

(a) (b)

(c)

Figure 3-7: Fourth and final deposit of interface layer on (a) polyester cotton, (b) top and (c) cross section image of SEM.

### 3.2.3.2 Discoloration and fabric properties

If the temperature used to cure the printed material is too high, sensitive substrates like fabric may be affected. Therefore it is very important to investigate the range of working temperatures of the standard polyester cotton fabric.

In this experiment, the fabrics were cut into rectangles measuring 9.5 x 3.0 cm and placed inside a box oven from temperature 80°C to 300°C for 1, 3, 5, 15, 30, 45 and 60 minutes respectively. The tensile properties of the fabric were then tested using the tensile machine described in section 3.4.2. Force and extension were recorded throughout the test.

A noticeable discoloration could be observed in the fabrics after 180°C at 45 minutes. However, at 200°C for 1 and 3 minutes no discolorations were observed. Figure 3-8 shows the fabric condition before and after the heating test was conducted. The fabric discoloration is more obvious in fabric which is colour dyed compared to the fabric which is not dyed. This might be due to a reaction between the fabric and the dye during the heating process which makes the discolouration are more obvious in the dyed fabric.

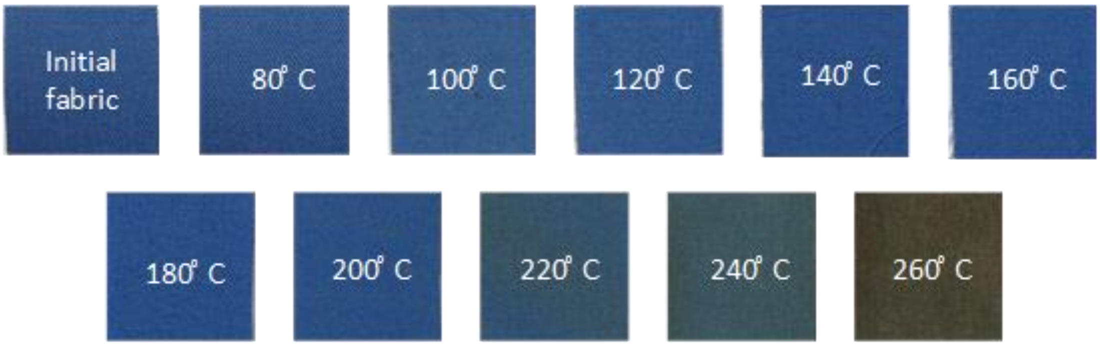

Figure 3-8: Fabric discoloration after heating process.

Before heating the tensile properties of the fabric were measured to be between 0.35 GPa to 0.4 GPa. The Young's modulus of the fabric heated at 200°C for 1 minute was found to be in the same range. The properties of the fabric heated above 200°C for 1 minute were found to be lower than this range, at 0.291 GPa. In particular at temperature 260°C the fabric becomes very brittle and the Young's modulus is indeterminate.

This indicates that lower temperatures such as 80°C can be used for more than 1 hour and it is possible to have higher temperatures of up to 200°C for shorter curing periods. Figure 3-9 and Figure 3-10 show the fabric properties after being heated for 1 minutes and at 240°C respectively.

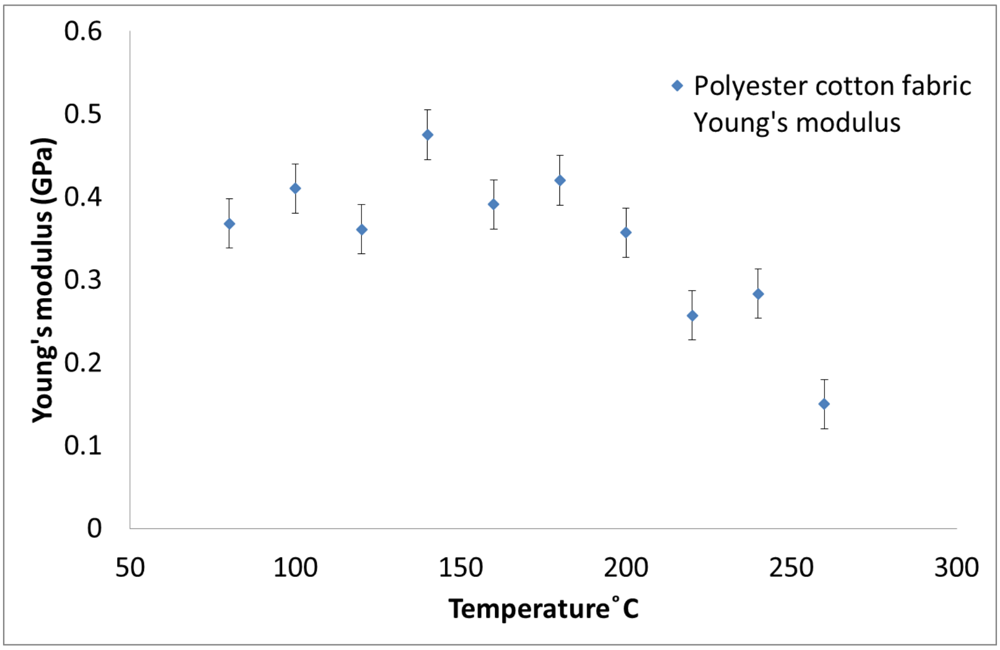

Figure 3-9: Fabric properties without printed layers after heating for 1 minute.

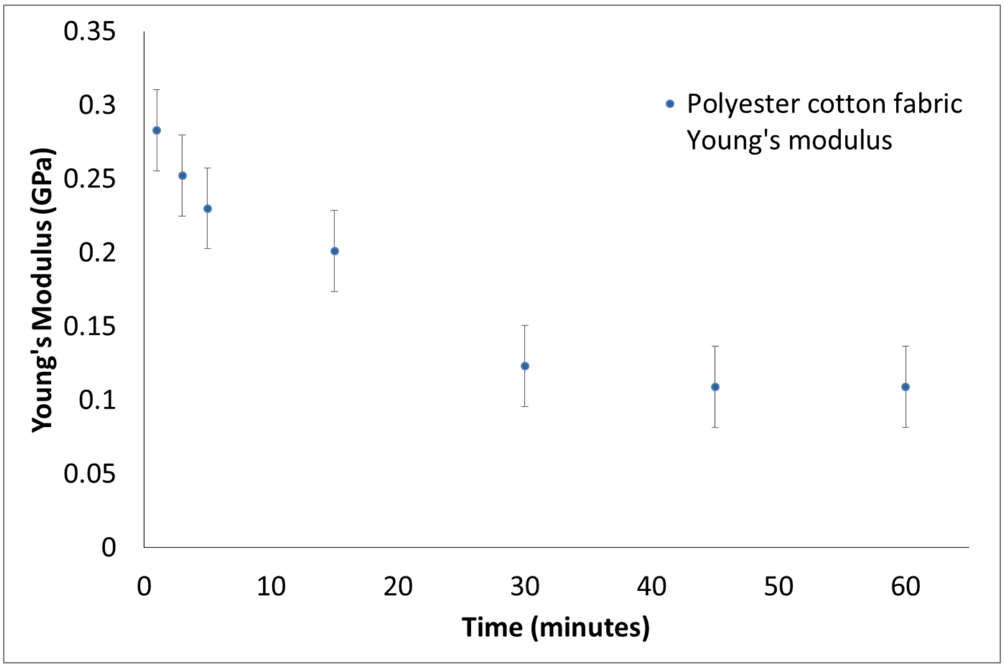

Figure 3-10: Fabric properties without printed layers after heated at 240˚C.

In this work, an estimation between 104 to 121 minutes of working time has been implemented for each sample. The samples are subjected to various temperatures of which the lowest temperature is 80ºC and the highest temperature is 130ºC. Both temperatures are compatible with fabric. *Komolafe et al* [67] had evaluated the average of Young's modulus after screen-printing fabrication which showed the Young's modulus reduces to 220 ± 19 MPa. However, the fabric condition shows no visible damage or discoloration and hence the process time and temperatures used in this work are suitable to be implement on a textile substrate.

## 3.3 Sacrificial layer evaluation

### 3.3.1 Introduction

As described in Chapter 2, there are several sacrificial materials which can potentially be used as a sacrificial layer in this work. These materials can be categorised by their removal mechanisms into solvent removal, water removal and thermal removal. The most suitable removal mechanisms for a fabric substrate are water removal and thermal removal, as solvent removal is not compatible with organic materials such as cotton in the fabric.

In the following section an evaluation of these two types of sacrificial material will be conducted with emphasis on finding the appropriate printing parameters, the surface tension of the printed ink and the cured surface roughness.

### 3.3.2 Sacrificial material 1 (Thermally removed)

Trimethylolethane (TME) is a sacrificial material that has plastic crystal properties. This plastic crystal is an intermediate form between the transition point ($T_t$) and melting point ($T_m$) as shown in

Figure 3-11. The transition gap of plastic crystal to gas ($T_m$ to $T_v$) is very narrow, which allows the TME to sublimate passing through and ignoring the liquid phase. This will reduce the potential for unwanted adherence and structure deformation while the sacrificial layer is being removed.

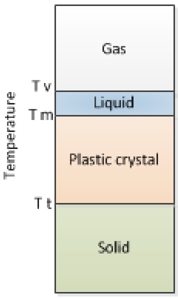

Figure 3-11: Phases in plastic crystals [68].

The temperature of the removal process must not exceed the previously established working temperature of the standard poly-cotton fabric. More details on sacrificial material 1 formulation have been investigated by *Wei et al* in his work [22].

### 3.3.3 Sacrificial material 2 (Water removed)

The other category of sacrificial material which can be used on fabric is sacrificial material 2, of which is the removal mechanism is water. Polyvinyl alcohol (PVA) is the most commercially important water soluble polymer used in the plastics industries. It is odourless, biodegradable and biocompatible, earning it a reputation as a 'green polymer' [69]. It is produced commercially by the hydrolysis of poly (vinyl acetate).

This material can be divided into two main types; fully hydrolysed and partly hydrolysed copolymers. This material is used in a number of applications such as a textile and paper coating, in adhesive technology and also in the food and pharmaceutical industries. [70]

In this work, PVA is used as a sacrificial layer as described in chapter 2. The PVA based sacrificial layer (UoS-SF-24), formulated at University of Southampton, Faculty of Physical Sciences and Engineering is used in this experiment.

#### 3.3.3.1 Viscosity measurement

The paste is rheological and the viscosity properties of the paste is highly influence the printing quality of the design. All viscosity measurements were performed using a Brookfield CAP 1000+ with a spindle cone 4 and rotation speed of 10 rpm. The measurement was taken over 15 minutes and Figure 3-12 shows the average viscosity of sacrificial material 2 was 7.34 Pa.s. Based on an experimental evaluation and observation during fabrication process, the viscosity which is most suitable for printing process using a 120 mesh screen was found to be around 7.0 to 10.0 Pa.s.

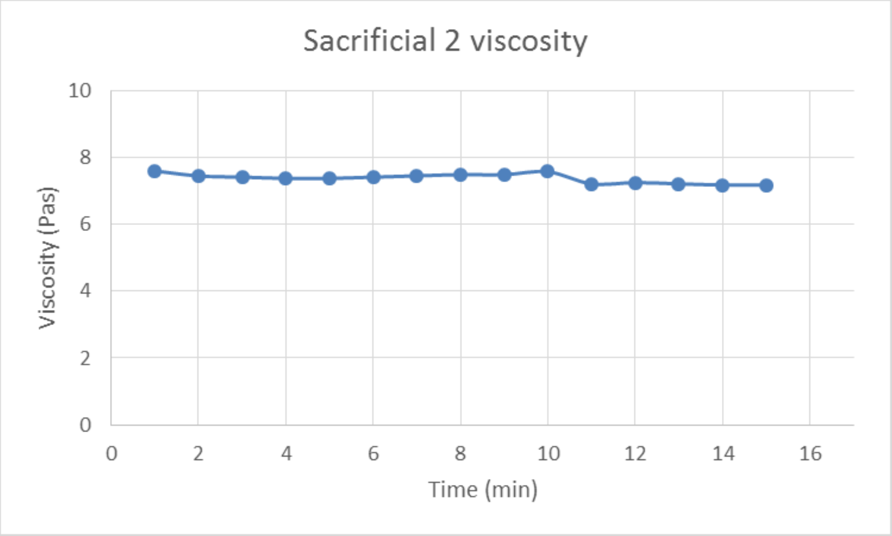

Figure 3-12: Sacrificial material 2 viscosity.

Lower than 7.0 Pa.s resulted in a thinner printed layer with more deposition needed to achieve the desired thicknesses. The viscosity of sacrificial material 2 increases, to >10.0 Pa.s after several uses of the paste due to the evaporation of solvent. The paste became sticky, which results in uneven printing and the printed layers being stuck to the screen.

### 3.3.4 Deposition parameters

The identification of the optimum printing parameters is very important in order to achieve good pattern definition of the printed design. Incomplete printing or a smudged pattern is often caused by, for example, using a printing gap that is too small or too large [64, 71]. In this work, the screen used for paste deposition was a 120T polyester mesh with a 40μm emulsion thickness. The screen was designed using L-edit as shown in Figure 3-13. The blue outlines show the screen for the sacrificial layer while the pink colour is the screen for the structural layer. The same design for structural layer was used to fabricate a stencil screen with 100μm thickness.

The designs have two primary purposes; to investigate the limitations of printing in terms of size and pattern definition, and to examine the effectiveness of the removal process under different removal conditions.

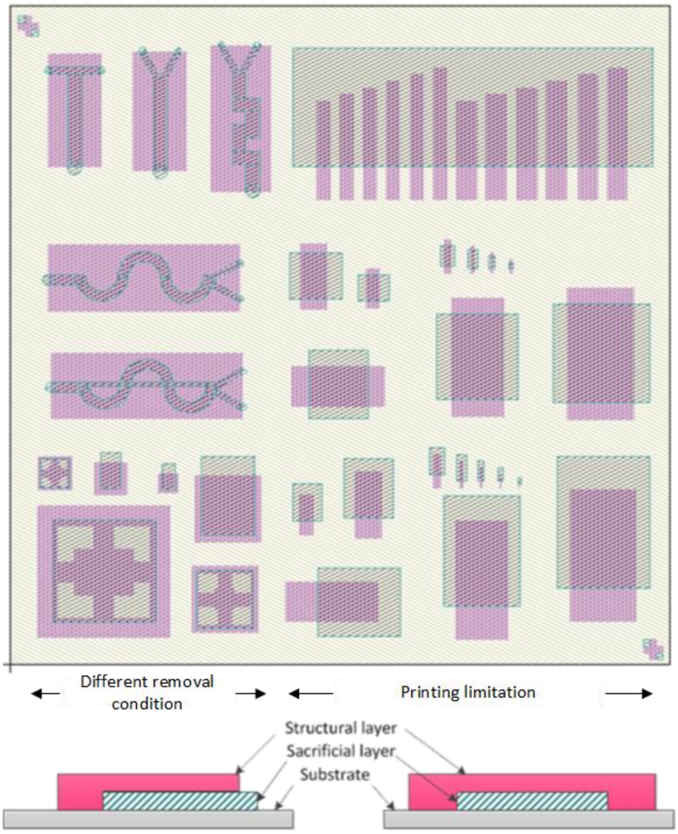

Figure 3-13: Top: Screen layout designed using L-edit and bottom: cross-section diagram of structure.

#### 3.3.4.1 Sacrificial material 1 (Thermally removed)

The sacrificial material 1 was printed on a Kapton substrate as shown in Figure 3-14 using a 120T polyester mesh with a 40µm emulsion thickness screen. The printed pattern was dried in a box oven for 5 minutes at 80ºC. The optimum drying temperature was previously investigated by *Wei et al* [22] and will not be discussed further.

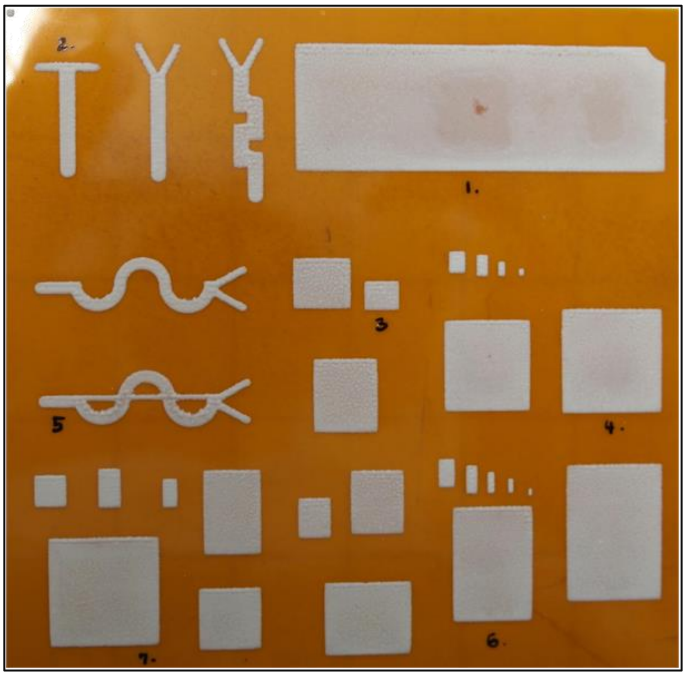

Figure 3-14: Printed pattern of sacrificial material 1.

The desired thickness of the printed layer can be achieved by printing and curing the sacrificial material 1 repeatedly until the required thickness is achieved. The sacrificial material 1 was printed as 7 layers with 2 depositions for each layer with a total thickness of 115µm. The optimum deposition conditions for the printed layer was determined by adjusting the critical parameters especially the printing gap. This is to ensure a complete pattern is consistently achieved by each printing process. Table 3-2 presents the optimum deposition parameters for sacrificial material 1.

Table 3-2: Sacrificial material 1 deposition parameter.

| **Material** | **Sacrificial material 1 UoS-TME-b** |
|---|---|
| Pressure (kg) | 6.0 |
| Gap (mm) | 1.5 |
| Flood speed (mm/s) | 70 |
| Printing speed (mm/s) | 70 |
| Number of deposits | 2 |
| Screen | 120T polyester mesh screen, 40µm emulsion |

The advantages of sacrificial material 1 are ease of printing and the ability to control the removal temperature as determined by Wei et al [22]. However, the pattern definition of the printed layers show an uneven surface especially for smaller designs and also at the edge of the larger pattern. The condition of the surface will be discussed further in section 3.2.3.1.

### 3.3.4.2 Sacrificial material 2 (Water removed)

The sacrificial material 2 is a water-soluble PVA based sacrificial material. The pattern was printed using the same design on an alumina substrate and then dried in a box oven for 3 minutes at 80°C. The drying temperature for sacrificial material 2 is the same as for sacrificial material 1. However, the drying time is 2 minutes shorter since the solvent in the paste evaporates much faster than for sacrificial material 1. A pink pigment was applied in the PVA sacrificial paste by thoroughly mixing the paste with magnetic stirrer on top of a hot plate. The printed patterns are easier to observe with pigment as shown in Figure 3-15.

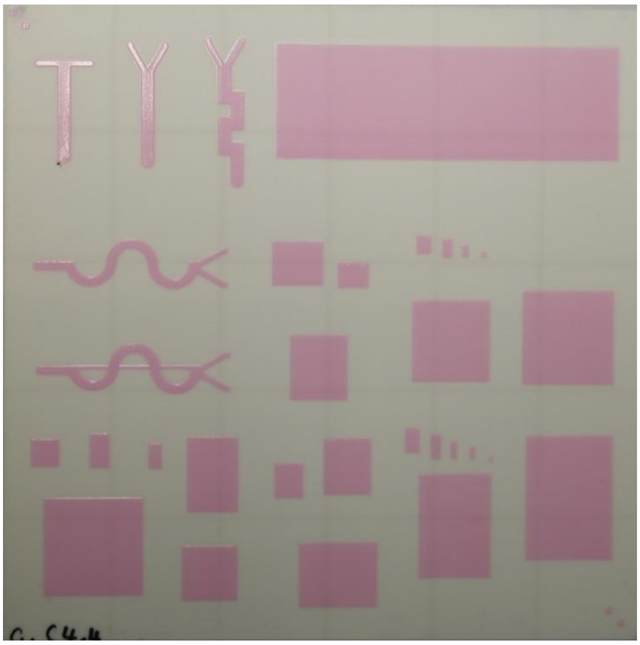

Figure 3-15: Printed PVA sacrificial layer on an alumina tile.

The printing parameters were experimentally evaluated by adjusting the values given in Table 3-3. The optimum values were achieved by observing the printing pattern on the alumina substrate after conducting printing tests. Printing errors such as incomplete pattern or smeared edges indicate that the printing parameters must be adjusted. The sacrificial material 2 needs 6 layers with 2 depositions to achieve the same thickness as sacrificial material 1. Patterns as fine as 500µm was successfully printed and the surface of printed layers were smooth. The surface roughness of both materials will be discuss further in section 3.3.6. However, the disadvantage of sacrificial material 2 is it easily dries at the screen-printing stage which causes the printed layer to pull off or stick to the screen.

Table 3-3: Printing parameters for sacrificial layers.

| Material | Sacrificial material 2<br>UoS-SF-24 |
|---|---|
| Pressure (kg) | 6.5 |
| Gap (mm) | 1 |
| Flood speed (mm/s) | 70 |
| Printing speed (mm/s) | 50 |
| Number of deposits | 2 |
| Screen | 120T polyester mesh screen, 40µm emulsion |

The next stage in the printing process is printing the structural layer on top of the sacrificial layer, which will be described in section 3.4.

### 3.3.5 Contact angle

Contact angle measurements are used to estimate the wettability of the surface of a material. The wettability is important to ensure bonding or adherence of two materials. Small contact angle (e.g. < 90°) can be observed when the liquid spread on the surface corresponds to high wettability or hydrophilic surface; while large contact angle (e.g. > 90°) corresponds to low wettability which minimized its contact with the surface and form a compact liquid droplet or known as hydrophobic surface as illustrated in Figure 3-16 [72].

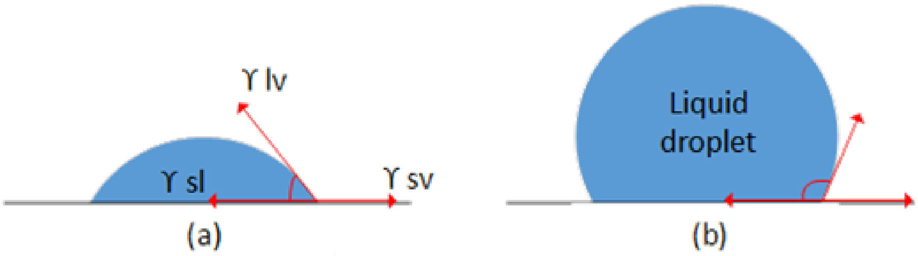

Figure 3-16: Illustration of water droplet on solid surface (a) high wettability with contact angle <90° (hydrophilic surface) and (b) low wettability with contact angle >90° (hydrophobic surface).

There are two important parameters which define the contact angle of a droplet on a surface: these are the angle interaction of the liquid-solid interface ($\Upsilon_{sl}$) and the liquid-vapour interface ($\Upsilon_{lv}$). The interfaces involved are solid, liquid and vapour and these interfaces are known as a three phase contact line as shown in Figure 3-17, while Figure 3-18 shows the actual water droplet on sacrificial layer.

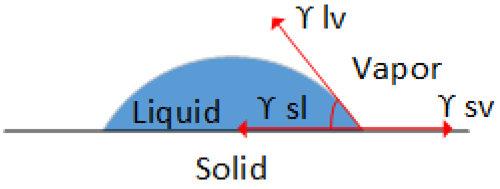

Figure 3-17: Illustration of contact angle between a solid material and a liquid droplet.

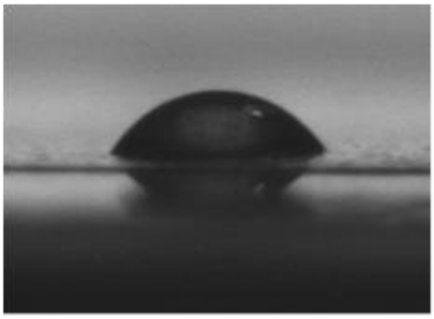

Figure 3-18 : Water droplet test on SF-24 layer.

The measurement was taken using a Kruss DSA30 Contact Angle Measuring Instrument using the Owens-Wendt method [73]. In this method, two different liquids (bipolar and polar) with known surface tensions are required to determine the surface energy. The liquids used were water with a bipolar component and diiodomethane with a polar component. 5 samples were each cured at different temperatures: 80°C, 90°C, 100°C, and 110°C and120°C. Table 3-4 shows the contact angle and calculated surface energy of each sample.

Table 3-4: Contact angle and surface energy measurements for SF-24 cured at various temperatures.

| Temperature (°C) | 80 | 90 | 100 | 110 | 120 |
|---|---|---|---|---|---|
| Water contact angle (deg) | 32.1 | 37.0 | 33.3 | 32.4 | 31.3 |
| Diiodmethane contact angle (deg) | 78.9 | 71.4 | 69.3 | 70.4 | 77.1 |
| Surface energy (mN/m) | 62.1 | 59.2 | 61.8 | 62.2 | 62.6 |

There is no significant effect on the surface tension of the sacrificial layer when the curing temperature is varied between 80-120°C and each sample has relatively high surface energy indicating high wettability for subsequent layers to be deposited. Therefore, UoS-SF-24 will be dried at 80°C for 3 minutes to minimise the effect on the fabric.

### 3.3.6 Surface roughness

The surface roughness of a material is important in understanding the friction between two sliding surfaces and can affect the rate of wear in a mechanical device. In printing technology, the surface roughness of a substrate or printed layer can affect the pattern definition of a subsequently printed layer. It will also affect the adhesion of a printed layer and can affect the operation of printed electronic components. For example, the noise in a printed resistor is known to be higher with a rough surface because the resistor is less uniform [64].

Techniques for measuring surface roughness can be divided into two categories depending on whether the equipment makes contact with the measured surface during the measurement. In screen-printing technology, a contact-type stylus profiler with electronic amplification is the most commonly used method of measuring surface roughness. In this method the stylus is loaded on the surface to be measured and then moved across the surface at a constant velocity. The stylus follows the contours of the surface and its vertical position is monitored to provide a measure of the surface roughness [74].

In this work a KLA-TENCOR P-11 surface profiler was used to measure the surface roughness of the screen-printed SF-24 and TME layers. Fixed stylus parameters were developed to calculate the surface roughness of each printed sample. Table 3-5 shows the parameters used to measure the surface roughness at different points on the sacrificial layer as shown in Figure 3-19.

Table 3-5: Stylus surface roughness parameter setup.

| **Stylus parameter** | **Value** |
|---|---|
| Scan length (μm) | 2000 |
| Scan speed (μm/s) | 50 |
| Sampling rate (Hz) | 50 |
| Stylus force (mg) | 1 |
| Stylus radius (μm) | 2 |

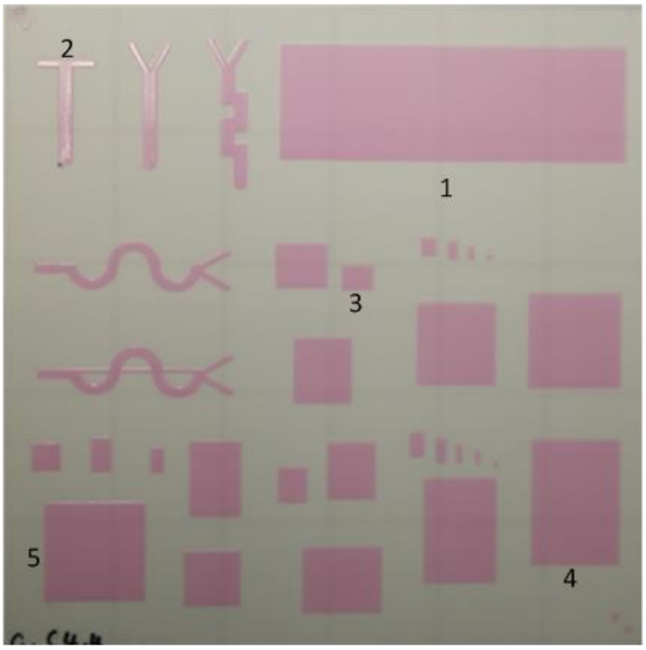

Figure 3-19 : Different position of surface roughness.

In this work a centre line average is taken as the method for measuring the surface roughness of the sample as suggested by T.R Thomas [75]. The centre line average can be defined as shown in Equations (1) and (2).

$$R_{CLA} = \frac{1}{L}\int_0^L |Z_i| dx \tag{1}$$

$$\approx \frac{|Z_1| + |Z_2| + |Z_3| + \cdots |Z_n|}{n} \tag{2}$$

L, Z and n are the sampling length, sampling height and sampling numbers respectively. 3 readings from each position on each material were evaluated and the average result was taken.

Based on this calculation, PVA has a smoother surface than TME. The lowest surface roughness reading from the PVA surfaces was 0.424µm, at position 3. However, for the TME surface, the larger pattern designs such as position 1, 4 and 5 have a smoother surface compared to the thin line patterns such as position 2. The average surface roughness for each position with each material is shown in Table 3-6. The examples of surface profiles for TME and PVA are shown in Figure 3-20 and Figure 3-21 respectively.

Table 3-6: Surface roughness of PVA and TME at each position.

| **Sample position** | **1** | **2** | **3** | **4** | **5** |
|---|---|---|---|---|---|
| TME surface roughness (µm) | 2.660 | 11.128 | 6.775 | 3.359 | 4.177 |
| PVA surface roughness (µm) | 1.825 | 0.736 | 0.424 | 2.170 | 4.599 |

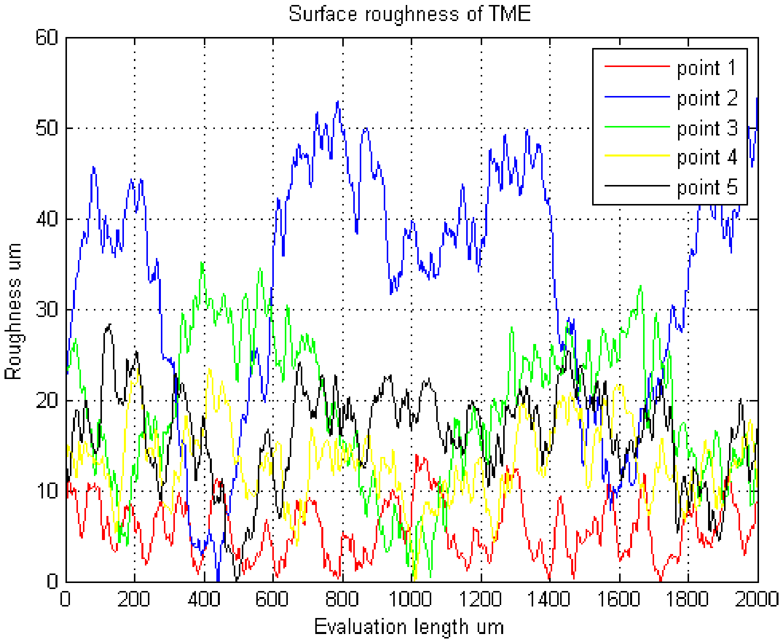

Figure 3-20: Example surface profiles for printed TME.

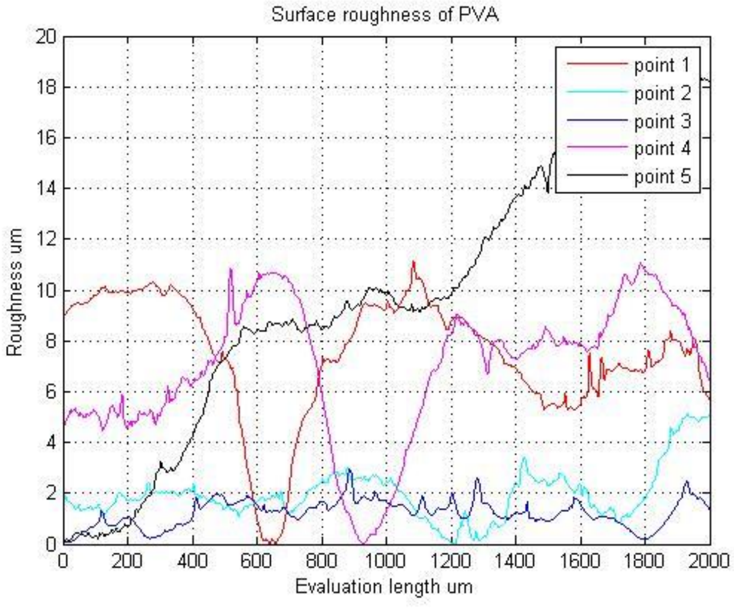

Figure 3-21: Example surface profiles for printed PVA.

## 3.4 Structural layer evaluation

### 3.4.1 Introduction

A structural material is defined as any material whose primary function is to be load or stress bearing [51]. The most common structural material used in micromachining fabrication technology is silicon [76]. This is due to its excellent mechanical properties which make it ideal for fabricating structures on the micro and nano scale and for the integration of electronic circuits and sensors. Device fabricated using silicon either as substrate or as a structural material is given in chapter 2 section 2.4.3. Table 3-7 gives a summary of some structural materials using various types of micro-fabrication process. Typically, these materials are deposited either using spin coating or photolithography.

Table 3-7: Structural materials used in micro-fabrication.

| Structural material | Deposition method | Application | Reference |
|---|---|---|---|
| Polyamide | Spin coating | Free-standing transducer | [77] |
| Polysilicon | LPCVD | Resonator | [11] |
| SU8 | Photolithography | Bridge structure | [78] |
| Poly(n-propyl methscrylate) PPMA | Micromolding | Beam structure | [79] |

Fabricating structures on a flexible fabric substrate places several restrictions on the process that can be used. There are several criteria that a structural material must meet to be compatible with a textile printing process. The requirements of the structural paste used in this process are described below.

- A curing time and temperature that is compatible with the fabric substrate (< 200°C) and that will not cause removal of the sacrificial layer such as TME (<160°C)
- No reaction with previous or subsequent layers. Reaction between sacrificial and structural layers resulted in the structural layer adhering to the substrate.
- Good mechanical properties to ensure a sturdy printed structure after the curing process.
- Ease of deposition to provide a smooth and fast printing process (< 1 minute for one deposition).
- Good pattern definition is very important especially for the conductive paste.

There are several pastes which can potentially be used as a structural material for this work. Structural materials can be divided by their curing mechanism into thermally curable and UV curable structural materials. Thermally curable structural materials must have a low temperature curing process to be compatible with the substrate and sacrificial layer. There are no such restrictions on the UV curing process so all UV curable structural materials are candidates. These pastes will be printed on top of both of the previously examined sacrificial layers: water removable PVA and thermally removable TME. The commercially available screen-printable paste which are SU8, Minico, Gwent D2100824D2 and EFV4 are evaluated in terms of printability, compatibility, pattern definition and tensile properties.

### 3.4.2 Mechanical properties

The mechanical behaviour of a micro-fabricated structure cannot be understood without the knowledge of mechanical properties of the material, such as its tensile strength and Young's modulus [80]. Young's modulus is a measure of stiffness and is related to the strength of atomic bonds between particles in the material under test. A tensile test measures the resistance of a material to elastic deformation when a tensile stress is applied. The Young's modulus E of a material is defined as the tensile stress $\sigma$ applied divided by the extension due to that stress $\varepsilon$.

$$E = \frac{\sigma}{\varepsilon} \tag{3}$$

A stiff material has a high Young's modulus because the extension is very low when a high stress is applied, whereas a pliable material such as rubber has a low Young's modulus and deforms considerably at low levels of stress. There are several ways to determine these mechanical properties such as tensile tests [81], resonance methods [80] and indentation methods [82].

A tensile test is conducted by moulding the material into a dumbbell shape. The dumbbell shape is then loaded into the tensile machine. The tensile machine then extends the sample until it fails while recording the tensile stress and extension. The Young's Modulus can be calculated from these readings. This technique is not suitable for very brittle materials due to the nature of the process.

Another method which can be used to calculate the Young's modulus of a material is resonance evaluation. Petersen et al [83] fabricated cantilever beams and then vibrated them electrostatically. The Young's modulus was determined from the mechanical resonant frequency for a given mechanical structure. The same method also has been implemented by *Kiesewetter et al* [80] with lower levels of error using three different excitation methods; photothermal, acoustic and mechanical.

An indentation test can also be used to measure the Young's modulus of a material. An indenter tip with known mechanical properties is used to indent the surface of a sample and the position of the indenter is measured with increasing load. Time, force, and displacement are recorded throughout the test. The depth of the indentation at different loads can be used to calculate the Young's Modulus.

In this work, a three-sided pyramidal Berkovich diamond tip is used for an indentation test as shown in Figure 3-22. 5 different samples were prepared for evaluation. 4 of the materials these being SU8, Minico, Gwent D2100824D2 and EFV4 dielectric were prepared by printing. As SU8 has also been used in micromachining fabrication process, one sample of SU8 by spin coating was also been prepared for comparison with printing. The Minico and Gwent D2100824D2 dielectric was cured using a box oven at a temperature of 160°C for 30 minutes and 130°C for 15 minutes respectively. SU8 and EFV4 were cured using a UV cabinet for 120 seconds. The maximum load applied was 1 mN and 20 indents were performed on each sample. The results are shown in Table 3-8.

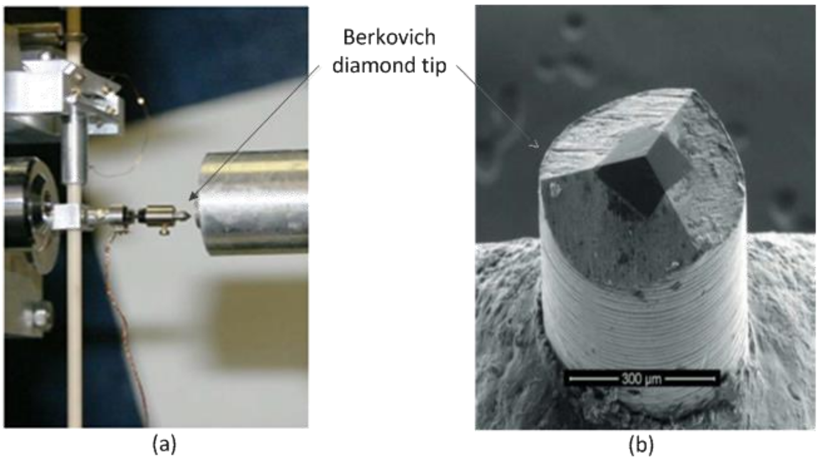

Figure 3-22: (a) Indentation test and (b) Berkovich diamond tip used in the test.

Table 3-8: Young's modulus measured by indentation for 5 different materials.

| Materials | Young's modulus | Literature | References |
|---|---|---|---|
| SU8 (spin-coating) | 5265 MPa | 4950±420 MPa | [84, 85] |
| SU8 (printed) | 2692 MPa | N/A | N/A |
| Minico M 7000 | 5523 MPa | N/A | N/A |
| Gwent D2100824D2 | 1523 MPa | N/A | N/A |
| EFV4/4965 | 840.4 MPa | ~500 MPa | [22] |

*N/A : not available

The Minico dielectric is the stiffest with a Young's modulus of 5523 MPa immediately followed by spin-coated SU8, at 5265 MPa. Spin-coated SU8, however, shows less plastic deformation compared to Minico. Figure 3-23 shows the load and displacement graph to calculate the indentation modulus of the material.

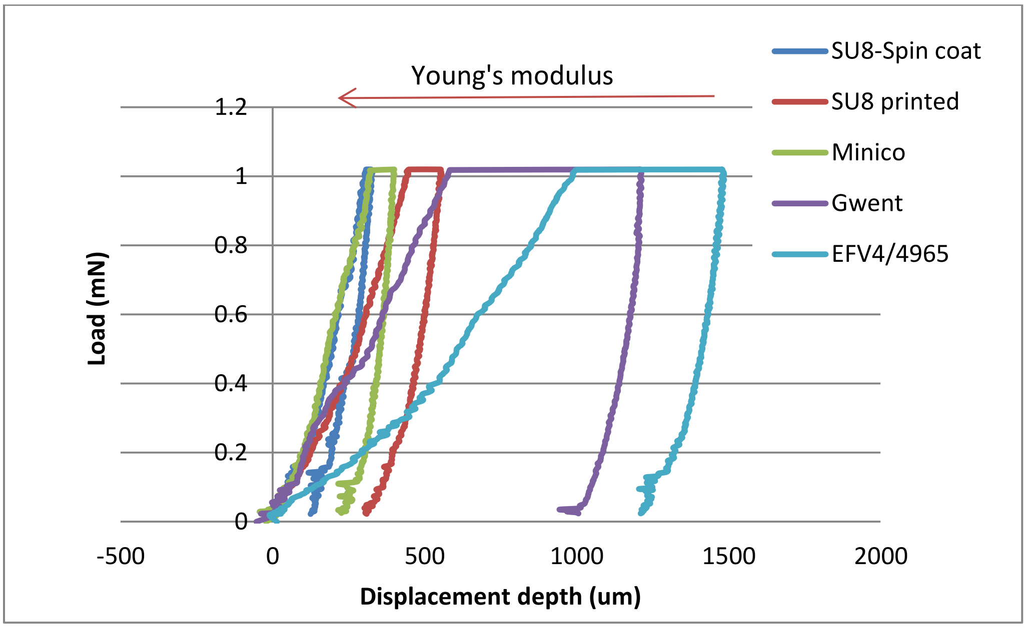

Figure 3-23: Indentation reading from 4 different materials.

Further evaluation was performed with only SU8 and Minico dielectric pastes, because they have greater stiffness, are compatible with the printing process and demonstrated a very good adhesion to the substrate. A stiff structural material is required in this process because this layer will be the main structure of the design. Hence, the stiffest material will provide the most durable free-standing structure. Therefore, a high Young's modulus are required. Further investigation will be conducted on those materials with the first and second highest Young's modulus which are the Minico dielectric and SU8.

### 3.4.3 Structural material 1 (SU8 dielectric)

#### 3.4.3.1 Introduction

Structural material 1 which is SU-8 is an epoxy based photoresist. It was first commercialised by IBM and distributed by Microchem from1996. There are three main components of SU-8; Bisphenol A Novolak epoxy oligomer, an organic solvent in which this epoxy is dissolved and the photoinitiator to cross-link it when UV light is applied.

Bisphenol A Novolak epoxy oligomer is also known as EPON™ Resin SU8. The number '8' in the SU8 refers to the number of epoxy groups in the oligomer as shown in Figure 3-24. Momentive Specialty Chemical Inc. defines SU8 as "a polymeric solid epoxy novolac resin possessing average epoxide group functionality of around eight" [86]. This high number of reactive epoxy functional sites per monomer molecule allows a high degree of crosslinking during the curing process, which contributes to its high stiffness.

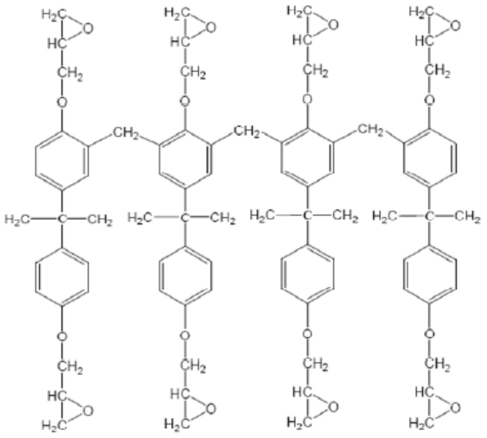

Figure 3-24: Molecular structure of SU8 monomer.

*Marijana et al* [87] tested 8 organic solvents to dissolve SU8. There are gamma-butyrolacton (GBL), propylene glycon methyl ether acetate (PGMEA), methyl-ethyl ketone (MEK), acetone, benzene, 1-methyl-2-pyrolidone (1M2P), N,N-Dimenthylacetamide (NNDMAA), and distilled water. From the tested solvents, only 5 out of 8 were found to be suitable solvents for SU8. GBL is usually used as the organic solvent for SU8 due to the capability of the GBL to copolymerise with SU8 to bridge two neighbouring epoxy groups, leading to a longer network and crosslink as reported by Marijina et al and Zhang et al [87, 88].

The photo-active or photoinitiator compound used in SU8 is an onium salt called tri-aryl-sulfonium. This salt will be added to generate the crosslinks between resin particles. The thickness of the processed SU8 layer depends on the viscosity of the SU8 formulation, which can be adjusted by changing the weight ratio of the SU8 resin to the solvent [84].

#### 3.4.3.2 Deposition parameters

The screen used for printing structural layers was a 12"x 12" polyester screen with 68-55 mesh and 40 micron emulsion thickness. The screen was designed using L-edit as shown in Figure 3-13 in section 3.3.4. The printing parameters for the structural layer are defined as shown in Table 3-9.

Table 3-9: Printing and curing parameters for SU8.

| Types of screen | Polyester screen | Stencil screen |
|---|---|---|
| Pressure (kg) | 6.5 | 0.5 |
| Gap (mm) | 1 | 0.1 |
| Flood speed (mm/s) | 70 | 70 |
| Printing speed (mm/s) | 50 | 50 |
| Deposition | 1 | 1 |
| Curing condition | 60 sec UV exposure | |

#### 3.4.3.3 Experimental results

Structural material 1 was printed on top of PVA and TME sacrificial layers printed with 68-55 polyester and a stencil screen. There was no reaction observed between SU8 and either of the sacrificial layers. However, there were problems with air bubbles and poor pattern definition of the SU8 layer. Figure 3-25 shows the air bubbles in the SU8 after printing.

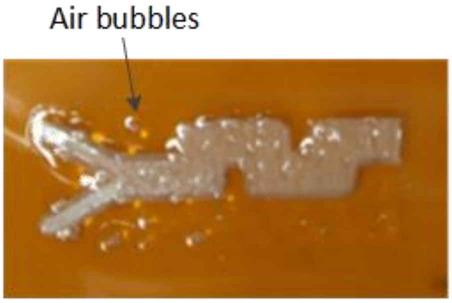

Figure 3-25: Air bubble form after printing.

Air bubbles were produced due to the polyester screen, where air bubbles are introduced to the SU-8 paste when it passes through the polyester mesh. The air bubbles were significantly reduced when the stencil screen was used, as shown in Figure 3-26. A smooth structural layer was produced by printing 2 layers of SU8 using a stencil screen. The thickness of the printed layer was around 200 µm.

Figure 3-26: (a) Printed using polyester screen (b) Printed using stencil screen.

The pattern definition for SU8, and especially for the SU8 cantilever structure, shows a huge difference between samples printed on PVA and those printed on TME. The structure printed on PVA shows better pattern definition due to the relative smoothness surface of the sacrificial layer. Figure 3-27 shows the structure printed on TME bleeds significantly more than that on PVA.

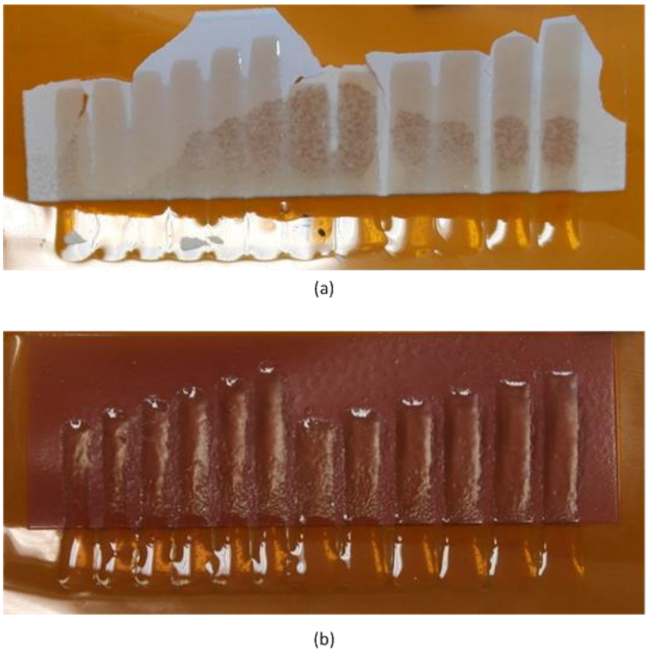

Figure 3-27: (a) SU8 structure bleeds and joint together on TME (b) SU8 printed on PVA.

#### 3.4.3.4 Removal process of sacrificial material 1

Two types of structures were evaluated which are channel and cantilever structures. Using the structural material 1, both of the structures were successfully fabricated as shown in Figure 3-28 and Figure 3-29.

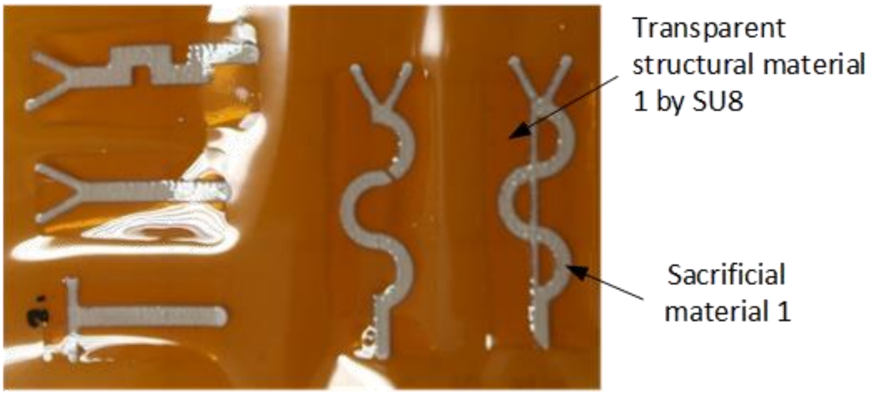

Figure 3-28: Channel structure fabricated using screen-printing.

Figure 3-29: Cantilever structure fabricated using structural material 1.

The removal process for the SU8 printed on the TME sacrificial layer was conducted at 160°C for 30 minutes in box oven as suggested by Wei et al [48, 50]. However, SU8 printed for channel evaluation on a TME sacrificial layer shows cracks on the surface of the SU8 as shown in Figure 3-30(b). This might be due to the high pressure caused by the sublimation of TME during removal and different thermal coefficients between Kapton and SU8.

Figure 3-30: (a) Channel or diaphragm structure before removal of sacrificial material 1 and (b) after removal process.

A cantilever structure with a larger opening area for the removal process was also evaluated. Figure 3-31(a) and Figure 3-31(b) illustrates before and after the removal process respectively. The cantilever structure was successfully released but some TME residue of was found underneath the cantilever.

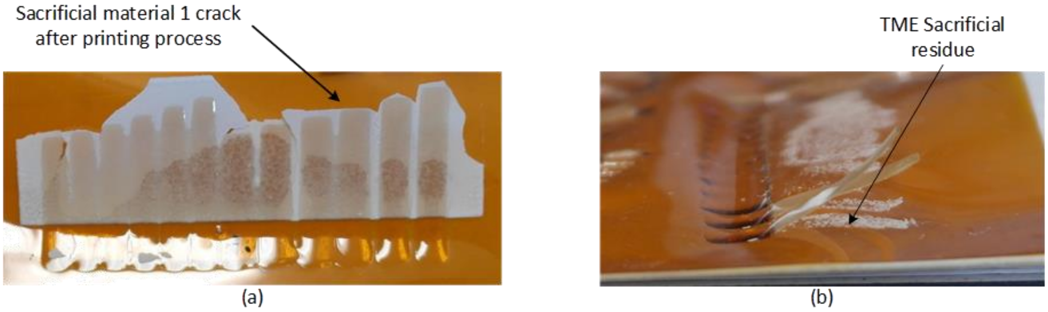

Figure 3-31: Cantilever structure (a) before and (b) after removal process.

#### 3.4.3.5 Removal process of sacrificial material 2

The removal process for PVA was conducted by submerging the sample into water at 90°C. The samples as illustrated in Figure 3-32(a) were fabricated using the parameters described in the previous section. The PVA sacrificial layer was completely removed after 20 minutes and the sample was rinsed with IPA twice and then left for the IPA to evaporate. Figure 3-32(b) shows the SU8 free-standing cantilever structures after the removal process.

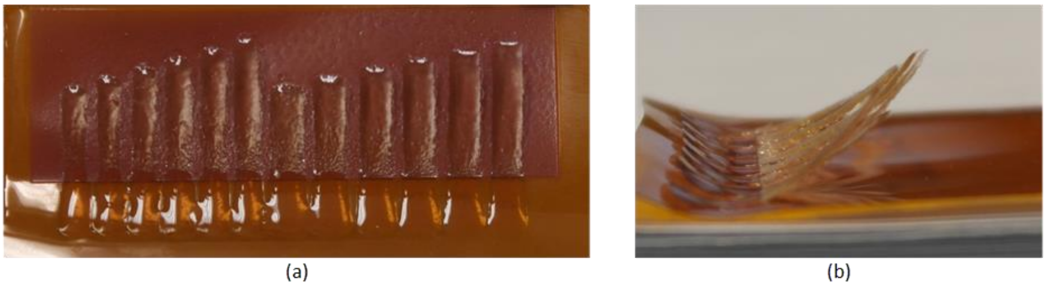
(a)
(b)

Figure 3-32: Cantilever structure printed with sacrificial material 1(a) before and (b) after removal process.

### 3.4.4 Structural material 2 (Minico dielectric)

#### 3.4.4.1 Introduction

Structural material 2 is a Minico dielectric screen-printable thermosetting dielectric produced by Acheson which is usually used as a binder. The curing temperature for this material is compatible with fabrics and the sacrificial layers. The good mechanical properties of Minico are another reason for its selection.

The paste viscosity influences the printing quality. The initial viscosity of the Minico dielectric was measured using a CAP 1000+ with spindle cone 4 and a rotation speed of 10 rpm. The graph below shows the viscosity measurement over time. The measured viscosity was between 90 to 93 Pa.s over the 15 minutes of the measurement. The paste was deposited using a 68-55 mesh polyester screen.

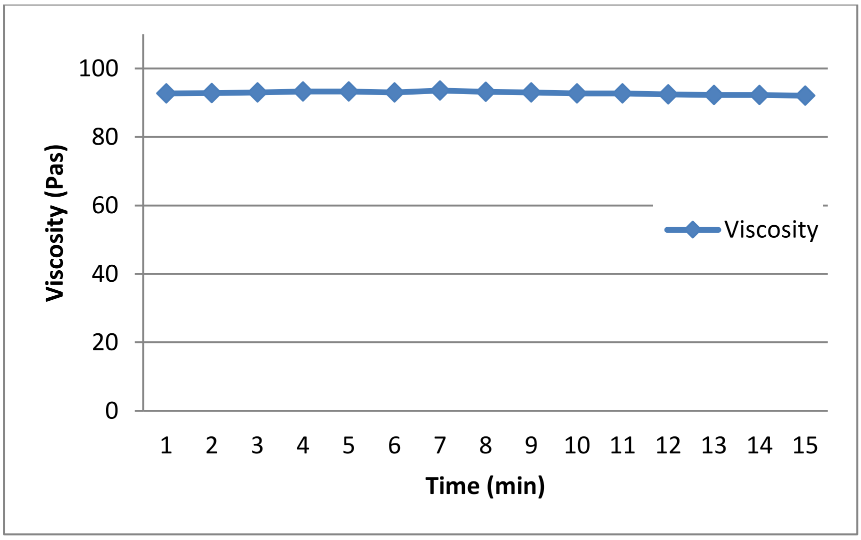

Figure 3-33: Viscosity of Minico dielectric paste over 15 minutes.

Due to the high viscosity of the paste and the fast evaporation of the solvent the paste dried quickly and caused the screen to clog. As a result, the printing pattern was incomplete. It is therefore important to reduce the paste viscosity to improve the printing quality. The viscosity is adjusted using 2-(2-butoxyethoxy)-ethanol solvent as suggested on the Minico dielectric data sheet. Table 3-10 shows the change in viscosity with varying amounts of this solvent.

Table 3-10: Viscosity of Minico dielectric with varying amounts of solvent.

| **Formulation** | **Weight percentage of solvent (g %)** | **Viscosity (Pas)** | **Printing condition** |
|---|---|---|---|
| 1 | 5 | 25.950 | Paste sticky |
| 2 | 10 | 17.100 | Smooth |
| 3 | 15 | 7.725 | Smooth |
| 4 | 20 | 5.025 | Too thin |

The formulation with viscosity between 7 Pa.s and 17 Pa.s gave the best printing quality. However, for formulation 1, the paste was too sticky and caused the substrate to stick to the screen. For formulation 4, the printed paste was too thin which resulted in a very thin printed layer, of around 10μm, which will require more print cycles to achieve the required thickness.

#### 3.4.4.2 Deposition parameter setup

The screen used was the same 12"x12" polyester screen as described in section 3.4.3.2. The best printing parameters, achieved after several tests, for this material are given in Table 3-11. The curing temperature at which this material crosslinks is 160°C for 30 minutes conducted in belt furnace after printing. A lower temperature is used between deposits to dry the deposit to allow the subsequent deposit to be printed.

Table 3-11: Printing parameters for Minico dielectric.

| **Types of screen** | **Polyester screen** |
|---|---|
| Pressure (kg) | 6.0 |
| Gap (mm) | 1 |
| Flood speed (mm/s) | 70 |
| Printing speed (mm/s) | 50 |
| Deposition | 1 |
| Curing condition | Belt dryer 160°C for 30 minutes |

The time taken for the Minico dielectric layer to dry at different drying temperatures was evaluated. The results are shown in Figure 3-34 and Figure 3-35 show a Minico dielectric layer printed on PVA and TME sacrificial layers respectively.

Table 3-12. The most suitable drying temperature for a Minico dielectric deposit on a PVA sacrificial layer was 100°C for 10 minutes. However, a Minico dielectric printed on TME will be dried at 80°C for 30 minutes because the TME sacrificial layer starts to sublime at 87°C. Figure 3-34 and Figure 3-35 show a Minico dielectric layer printed on PVA and TME sacrificial layers respectively.

Table 3-12: Drying temperature for Minico.

| **Drying temperature (°C)** | **Time (min)** |
|---|---|
| 80 | 30 |
| 100 | 10 |
| 120 | 6 |
| 140 | 1 |

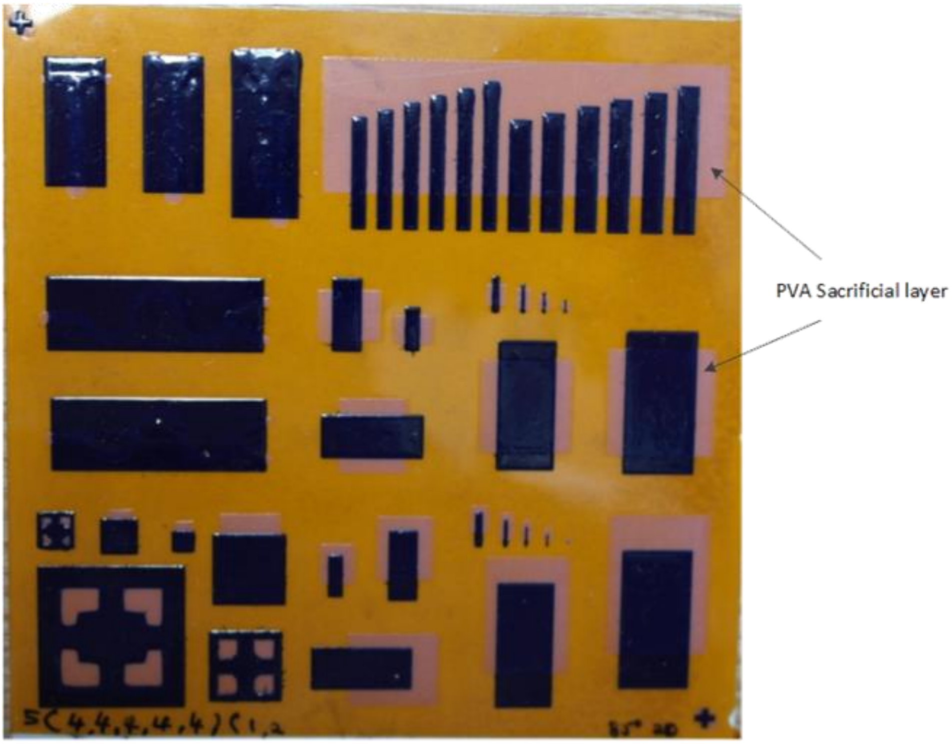

Figure 3-34: Minico dielectric printed on PVA sacrificial layer.

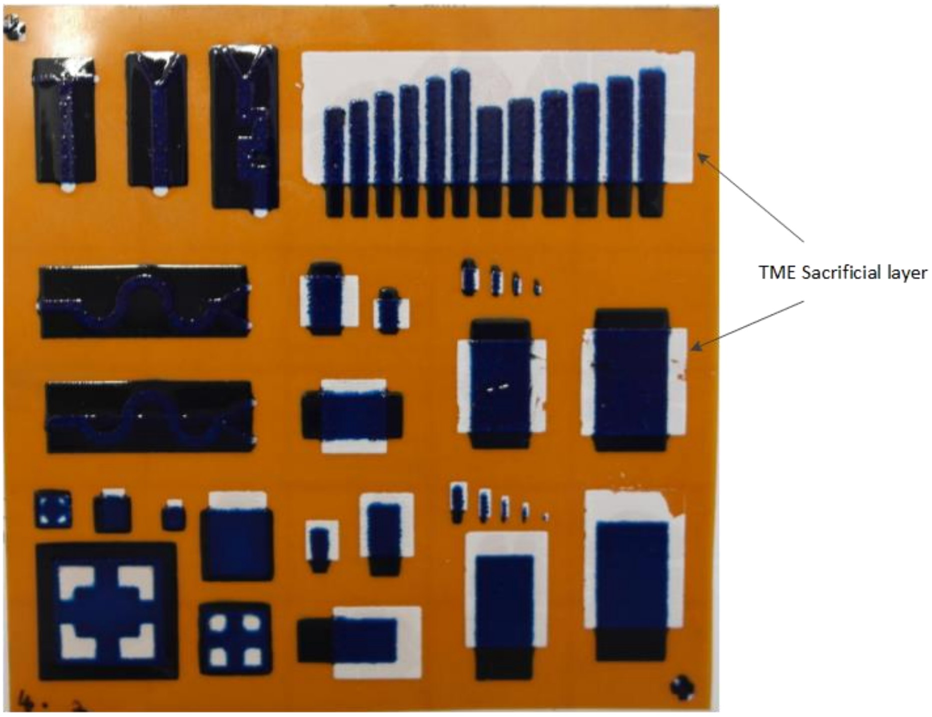

Figure 3-35: Minico dielectric printed on TME sacrificial layer.

#### 3.4.4.3 Experimental results

The curing temperature in the Minico dielectric suggested in the datasheet is 160°C for 30 minutes, so the curing process was carried out at this temperature. Minico dielectric paste was printed using a polyester screen on to Kapton. Three deposits resulted in a layer with a thickness of 125µm. Samples were prepared with a combination of Minico dielectric directly on Kapton and on TME and PVA sacrificial layers. The sample was cured in a box oven with maximum air ventilation. The maximum air ventilation was used to prevent the sample from thermal shock. The resulting structural layer surface had a very rough surface as shown in Figure 3-36. This effect might be due to the solvent in the structural paste evaporating too quickly and causing bubbles on the surface.

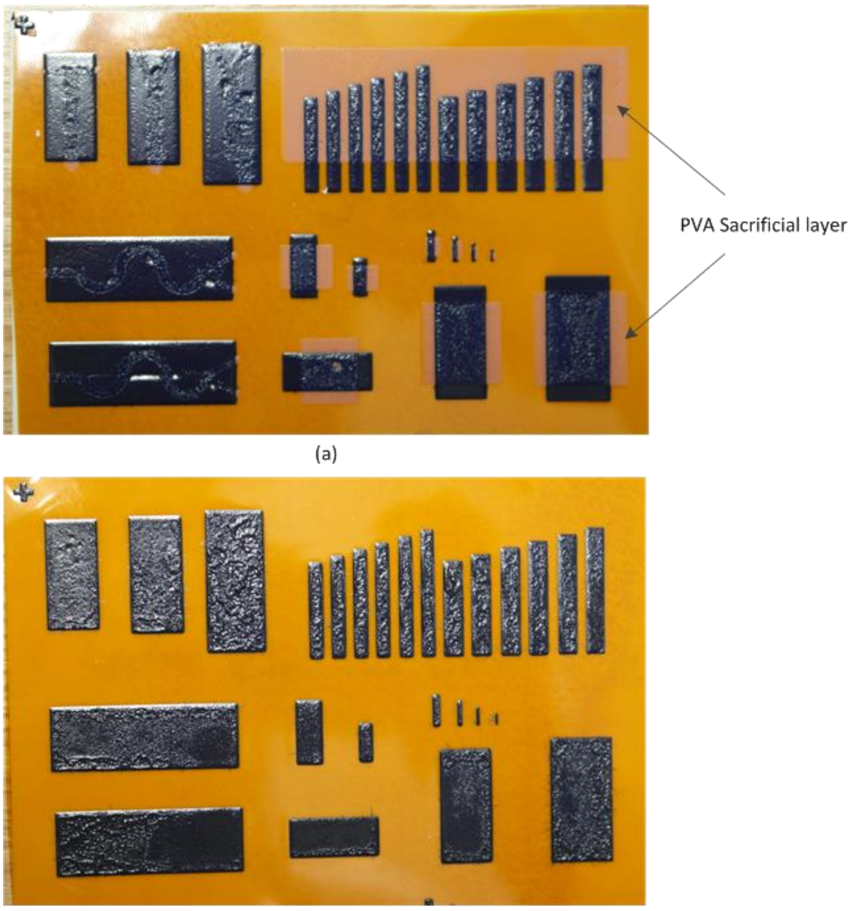

(a)

(b)

Figure 3-36: (a) Dielectric with sacrificial layer (b) without sacrificial layer cured in box oven.

To prevent this from occurring, a curing process in which the temperature was ramped slowly was implemented. This is to allow the solvent to evaporate gradually from the printed layer. Figure 3-37 shows the temperature profile programmed into the belt furnace used in this work.

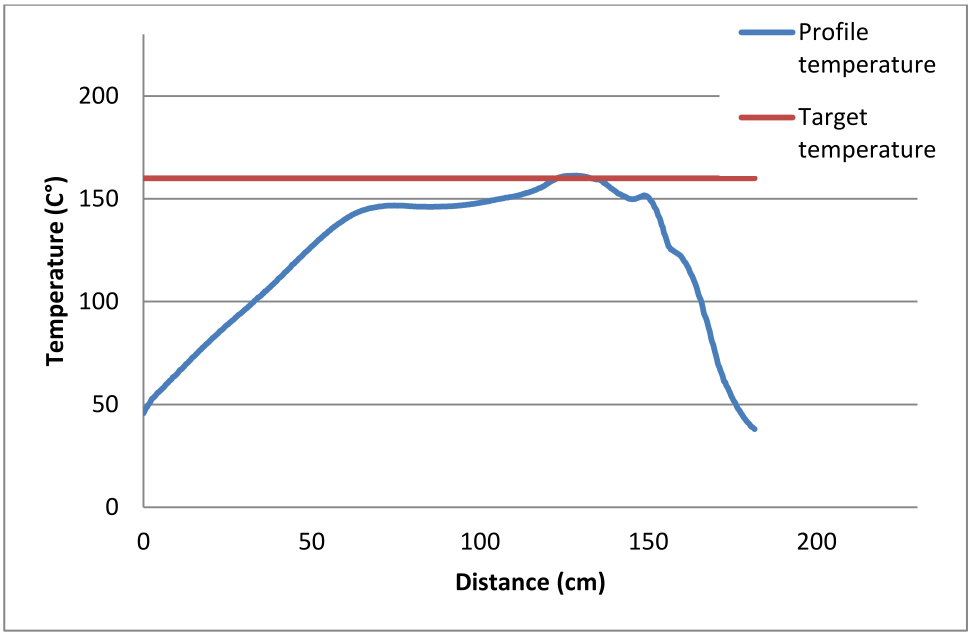

Figure 3-37: Temperature profile for Minico dielectric.

Cured samples using this profile were examined and the samples without a PVA sacrificial layer showed significantly reduced roughness compared to those using the previous curing profile. However, the sample with a printed PVA sacrificial layer has the same rough surface as the dielectric structural layer. This might be due to the air pressure caused by the sublimation of the sacrificial layer during curing process. Figure 3-38 shows the surface of the Minico dielectric dried in the belt dryer.

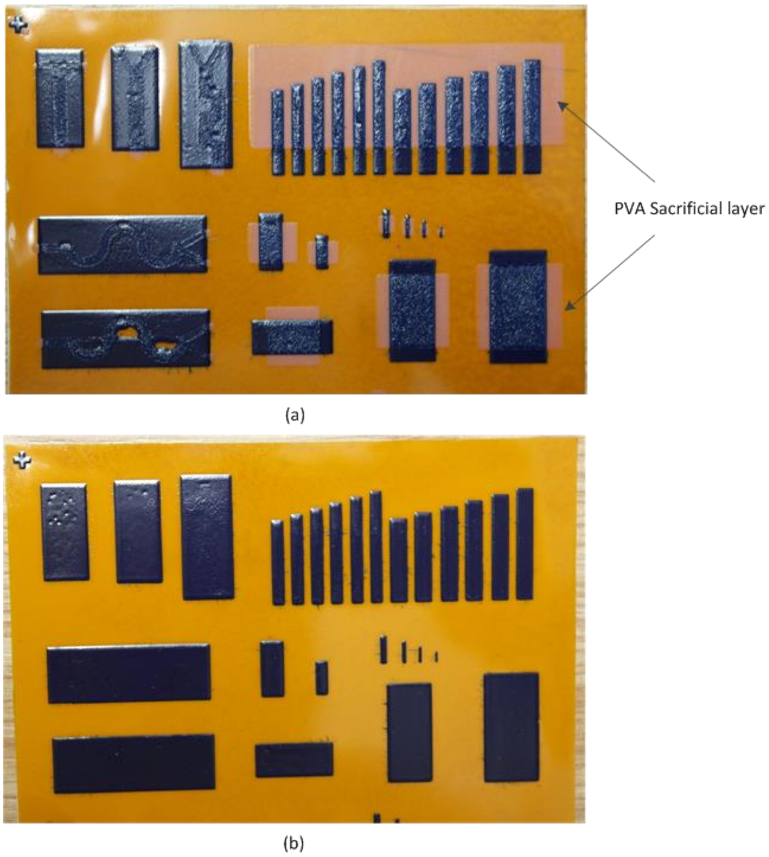

Figure 3-38: (a) Dielectric printed on sacrificial layer and (b) printed directly on Kapton and cured in belt dryer.

Further experimentation was conducted by drying the structural layer at a lower temperature for a longer time to reduce the gas pressure. Printed samples were heated at temperatures from 80 to 160°C in increments of 20°C until cured. Table 3-13 shows the curing time and the observed surface smoothness in this experiment. At temperatures from 80°C to 100°C, the surface condition of the structural layer was smooth and at higher temperatures, from 120°C to 160°C the surface started to become rough and air bubbles formed.

Table 3-13: Surface condition for the curing of Minico dielectric on top a PVA sacrificial layer at different temperatures.

| **Sample** | **80°C** | **100°C** | **120°C** | **140°C** | **160°C** |
|---|---|---|---|---|---|
| Curing time | 4 hours 30 minutes | 3 hours 30 minutes | 2 hours 30 minutes | 1 hour 30 minutes | 30 minutes |
| Surface condition after curing | Smooth surface | Smooth surface | Bubbly surface | Bubbly surface | Bubbly surface |

#### 3.4.4.4 Removal process of sacrificial material 1

The removal process for a TME sacrificial layer with Minico structural layers had issues with the dielectric sticking to the substrate and not being properly released, as shown in Figure 3-39. The removal process was conducted using the same process that crosslinks the dielectric: 160°C for 30 minutes.

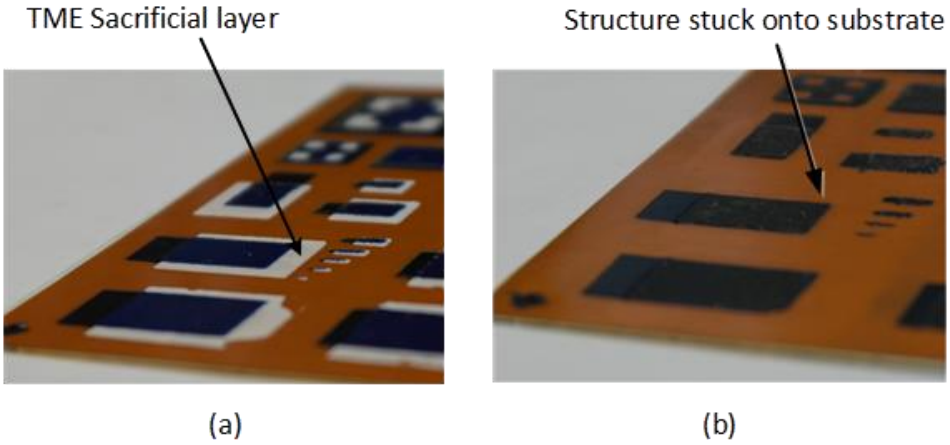

Figure 3-39: Minico dielectric printed on TME sacrificial layer (a) before and (b) after the removal process.

Further experiments were conducted to investigate the cause of the dielectric sticking onto the substrate. It was thought that during the removal process gravity pulled the structure down, after the TME was removed, which resulted in the structural layer sticking to the substrate. Four alumina spacers of thickness 1cm were used to support each edge of the substrate and the substrate was cured upside-down as shown in Figure 3-40. However, the Minico dielectric still stuck to the substrate after the removal process.

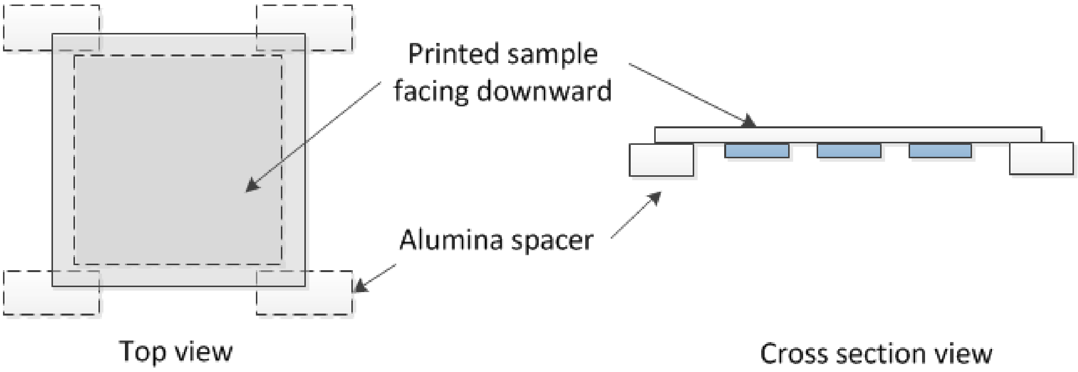

Figure 3-40: Test setup to cure the printed structures upside-down.

#### 3.4.4.5 Removal process of sacrificial material 2

The removal process for PVA sacrificial layers with the Minico dielectric structural layers is submersion in water at 90°C. The sample was submerged in the water as described in section 3.4.3.3. However, the sacrificial layer was not completely removed after one hour and the structural layer adhered to the substrate. This was due to PVA residue remaining underneath the structure as shown in Figure 3-41. Consequently, the sample was submerged for a longer times up to 24 hours. However, after 24 hours, the samples were examined and PVA residue remained beneath the structural layers.

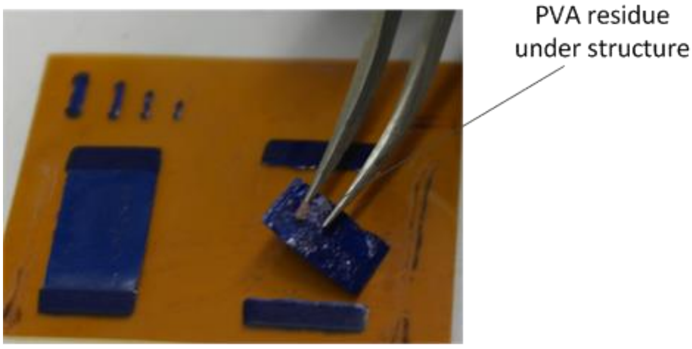

Figure 3-41: PVA residue under the structural layer after one hour in 90°C water.

Next, the flow rate of the hot water was increased to attempt to remove all of the PVA. The sample was placed hanging above a magnetic stirrer as shown in Figure 3-42.

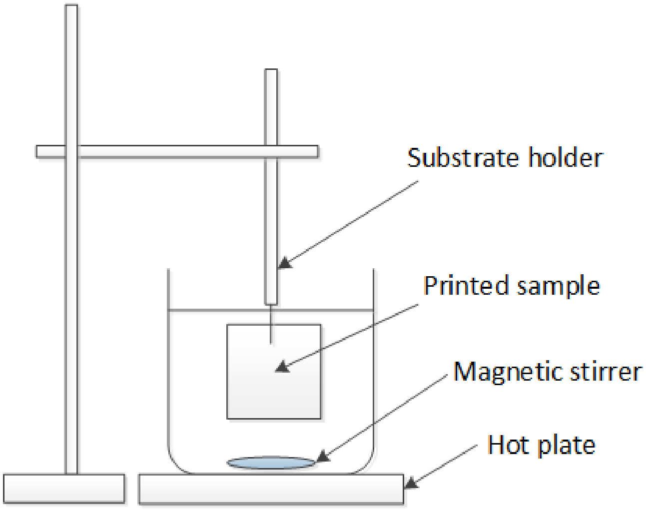

Figure 3-42: Setup to provide increased flow rate in the PVA removal process.

The removal process was carried out with 5 samples using temperatures from 80 to 160°C. The results are presented in Table 3-14. Temperatures between 80°C to 120°C completely removed the sacrificial layer. However, at temperatures equal to or above

140°C, the PVA sacrificial layer was not completely removed which resulted in the structural layer adhering to the substrate.

Table 3-14: PVA removal process at 5 different temperatures.

| **Sample** | **80°C** | **100°C** | **120°C** | **140°C** | **160°C** |
|---|---|---|---|---|---|
| Removal condition | Removed | Removed | Removed | Not removed | Not removed |
| Removal time | 30 minutes | 45 minutes | 45 minutes | N/A | N/A |

## 3.5 Conclusions

Substrate, sacrificial and structural materials were evaluated in this chapter. Three types of substrate were used: alumina, Kapton and 65/35 polyester cotton fabric. A rigid substrate is very important for the printing process; therefore alumina is the easiest material to print on. However, work on Kapton has been initiated so that the structure's behaviour on a flexible substrate can be investigated irrespective of the surface roughness. The fabric properties such as surface roughness and discoloration have also been investigated. The surface roughness of the fabric was greatly reduced by implementing four depositions of interface layer on fabric without sacrificing the fabric flexibility. This has been verified by the SEM image taken for each deposition printed. The Heating tests were also conducted to verify the effect of heating on fabric properties. Before heating, the fabric properties was between 0.35 to 0.40 GPa. The experiment shows that a lower temperature such as 80°C can be used for more than 60 minutes because the Young's modulus is still in the range of the unheated fabric. However, the fabric's Young's Modulus decreases to 0.291 GPa when the temperature reaches 200°C. This indicates the temperature suitable to be used on fabric is below 200°C.

As the aim of the research is to fabricate a free-standing structure, a sacrificial layer is essential. Two types of sacrificial materials have been evaluated which are sacrificial material 1 and sacrificial material 2, of which the main components are TME and PVA-based respectively. Sacrificial material 1 had ragged edges and high roughness especially in position 2 with 11.13 μm. Compared to sacrificial material 1, sacrificial material 2 achieves a well defined pattern following the design on the screen and a smooth surface with the surface roughness at the same position is 0.74 μm. The drying and curing temperature of sacrificial material 2 is compatible with fabric which is between 80°C to 120°C. The sacrificial material 2 was also removed completely when curing between these temperatures ranges. Sacrificial material 1 in other hand, left some residue underneath structural material 1 (SU8) and caused structural material 2 (Minico) to stick on the substrate. Therefore the PVA-based sacrificial layer is selected as the sacrificial layer to be used in this work.

Both Structural material 2 (Minico) and structural material 1 (SU8) show advantages and disadvantages in terms of suitability for printing. Minico has a Young's modulus of 5523 MPa which is 33 times lower than silicon's Young's Modulus but 10 times higher than the materials used by Wei et al [24] . SU8 on the other hand, has a fast curing process (60 seconds) under UV exposure and has a Young's Modulus of 2692 MPa. However, due to air bubbles and smudging of the pattern after printing, SU8 will not be evaluated and used. Furthermore, the pattern definition and mechanical properties of Minico dielectric is better than SU8. Therefore, structural material 2 (Minico) is selected as the structural layer to be used in this work.

# 4. Device 1: screen-printed free-standing cantilever beam

## 4.1 Introduction

In this chapter, the design, fabrication and evaluation of free-standing piezoelectric cantilevers are demonstrated. The design of the device was conducted using ANSYS workbench 15.0 and focused on the placement of piezoelectric layer and estimation of the resonant frequencies and mode vibrations of the device. The simulation results were used to understand and to predict the behaviour of the cantilever device.

In previous chapter, the main materials such as the structural material and sacrificial material was introduced. The focus of the evaluation was to check the material compatibility and removal process. In this chapter, more complex and multilayer structure including piezoelectric layer will be presented. Devices are demonstrated on both Kapton and fabric substrates.

The objective of this work is to fabricate the free-standing piezoelectric cantilever on flexible substrate. A test application using the cantilever as energy harvesting on flexible substrate is undertaken to demonstrate the capability of the printed device.

The evaluation of the free-standing piezoelectric cantilever device has been divided into two sections. The first section presents the testing and evaluation of the performance of a straightforward cantilever device. The second section presents the results of the cantilever with a tungsten proof mass located on the tip of the cantilever. Adding a tungsten mass will improve energy harvesting performance and the effect on resonant frequency, voltage output and cantilever displacement are the main interest.

## 4.2 Free-standing piezoelectric cantilever

The cantilever structure is commonly used in MEMS sensors and can be fabricated using numerous MEMS fabrication techniques. By implementing sacrificial layer in a type of surface micromachining process cantilevers can also be realised by screen-printing techniques. The significance of this kind of structure is the wide range of applications that it can cover, from switches to harvesters and sensors.

The free-standing piezoelectric cantilever on flexible substrate for energy harvesting is a new application of the screen-printing process. The piezoelectric cantilever devices are possible to be implemented on vibrating machinery to harvest the energy. The materials used in this fabrication process are low temperature and proven not to damage the properties of substrate such as fabric.

In this work, the energy harvested from the cantilever device will be the preliminary result for free-standing piezoelectric cantilever on fabric.

### 4.2.1 Piezoelectricity

Piezoelectricity is the ability of certain materials to generate a voltage when a corresponding mechanical stress is applied. The piezoelectric effect is reversible, whereby the shape of the piezoelectric material will also deform proportionally to an externally applied voltage.

The history of piezoelectrics started in 1880, when Jacques and Pierre Curies discovered an unusual characteristic in certain crystalline minerals such as tourmaline and quartz [89]. Each of piezoelectric crystals is built up of elementary cells consisting of electric dipoles. Dipoles near to each other tend to align in a Weiss domains regions. These domains are randomly oriented within the materials, which has no overall polarization as in Figure 4-1(a).

In order to activate the piezoelectric behaviour, the domains must be aligned in a single direction. This alignment can be achieved by the poling process. The process starts by exposing the piezoelectric material to a strong electric field whilst heating it up to the Curie temperature of the material. The domains are forced to change and rotate into the direction of the applied electric field as shown in Figure 4-1(b).

The piezoelectric material is then cooled down to room temperature, while the electric field is still maintained. After poling process, the electric field is removed and most of the domains stay approximately in alignment as shown in Figure 4-1(c). The details regarding the poling process are further discussed in fabrication section 4.4.

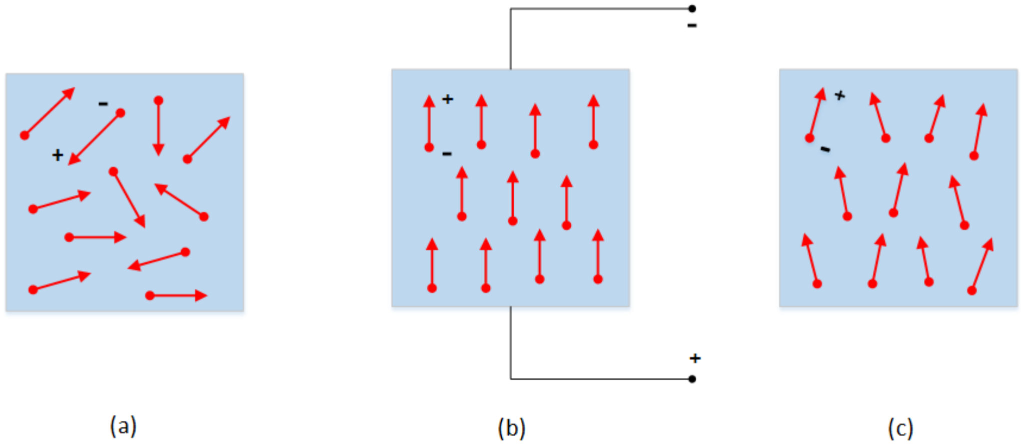

Figure 4-1: (a) random orientation within piezoelectric materials (b) domains rotation change to applied electric field and (c) remanent polarization after poling process.

A piezoelectric cantilever can be designed to operate in either $d_{31}$ or $d_{33}$ modes depending on the electrode arrangement [58]. For example, a bending beam which has top and bottom electrodes sandwiching the piezoelectric layer applies a stress which is orthogonal to the poling direction as shown in Figure 4-2 (a). This configuration is operating in the $d_{31}$ mode. Meanwhile, for the $d_{33}$ mode, the stress applied is the same direction as poling direction as illustrated in Figure 4-2 (b). This requires electrodes to be positioned on only one surface of the piezoelectric material with a gap laterally between each electrode. This forms an interdigital (IDT) electrode pattern typically used to achieve the d33 mode.

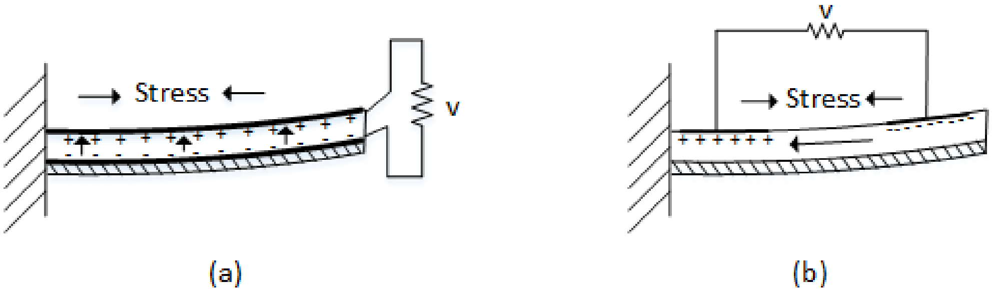

Figure 4-2: Piezoelectric electrode configuration (a) $d_{31}$ and (b) $d_{33}$ mode.

In this work, piezoelectric composites which were produced by University of Southampton were used. The flexibility and low temperature process (i.e. 90°C) allows the piezoelectric composites to be implemented on fabric. The composites consist of PZT ceramic powder and polymer matrix which were mixed and milled to produce a homogenous paste which is suitable to be used in screen-printing process. The materials, formulation and the poling condition were discussed in detail by *Almusallam et. al.*[90] and will not be discussed further.

## 4.3 Design and modelling

Finite element modelling (FEM) has been used to analyse the structure behaviour of the device based upon the structural material presented in chapter 3. A series of finite element simulations was carried out using ANSYS workbench 15.0 to estimate the frequency response, structural stresses and total deformation produced by the structure. Two types of analysis were conducted: modal analysis and harmonic response analysis. The modal analysis was used to predict the natural frequencies and modes of the structure. The harmonic response analysis was used to estimate the stress distribution across the structure.

Three different structures were evaluated in the simulation which are piezoelectric cantilever beam, encastre beam and diaphragm structure. The encastre beam and diaphragm simulations will be discussed in detail in chapters 5 and 6 respectively. The excitation direction of the simulation is normal to the cantilever surface structures. The dimensions and design of the cantilever structure are as illustrated in Figure 4-3.

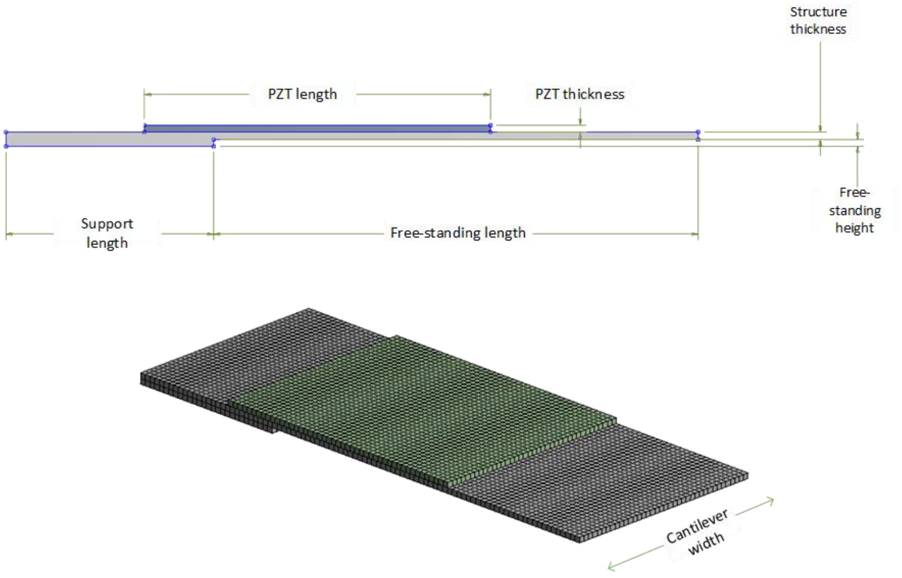

Figure 4-3: Cantilever beam design structure.

The simulation parameters investigated were the length, width and thickness of the cantilever and the force applied as shown in Table 4-1. The key material properties used in the simulations (elastic modulus, Poisson's ratio and the density of the material) are given in Table 4-2.The simulation enables the influence of the dimensions and boundary condition on the resonant frequencies, mode shapes and stress distribution to be investigated.

Table 4-1: Cantilever dimensions.

| **Cantilever dimensions (unit)** | **Values** |
|---|---|
| Length (mm) | 10 |
| Width (mm) | 4 |
| Support length (mm) | 3 |
| Free-standing height* (μm) | 150 |
| Structure thickness* (μm) | 170 |

*Thickness based on SEM image taken

Table 4-2: Material properties used in simulation.

| **Material properties (unit)** | **Values** |
|---|---|
| Minico Young's Modulus (MPa) | 5523 |
| Minico density (kg/m$^3$) | 1300 |
| Minico Poisson ratio (dimensionless) | 0.4 |
| PZT composites Young's modulus (MPa) | 131 |
| PZT composites Poisson ratio (dimensionless) | 0.4 |

An important aspect of the simulations is to investigate the position of maximum stress along the top surface of the cantilever. By establishing this position, a maximum degree of mechanical coupling between piezoelectric element and the cantilever structure can be obtained. This will be a useful guide and estimation for the testing and designing a workable free-standing structure on fabric.

The devices are designed as multilayer composite structures built up from six printed layers of different polymer material. This starts with the interface layer and finishes with the polymer PZT sandwich with a thin layer of top and bottom silver electrodes. Figure 4-4 shows the images of each layer printed on fabric. The average thickness of the PZT is 110 μm, while the average structure thickness is 206 μm.

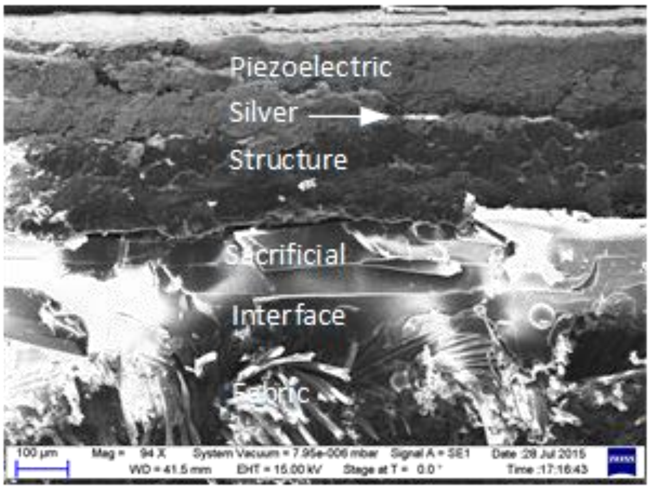

Figure 4-4: Screen-printed cantilever beam under SEM inspection.

### 4.3.1 Modal analysis

At the fundamental out of plane mode, the resonant frequency for the cantilever without added mass was 703.4 Hz. In this mode, the cantilever was moving up and down in Y-direction and the maximum deflection occurs at the tip of the cantilever. The second mode occurs at a resonant frequency of 2574.4 Hz and this is the fundamental torsional mode of the cantilever. Both of the modes can be observed in Figure 4-5(a) and (b) respectively.

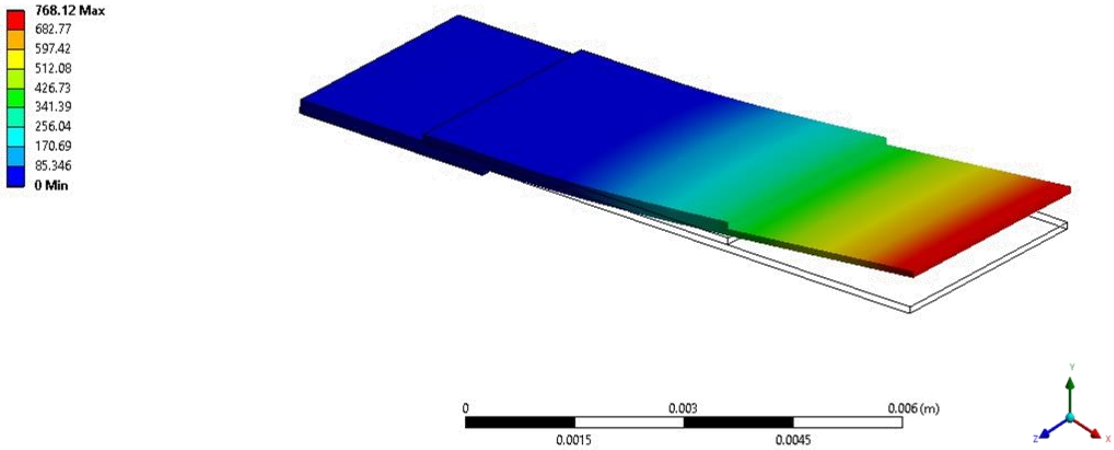

(a)

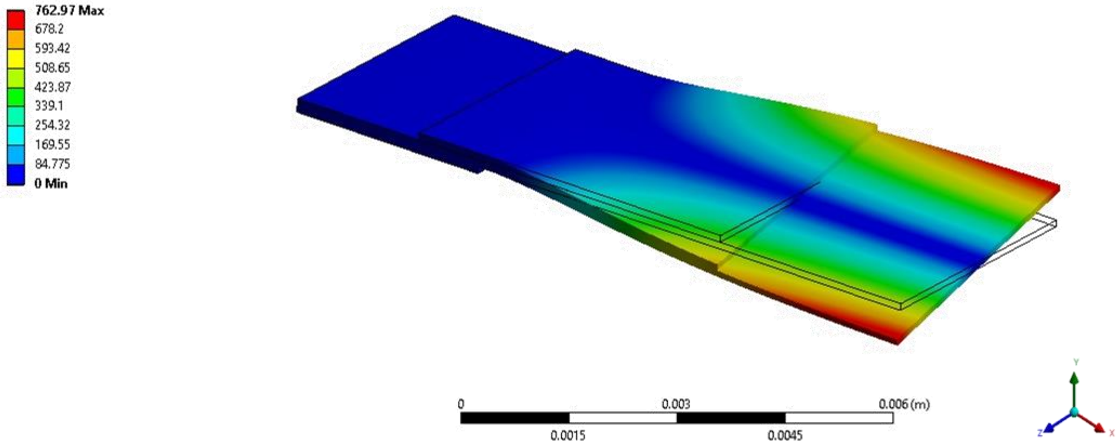

(b)

Figure 4-5: (a) fundamental mode and (b) second mode of cantilever.

The third mode illustrated in Figure 4-6 (c) occurred at 4379.3 Hz and is the first out of plane harmonic of the structure. This has a node (stationary point) along the length of the cantilever device, which result in a wave like movement of the cantilever. The fourth mode occurred at 8574.8 Hz and is the first torsional harmonic as demonstrated in Figure 4-6 (d).

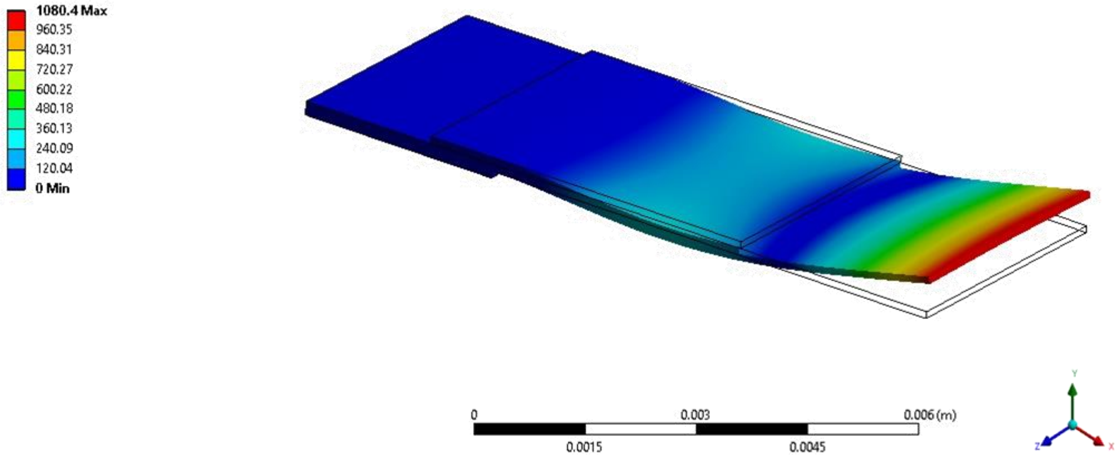

(c)

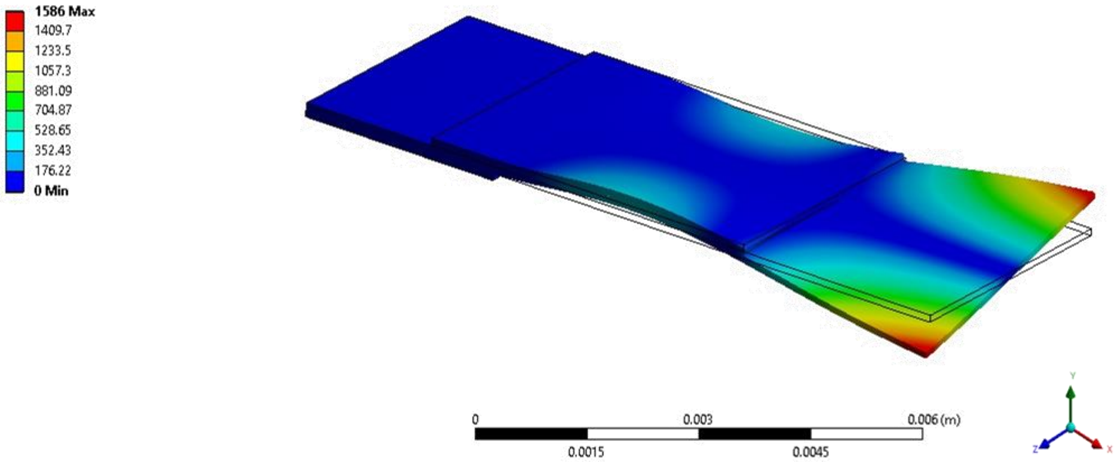

(d)

Figure 4-6: (c) third mode and (d) forth mode of cantilever simulation.

The evaluation continues with a tungsten mass placed on top of the structure. Similar mode shapes but the resonant frequencies have, as expected, decreased up to 203.25 Hz. Furthermore, the magnitude of the stress for the cantilever increases from 1.8778 GPa to 5.583 GPa, 5 times higher compared without tungsten mass. The stress distribution of the cantilever structure are mainly focusing on the anchor or clamping area of the structure as illustrated in Figure 4-7.

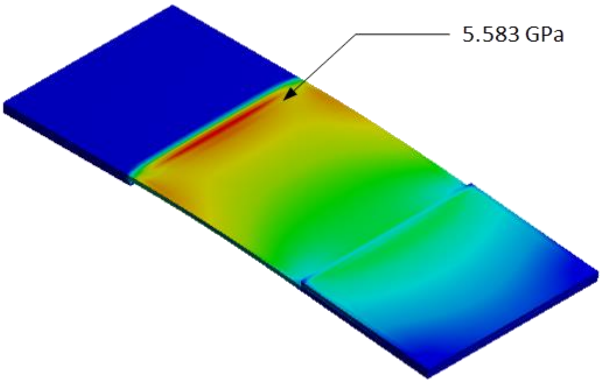

Figure 4-7: Stress distribution on cantilever structure.

The next section will discuss further the fabrication process of the devices on Kapton and also fabric. Based on the simulation results, the polymer PZT are placed in the area where maximum stress is obtained in order to gain the optimum output from the devices. Figure 4-8 and Figure 4-9 show the illustration and actual printed device of polymer PZT placement respectively. Both of the figures showed the polymer PZT layer overlapping the clamping area which had maximum stress to allow maximum coupling between structure and piezoelectric elements.

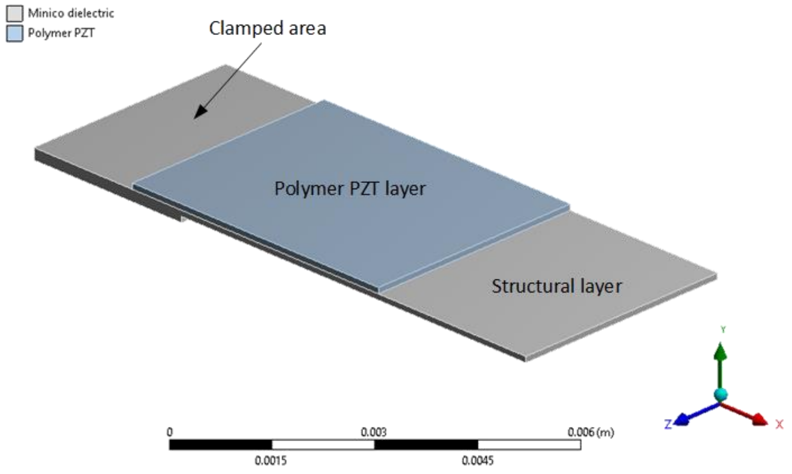

Figure 4-8: Illustration of polymer PZT placement on cantilever structure.

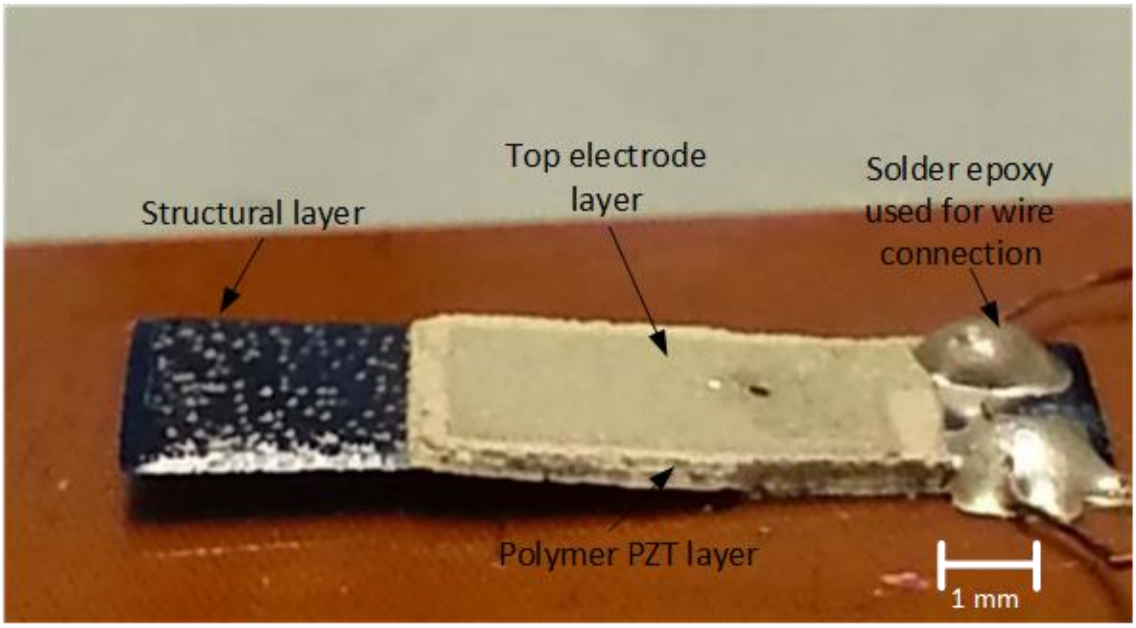

Figure 4-9: Polymer PZT placement of actual printed device.

## 4.4 Fabrication

Figure 4-10 (a) and (b) show the piezoelectric cantilever device fabrication flow on two different flexible substrates; textile and Kapton. The cantilever device fabricated on textile needs an extra interface layer compared to fabrication on Kapton. The interface layer is essential to reduce the surface roughness and to prevent penetration of paste into the fabric.

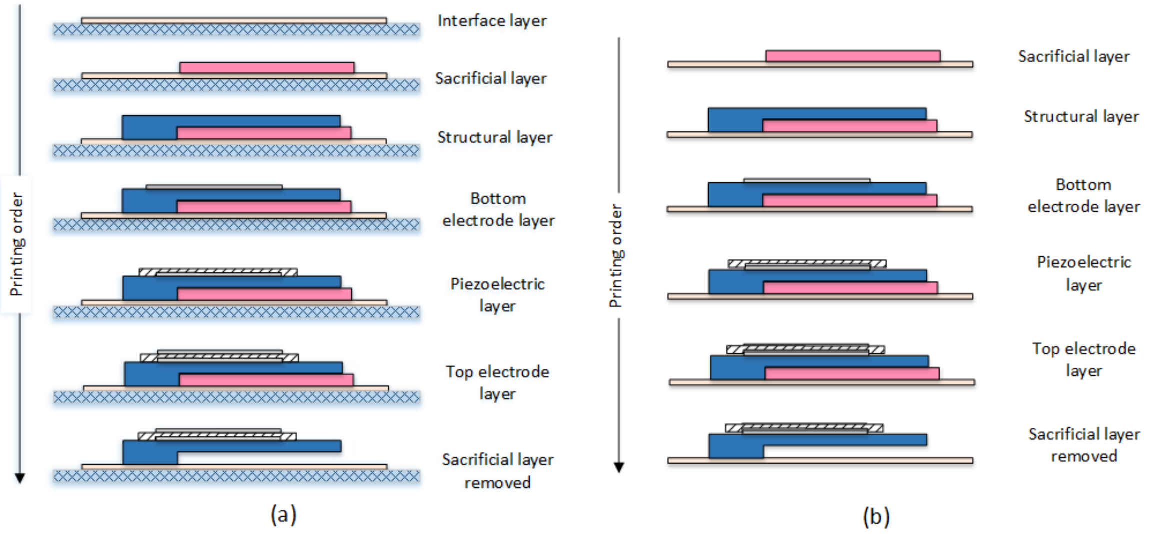

Figure 4-10: Lateral view of piezoelectric cantilever fabrication flow on (a) fabric and (b) Kapton.

The fabrication process starts with printing the interface layer on the textile and is followed by printing the sacrificial layer. Then, a structural layer was printed to form the main body of the device. The process continues with printing the piezoelectric layer sandwiched by bottom and top electrodes. Finally, the process ends with the removal of the sacrificial layer to produce a free-standing cantilever beam as illustrated in SEM image in Figure 4-11. The fabrication sequence on polyester cotton textile and polyimide Kapton is as shown in Figure 4-12 and Figure 4-13 respectively.

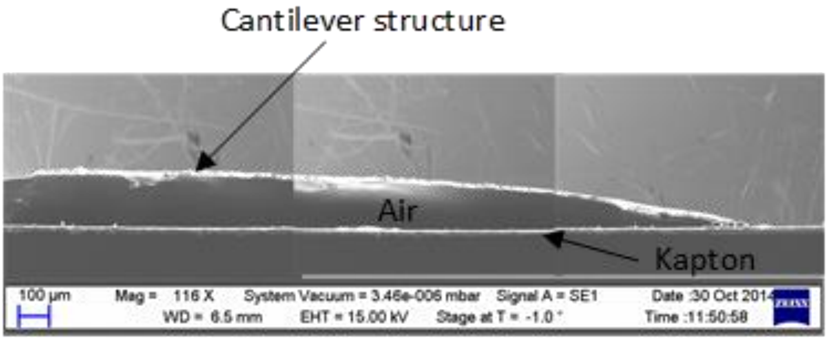

Figure 4-11: SEM image of cantilever after removal.

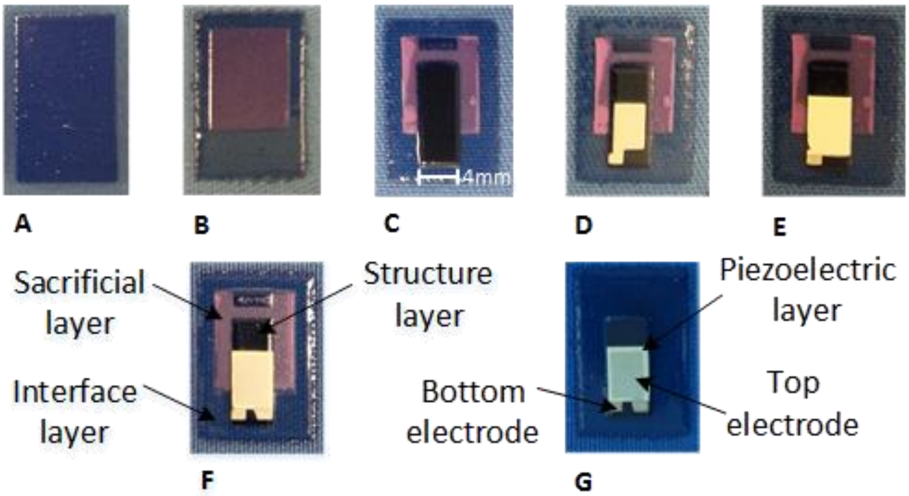

Figure 4-12 : Printing sequence for cantilever on polyester cotton textile.

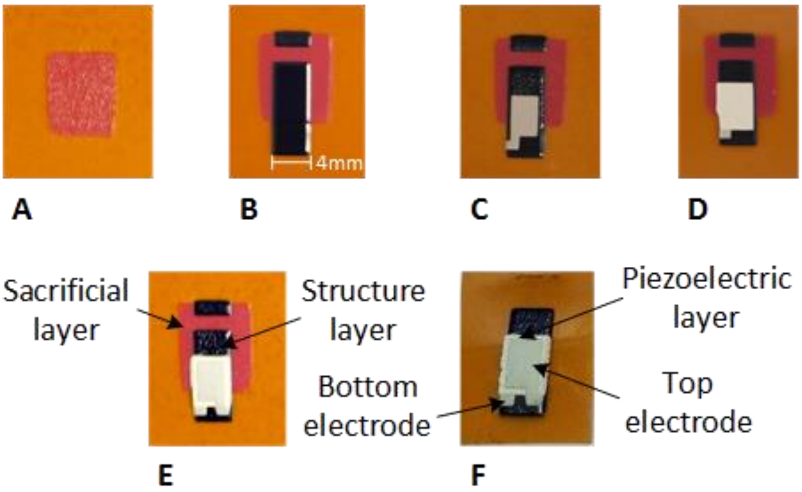

Figure 4-13: Top view of cantilever structure on polyimide Kapton substrate.

Each printed layer required a separate screen and in total 6 to 7 screens were needed including the interface layer. One advantage of using screen-printing techniques is the ability to simultaneously fabricate a variety of dimensions and geometries on one substrate as illustrated in Figure 4-14.

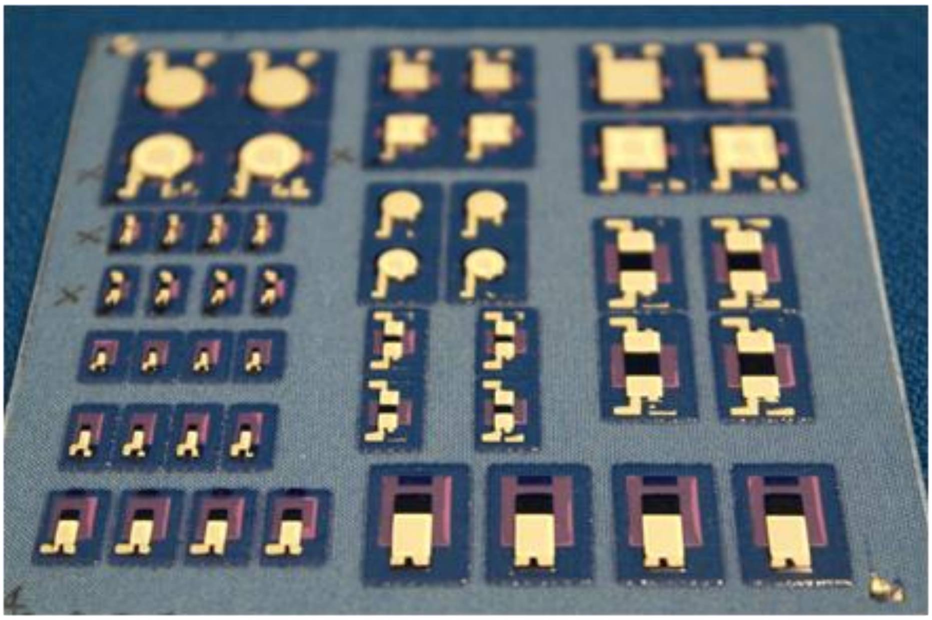

Figure 4-14: Device fabricated on 101x101 mm substrate with different structures and dimensions.

The cantilever devices were fabricated with 4 different dimensions. This was done in order to explore the minimum printable size with each paste and also the capability of the fabrication technique. The dimensions of the electrodes are always smaller than the piezoelectric layer to prevent short circuit between top and bottom electrodes. Table 4-3 shows the dimension of the printed cantilevers on a 101x101 mm substrate. However, in this work only cantilever size of 11.0x4.0 mm were tested due to the high yield produced for each productions.

Table 4-3: Fabricated cantilever dimensions.

| **Design** | **1** | **2** | **3** | **4** |
|---|---|---|---|---|
| Cantilever (mm) L x W | 11.0 x 4.0 | 6.0x2.0 | 5.0x1.0 | 3.0x0.5 |
| Top and Bottom electrode (mm) L x W* | 4.5x3.0 | 2.0x1.0 | 2.0x0.5 | 1.5x0.3 |
| Piezoelectric (mm) L x W | 5.5x4.0 | 3.0x2.0 | 2.5x1.0 | 1.7x0.5 |

*not including connection pad

The sacrificial layer was removed either using method described in chapter 3 or using ultrasonic bath. The samples were submerged in the water as in Figure 4-15 and the sacrificial layer was removed completely after 5 minutes.

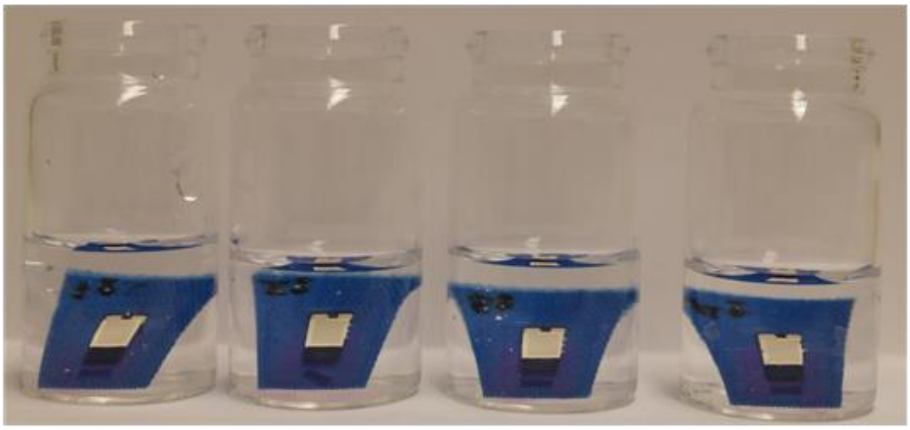

Figure 4-15 : Cantilever sample submerged in water before removal.

The samples were than dried at 100ºC in a box oven to evaporate the water. The connection pads on the samples were than connected using silver conductive epoxy from CircuitWork®. The samples were than left for 24 hours for the conductive epoxy to harden before the PZT could be polarized.

After polarization process, some of the cantilever was attached with tungsten mass for evaluation in section 4.5.2.2. The tungsten mass was attached with fast drying glue on the tip of cantilever without overlapping the piezoelectric layers. The tungsten mass used was 4.9 mm long and 3.0 mm wide with a thickness of 570 μm.

### 4.4.1 Poling process

Polarisation is the final and essential fabrication step to active the cantilever piezoelectric layer. The top and bottom electrode of the cantilever were connected electrically to a 300V potential difference, which is equivalent to an electric field of 3.7MV/m. After a period of time to allow temperature to stabilise at 90ºC, the electric field was applied and kept on for 6 minutes.

The sample was allowed to cool down at room temperature for approximate of 20 to 30 minutes after which the electric field was removed. The influence of the poling parameters such as poling temperature, poling electric filed and poling duration on polymer piezoelectric has been evaluated further by *Almusallam et al* [29]. The poling setup is as illustrated in Figure 4-16.

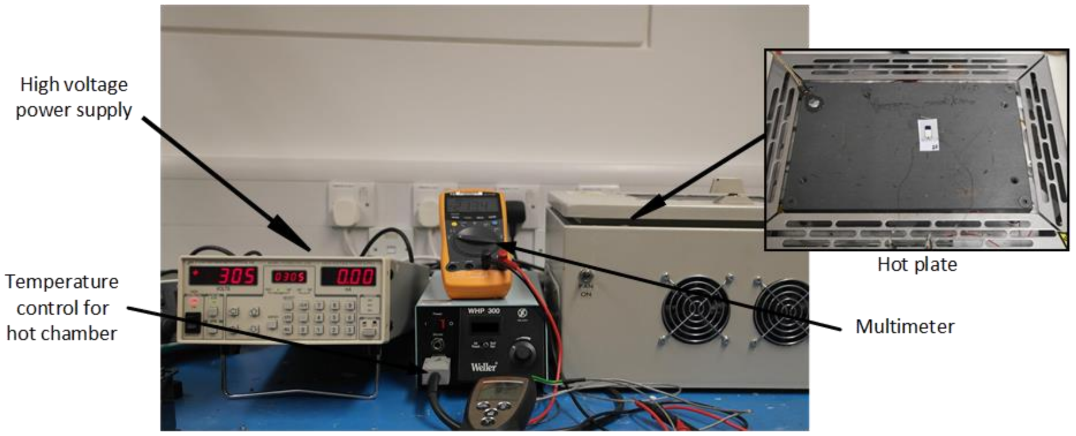

Figure 4-16: Cantilever sample on hot plate while poling process.

The $d_{33}$ value was measured at five different locations on the device with eight measurements at each location using a PM35 piezometer. A force of 0.25 N was applied to the sample which was mounted between two curved probe tips, one mounted on a load cell, the other was driven by shaker oscillating at 110 Hz as shown in Figure 4-17. The charge produced by the sample was measured using a charge amplifier which was directly related to the $d_{33}$ values. The results from 4 cantilevers are illustrated in Figure 4-18 and had $d_{33}$ values of between 29 pC/N and 22 pC/N.

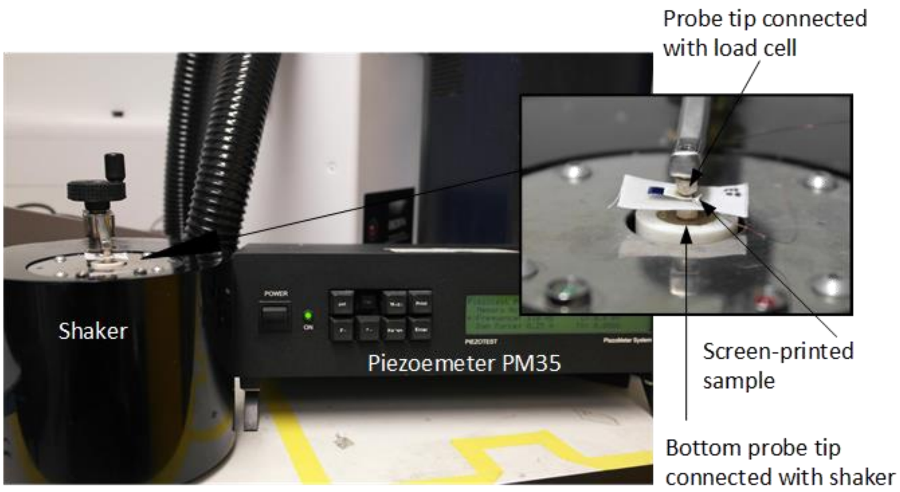

Figure 4-17: Piezometer used to measure $d_{33}$ values.

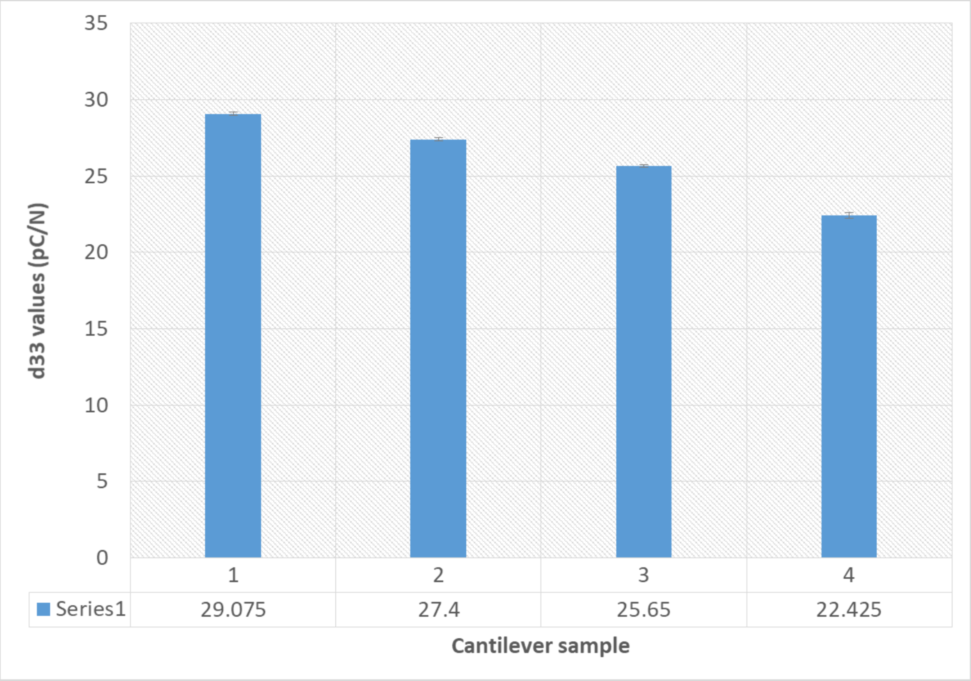

Figure 4-18: Average value of four samples $d_{33}$ after polarisation process.

This measurement confirmed that the printing of the piezoelectric layer was successful. The samples showed no short circuit between the printed electrodes and no deformation was observed on the textile. Therefore, the materials and process used are compatible with textiles.

## 4.5 Experimental Evaluation

The composite free-standing cantilever samples with and without mass on both Kapton and textile were tested and the experimental results compared with the model described in section 4.3. The experimental results obtained for each device are the actual resonant frequency and the voltage output from the piezoelectric element. The results were then used to calculate the energy which can be harvested from the printed cantilever device.

### 4.5.1 Setup

The samples were characterised on a shaker table operated by a sinusoidal driving signal over a range of different frequencies close to the predicted resonant frequency of the cantilever beam as simulated. The acceleration level was maintained at constant level by using a feedback system. The accelerometer in the shaker measures the actual value of frequency and acceleration level applied and this is feedback into the Labview based control system. A revised driving signal is then generated and applied the shaker to ensure the desire acceleration level is achieved at a given frequency. Hence, confirming the resonant frequency of the sample.

A laser displacement meter by KEYENCE (model LC-2450) was used to measure the cantilever displacement. The sample was mounted on the shaker while the laser was focusing on the tip of the sample. The output voltage and cantilever displacement results was taken simultaneously. Figure 4-19 shows a free-standing cantilever on Kapton mounted on the shaker rig with the laser focused on the tip of cantilever structure.

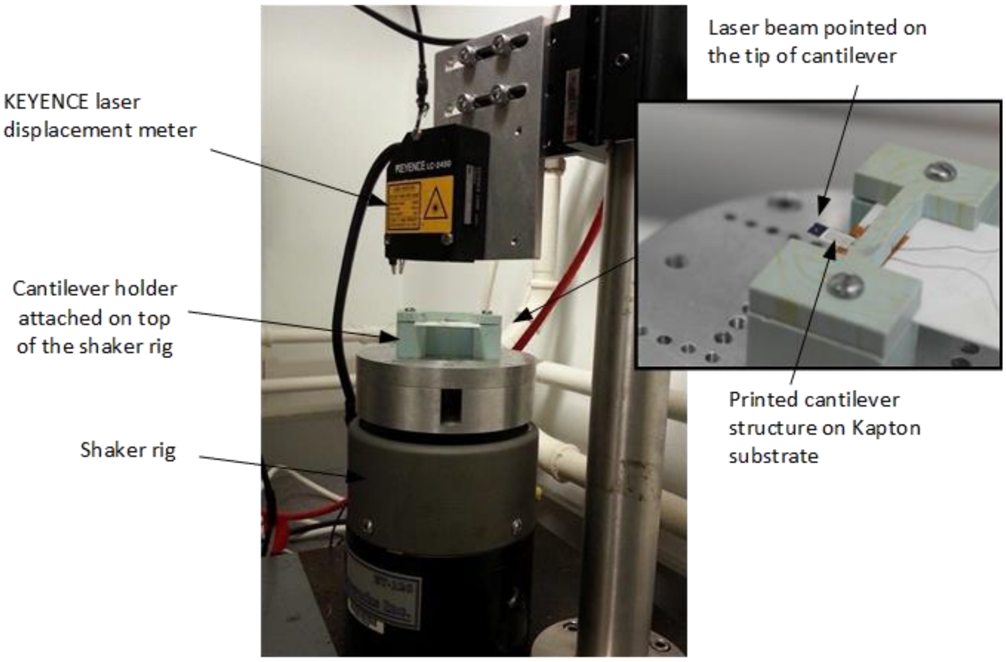

Figure 4-19: Cantilever device on electromechanical shaker.

### 4.5.2 Results

#### 4.5.2.1 Excitation without proof mass

The voltage output of the piezoelectric and the cantilever displacement were measured over frequency range of 1150 Hz to 1744 Hz with increments of 2 Hz at a series of acceleration level from 2.94 m/s$^2$ up to 12.75 m/s$^2$. Figure 4-20 and Figure 4-21 show the measurements of the voltage output and the displacement of the cantilever on Kapton versus frequency.

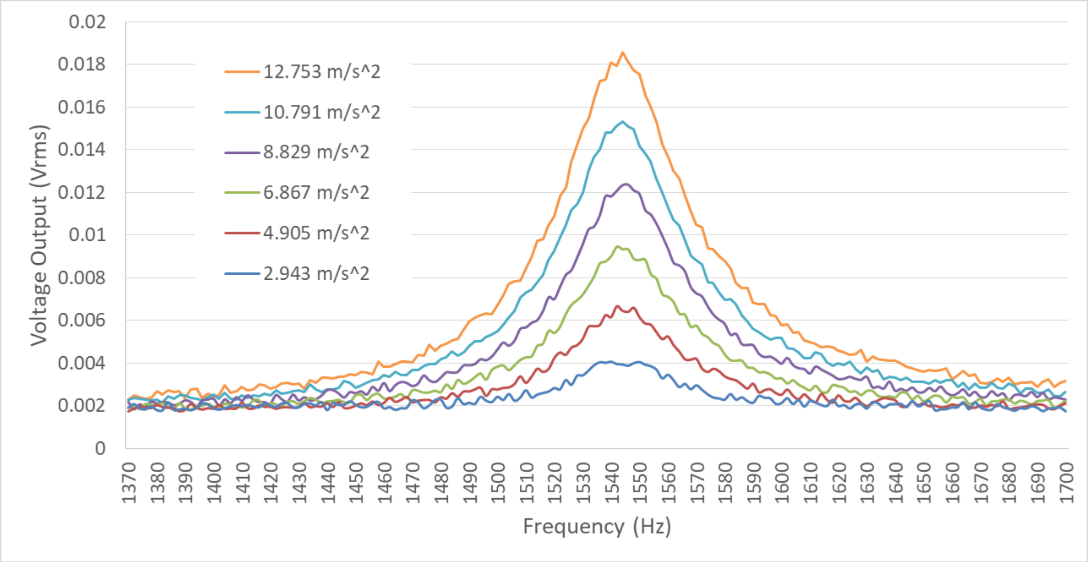

Figure 4-20: Experimental result for cantilever on Kapton without tungsten mass.

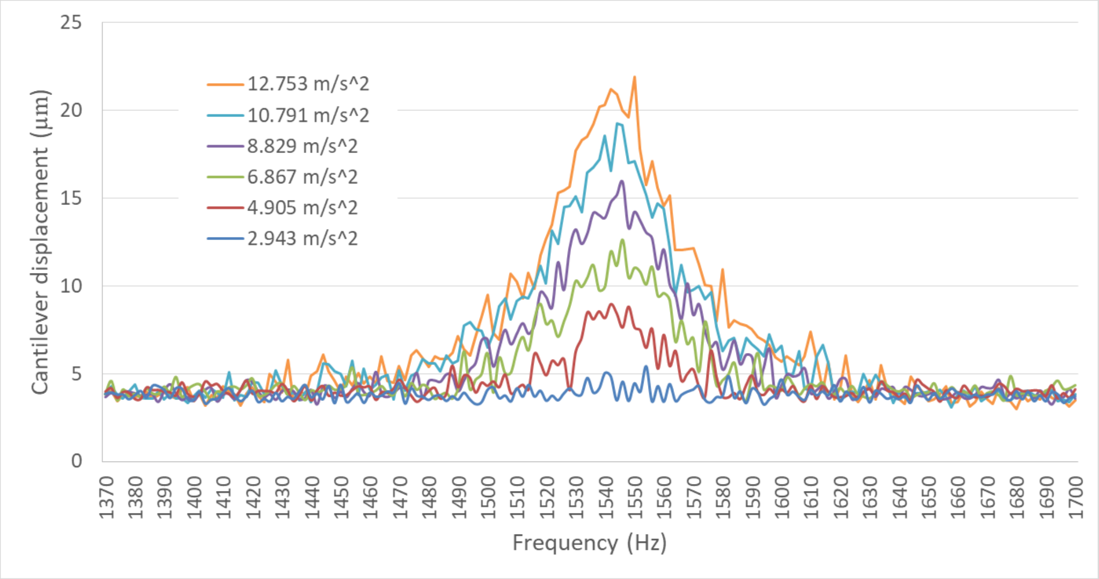

Figure 4-21: Cantilever displacement measurements taken simultaneously.

The fundamental out of plane resonant frequency of the cantilever was found to be 1544 Hz. The maximum output voltage was 18.6 mV and the maximum tip displacement was 21.92 µm when the cantilever was excited at 12.75 m/s$^2$. As expected, the voltage output and the cantilever tip displacement shows a good correlation as in Figure 4-22, both the voltage and displacement increases as the acceleration increase.

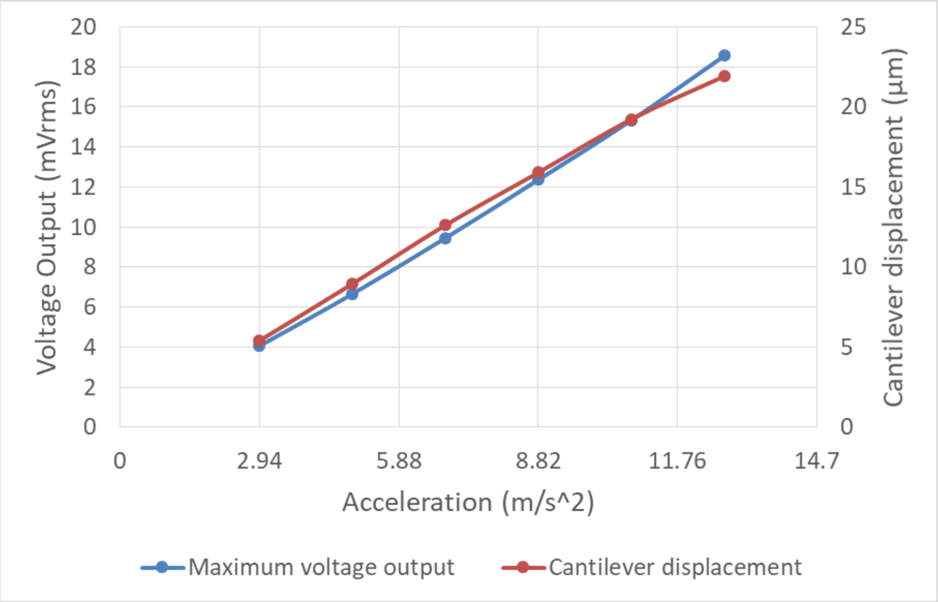

Figure 4-22: Experimental result of cantilever displacement and voltage output subject to acceleration.

The same experiment was repeated on free-standing cantilever on fabric but due to very low voltage output from the piezoelectric cantilever only the cantilever displacement results was visible. The resonant frequency for free-standing cantilever fabricated on fabric occurred between 1176 to 1198 Hz. Figure 4-23 shows the maximum cantilever tip displacement achieved was 2.03 µm when excited at 14.72 m/s$^2$. The cantilever displacement increases gradually with acceleration as in Figure 4-24.

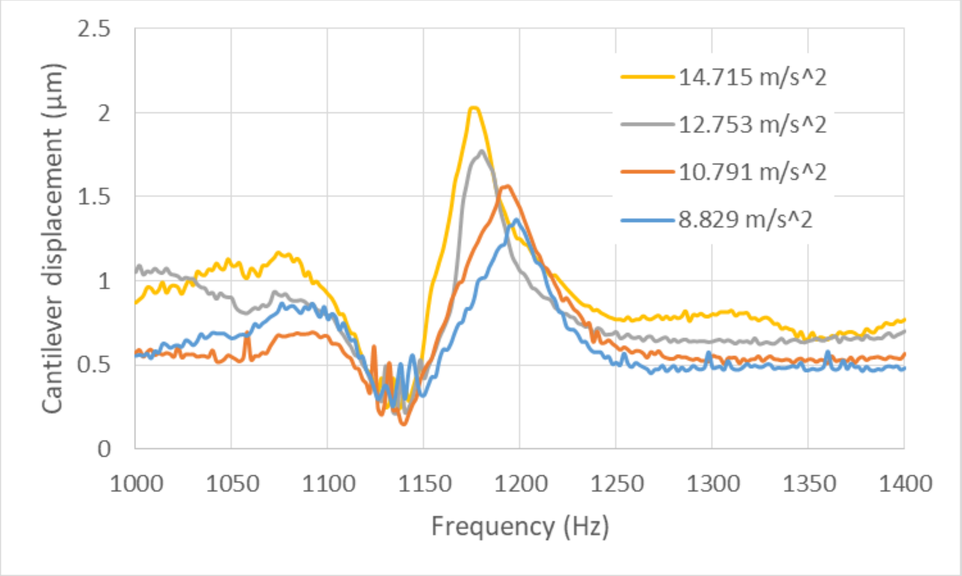

Figure 4-23: Experimental results of cantilever displacement on textile.

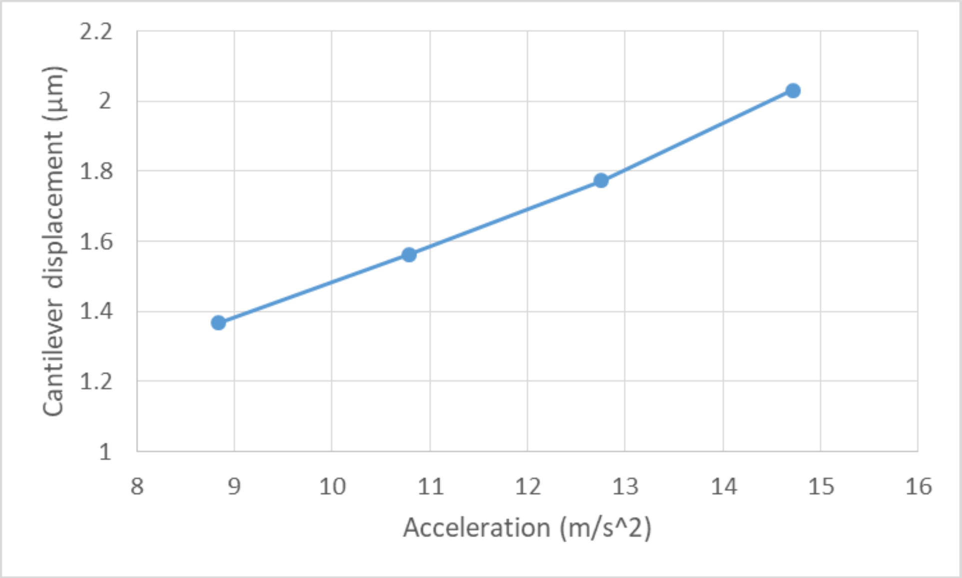

Figure 4-24: Cantilever displacement increase gradually with accelerations.

Both the resonant frequency on Kapton and fabric are almost 2 times higher than the simulation result. It is essential to mention, the evaluation of the properties of each composite materials is not perfect and the actual Young's modulus may be different to that used in the simulation. Also, the thickness of the printed layer is difficult to control and actual layer thicknesses will be different to those modelled.

#### 4.5.2.2 Excitation with proof mass

Attaching additional proof mass to the cantilever beam will reduce the resonant frequency and increase the stress in the piezoelectric layer and therefore maximise the voltage output of the device. A tungsten mass of 0.13g with density of 16249 kg/m$^3$ was attached on the tip of cantilever as shown in Figure 4-25 and placed on electromechanical shaker as explained previously.

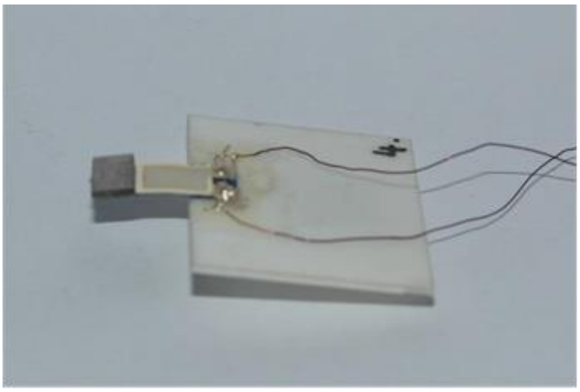

Figure 4-25: Cantilever attached with 0.13g tungsten mass.

Figure 4-26 and Figure 4-27 shows the resonant frequency and cantilever displacement respectively after tungsten mass was attached. The resonant frequency is reduced by 86% from 1544 Hz to 207 Hz while, the cantilever displacement increases from 5μm (without mass) to 64 μm when the cantilever was excited at 2.943 m/s$^2$. The voltage output increases 10 times higher compare to the cantilever without proof mass at the same acceleration. Therefore, as expected, adding the tungsten mass reduces the resonant frequency and increases the voltage output of the piezoelectric layer.

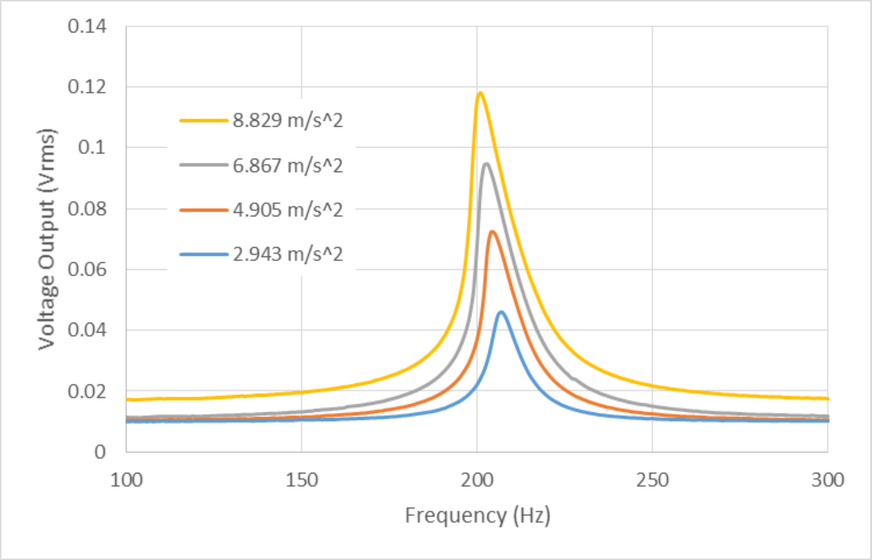

Figure 4-26: Experimental result of free-standing cantilever on Kapton with 0.13g tungsten mass.

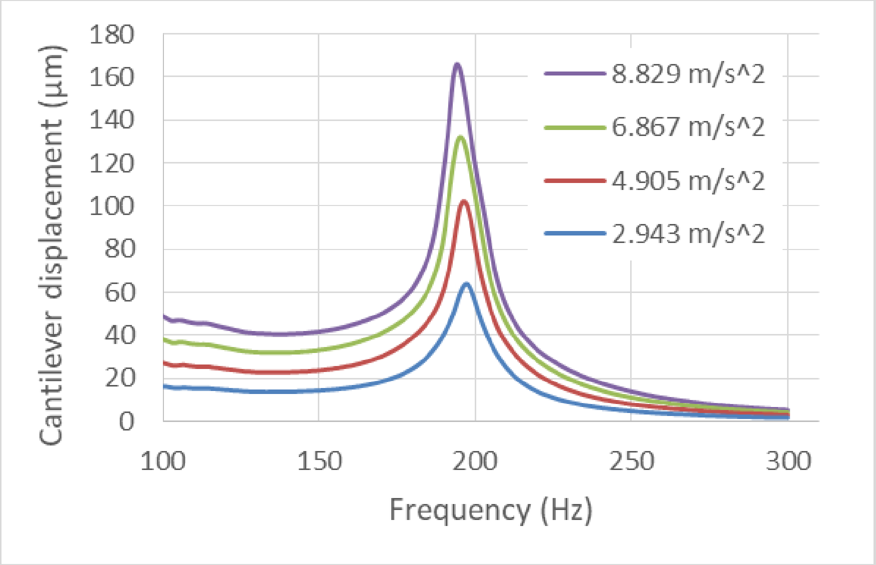

Figure 4-27: Cantilever displacement taken simultaneously from cantilever with 0.13g tungsten mass.

The experimental results show that the cantilever device exhibit a soft non-linear behaviour when the device was attached with proof-mass. This is shown by the natural frequency shifted to lower frequency as the acceleration increased as shown in Figure 4-28. This behaviour is attributed to the increased of elastic compliance of PZT due to nonlinear effects under large stress [91].

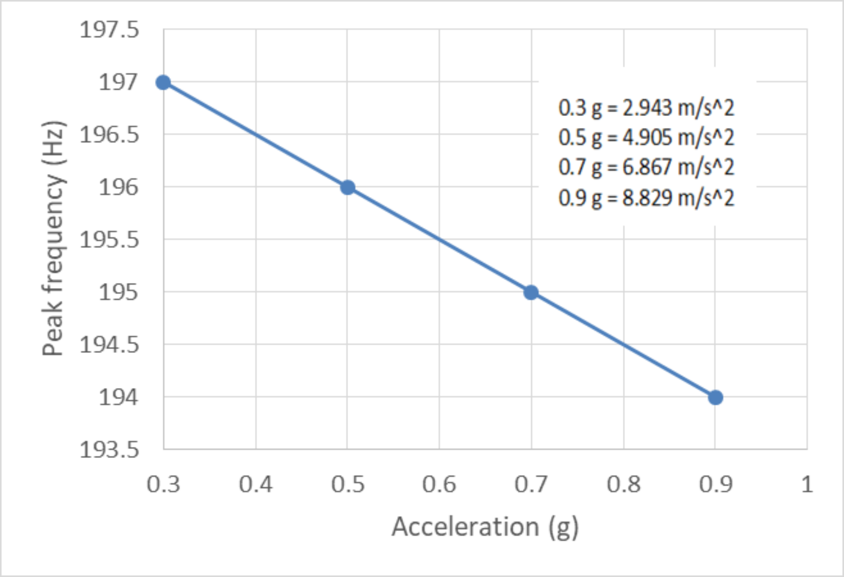

Figure 4-28: Soft non-linear behaviour exhibit by screen-printed free-standing cantilever device where the frequency reduces with increasing amplitude.

The mechanical quality factor, Q, of the device is dependent upon the sharpness and magnitude of the resonance of the cantilever. The Q-factor of the cantilever can be calculated from the resonant response curve by $Q = f_0/\Delta f$, where $f_0$ is the resonance frequency and $\Delta f$ is the bandwidth at half of its peak power value.

The Q-factor calculated from the cantilever displacement is 42.94 for cantilever without mass and 12.93 for cantilever with tungsten mass shows 69.9% decreases in Q-factor. This decreases indicates increasing mechanical losses that can be attributed to air damping effects and internal friction.

Further experiments were conducted to investigate the electrical output power from the cantilever device. The top and bottom electrode of the cantilever device was connected to a programmable load resistance that is varied automatically and the output voltage and power calculated at each resistance. A series of different experiments were carried out to evaluate the output power as a function of electrical load resistance, input acceleration level and proof mass.

By carefully selecting the resistive loads, the electrical damping can be adjusted to equal to the mechanical damping. Once the optimal resistance load was obtained, the maximum power output from the device can be produced. Figure 4-29 shows the experimental result produced from the free-standing piezoelectric cantilever device when excited from 100 Hz up to 300 Hz with increment of 1 Hz. The maximum power output was obtained at resonant frequency which was varied between 201 to 207 Hz with increasing acceleration. From the results, the maximum power output achieved was 27.9 nW at a frequency of 201 Hz with a load resistance of 500 k**Ω**.

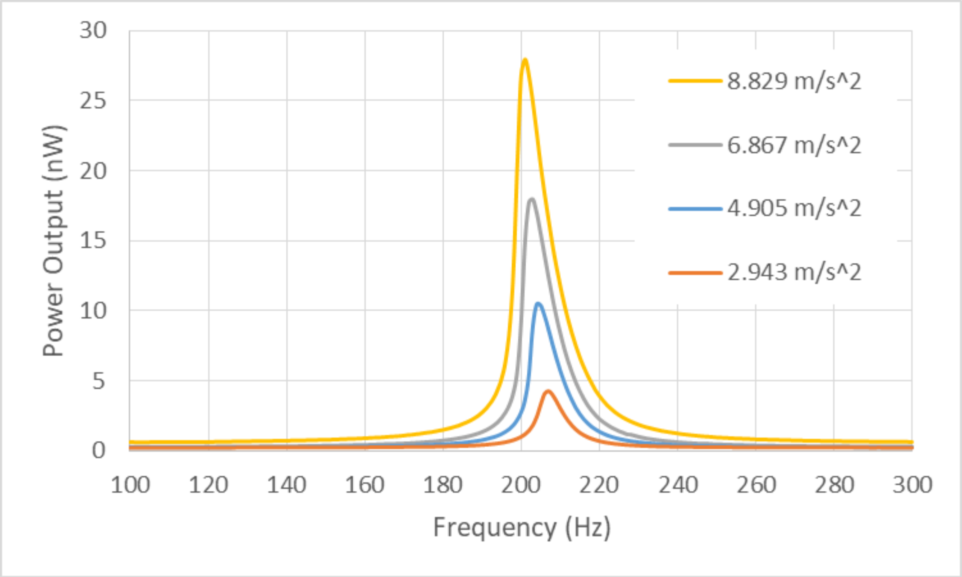

Figure 4-29: Power output excited at resonant frequency with 500 k**Ω** load resistance.

The relationship between the different acceleration levels and the load resistances were also evaluated. Four different acceleration levels starting from 2.943 m/s$^2$ up to 8.829 m/s$^2$ with varies load resistances from 1 k**Ω** up to 50 M**Ω** were investigated. The results in Figure 4-30 and Figure 4-31 shows that the power output of the device increases significantly as the acceleration increases. This result agrees well with the relationship of power verses the square of acceleration. By varying the load resistances at certain acceleration, the optimum power output was obtained and it was found to be at 500 k**Ω**. However, the power output decreased and became negligible from 1 M**Ω** and 5 M**Ω** respectively.

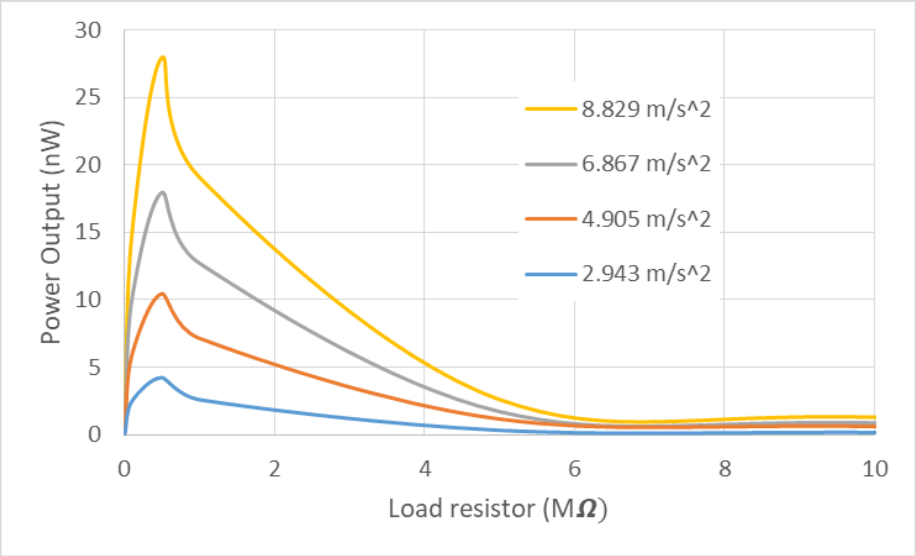

Figure 4-30: Output power at different level accelerations.

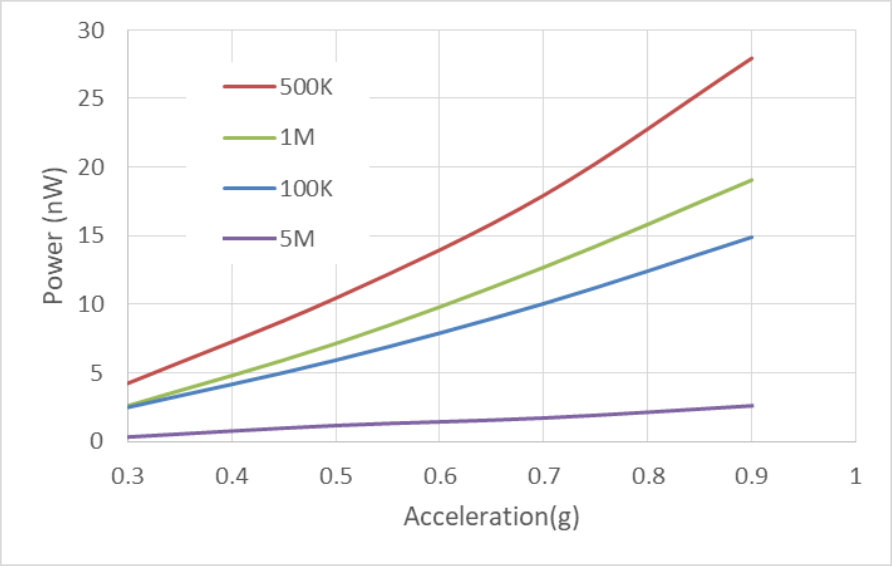

Figure 4-31: Power output as a function of different accelerations where 1'g' = 9.81m/s$^2$.

Further evaluations were conducted by adding another additional proof mass on top of free-standing piezoelectric cantilever device. The total weight of tungsten mass on top of the device was 0.26g. The resonant frequency of the free-standing cantilever with increased tungsten mass decreases from 201 Hz to 104 Hz at 6.867 m/s$^2$, as expected. However, the results from Figure 4-32 show different cantilever behaviour whereby the level of nonlinearity of resonant frequency with amplitude is significantly greater than compared with the single tungsten mass. This soft nonlinear behaviour could be the combination effect of the increased effective mass and the elastic nonlinearity on the cantilever structure.

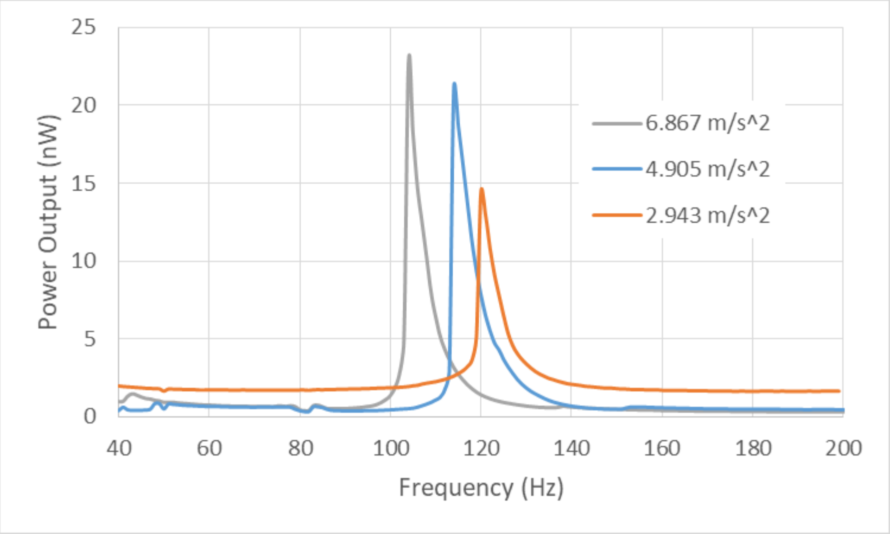

Figure 4-32: Experimental result of power output from double mass.

The maximum power output occurs at the same optimum load resistance as for the single tungsten mass which is at 500 k*Ω* shown in Figure 4-33. The power output level at the same acceleration is increased compared to the single tungsten mass e.g. 22.7 nW at 6.87 m/s$^2$ for the double mass compared with 17.95 nW at the same acceleration for the single mass. It is however, not possible to obtain results at 8.829 m/s$^2$ because this had caused the free-standing piezoelectric cantilever device to break as shown in Figure 4-34.

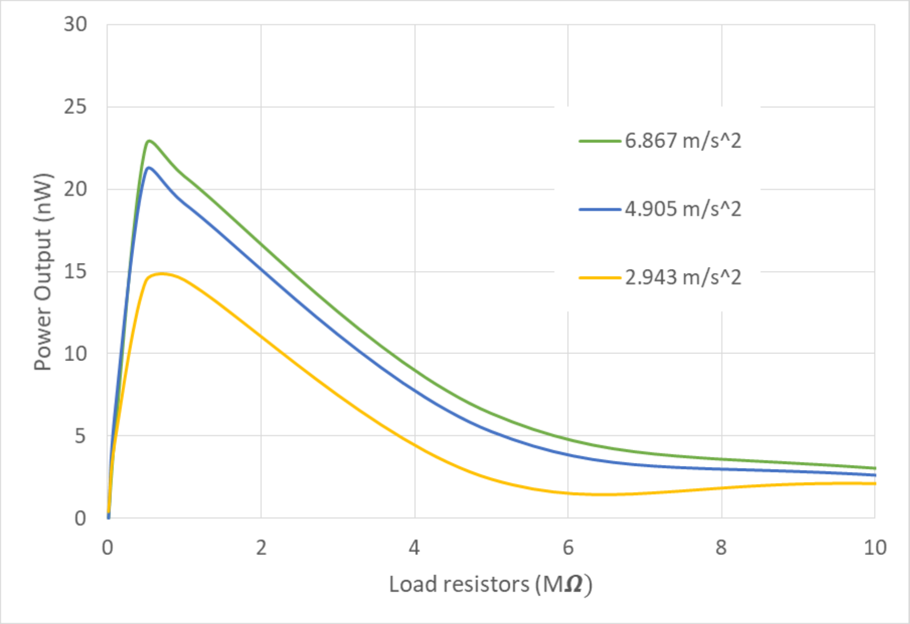

Figure 4-33: Optimum power output at 500 kΩ for double tungsten mass.

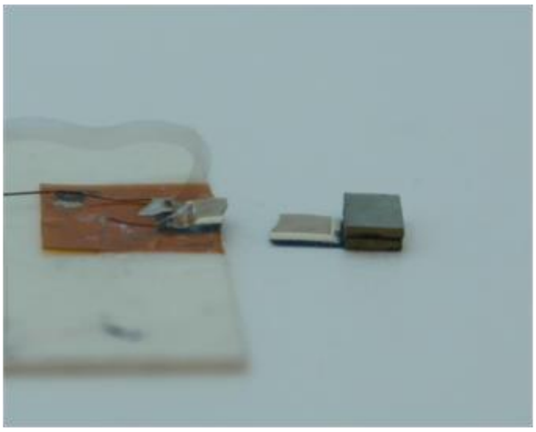

Figure 4-34: Cantilever with 0.26 tungsten mass broken at 8.829 m/s$^2$.

## 4.6 Summary and conclusion

This chapter demonstrates the design, fabrication and testing of free-standing piezoelectric cantilevers. The simulation results show that the stress distribution of the structure is mainly concentrated near to the anchor or the clamping area of the cantilever for the placement of piezoelectric layer. The resonant frequency and mode vibration of the device gave an estimation of the behaviour of the device. However, the resonant frequency achieved from experimental varied from simulation results due to the uncertainty of mechanical properties of the structure.

The cantilever devices were fabricated using Minico dielectric as the main structural component. The piezoelectric layer was placed as simulated to achieve the optimum power output for free-standing piezoelectric cantilever device. Poling process was perform at 90ºC for 6 minutes with an electric field of 3.7MV/m to active the piezoelectric layer. The average $d_{33}$ achieved was between -29 pC/N to -22 pC/N using piezoelectric polymer.

Evaluations on device with and without tungsten proof mass using dynamic test were conducted. A series of different experiments was carried out to evaluate the resonant frequency, cantilever displacement and output power of the device was analysed.

The resonant frequency before adding proof mass was at 1544 Hz and the maximum output voltage was 18.6 mV and the maximum tip displacement was 21.92 μm when the cantilever was excited at 12.75 m/s$^2$. The voltage output and the cantilever tip displacement shows a good correlation with the voltage and displacement increases as the acceleration increase.

By adding tungsten proof mass, the natural frequency decreases 86%. The testing result shows that electrical power output obtained was 27.9 nW excited at frequency of 201 Hz with load resistance of 500 k***Ω***. Another additional proof mass was added and the result shows that the electrical power output increases for 21% and the natural frequency was lower down from 201 to 104 Hz at 6.867 $m/s^2$. However, the presence of 0.26g of tungsten mass on top of the cantilever is not desirable as the soft nonlinear behaviour is more obvious and may cause the device to break.

The Q-factor of the device determines the sharpness of the frequency-amplitude response, which defines the frequency span where the device could be usable. The low Q-factor (e.g. 42.94 and 12.93 for cantilever without mass and with tungsten mass respectively) of the device indicates suitability for broader bandwidth applications being able to accommodate small deviations in the exciting frequency. Any small deviations will not cause a large decrease in power output. However, it also indicates high energy losses which is not good for the maximum level of power output from the energy harvester.

The power output achieved from these free-standing piezoelectric cantilever device fabricated solely using screen-printing method had shown a promising progress in enabling energy harvesting on textile. With low temperature processing and a direct fabrication method on textile, kinetic energy harvesting on fabrics is possible.

Further evaluations of the different structures, such as the encastre beam, will be discussed in detail in next chapter.

# 5. Device 2: Screen-printed free-standing encastre beam

## 5.1 Introduction

This chapter explores the design, fabrication and testing of encastre beam with multiple layers on flexible substrate using low temperature processes identified in previous chapters.

The device demonstrated in this chapter is an encastre beam i.e. clamped at each end. The structure is ideal for use as strain sensing resonator and is combined with piezoelectric layers for exciting and detecting the beams vibrations.

This chapter includes the following:

- An introduction to resonator
- Design and fabrication device
- Experimental setup and testing of the device

The experimental evaluation initially involved testing the piezoelectric element on one end of the beam at a time. The response of the piezoelectric elements has also been evaluated using a shaker rig with varied acceleration levels. The resonant frequency of the device is presented and discussed and the influence of operation in air and vacuum is explored.

## 5.2 Resonant Sensors

A resonant sensor consists of mechanical structure which vibrates at its resonant frequency [92]. The frequency of the resonating structure is affected by the measurand

and varies as the measurand changes. Typically, the measurand can be affected by three ways as follows:

- Varying the stiffness of the resonator.
- Altering the resonator mass.
- Changing the shape of the resonator.

The most common coupling mechanism is to apply a varying strain to the resonant structure. A sample device from the University of Twente, Netherlands, is a bridge force sensor fabricated using silicon micromachining processes. When an external force is applied to the bridge structure, this places the vibrating bridge structure in compression or tension. These compressive or tensile forces alter the mechanical stiffness of the structure which in turn changes the resonant frequency of the bridge [93]. This principle is mostly implemented in force sensors, accelerometers, and pressure sensors to name a few.

Another common coupling mechanism is to change the frequency of vibration by altering the mass of the resonant structure. This can be achieved by surrounding the structure with a liquid or gas. The presence of such a fluid increases the resonator's inertia and changes its resonant frequency. The resonator can be coated with a chemically sensitive material in order to realise a gas sensor. The sensitive material absorbs the particular gas molecules, thus adding to the mass of the resonator structure. This will again reduce the frequency of the resonator [94].

Changing the shape of the resonator is the least commonly implemented coupling mechanism. This effect is similar to the strain effect except the change in the measurand alters the geometry of the resonator which leads to a shift in the resonant frequency [95].

Another very important parameter to consider in resonant sensor is mechanical quality factor or Q-factor. The Q-factor is a measure of energy losses in resonant sensor, low energy losses indicates high Q-factor. One common method used to calculate the Q-factor is from the amplitude-frequency spectrum of the vibration by $Q = f_0/\Delta f$, where $f_0$ is the resonance frequency and $\Delta f$ is the bandwidth at half of its peak value. In other words, the resonant peak from the amplitude-frequency diagram is high and narrow when the Q-factor is high. A high Q-factor is desirable as it has good frequency stability, low energy required to maintain oscillation and high resolution.

The Q-factor however, is highly influenced by damping mechanism. There are three main damping mechanisms which are; viscous and acoustic damping, damping due to the support of resonator and damping resulted from internal material related. The most significant damping mechanism is due to the interaction with surrounding fluid which can be avoided by operating the resonant sensor in vacuum condition.

Most of the resonant sensors were fabricated using silicon wafer technology for many years. This technology has proven to produce identical, small, low-cost sensors with or without integrated electronics on the sensor chip. Silicon is also a highly attractive resonator material since it exhibits an intrinsically low level of internal damping. However, this fabrication technique and the use of silicon is not compatible with fabrics due to the use of chemicals, temperatures and processes which will jeopardise the properties of the fabric. Screen-printing fabrication technique on the other hand, provides an alternative for such sensitive substrates.

## 5.3 Design and modelling

An encastre beam is a type of free-standing beam structure which has both ends fixed to the substrate (in contrast to a cantilever beam whereby only one end of the structure is fixed. It is a good choice for use as strain sensor since strain can be applied through the substrate to one or both ends of the beam. The encastre beam is analysed using the same techniques described in chapter 4.

The encastre beam structure was simulated to predict the beams resonant frequency and the stress distribution along the length of the beam. The stress distribution was evaluated using static finite element analysis to obtain the optimum position of piezoelectric. The excitation direction of the simulation was normal to the surface of the encastre beam. A force of 1 N was applied to Y-direction of the structure to investigate the maximum stress location on the structure.

The maximum stress during deformation was found to be near both clamped area. By placing the piezoelectric elements in this region, the maximum degree of mechanical coupling between the piezoelectric layer and resonant structure could be obtained. Figure 5-1 and Table 5-1 shows the details of the simulated structure of the encastre beam.

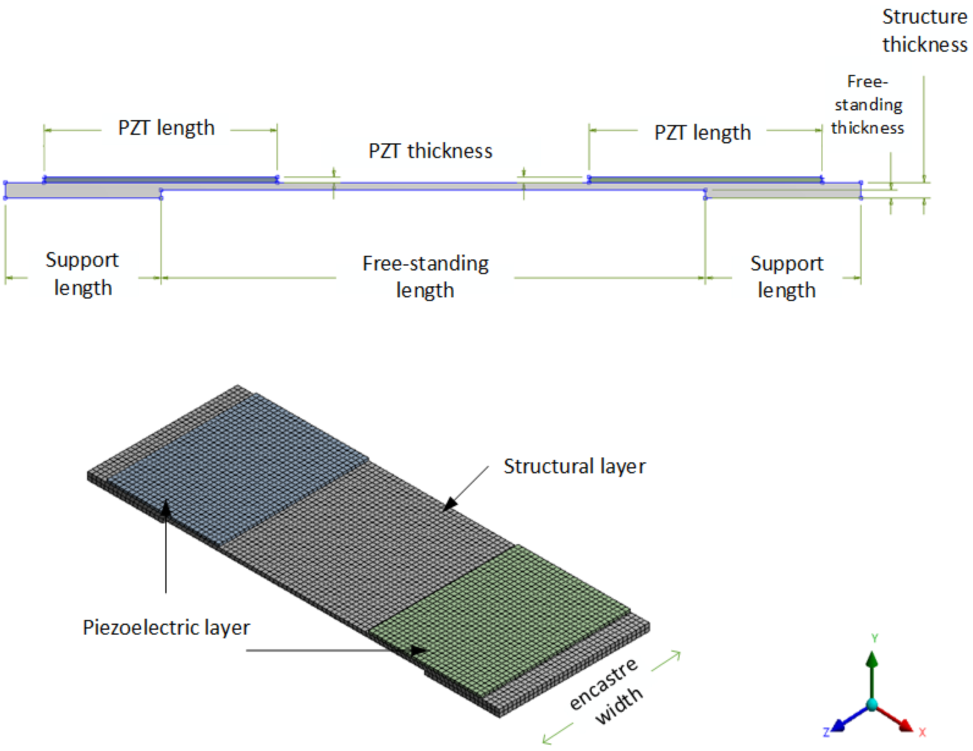

Figure 5-1: Encastre beam design and structure.

Table 5-1: Parameter of encastre beam.

| **Parameters** | **Values** |
|---|---|
| Total length (mm) | 11 |
| Width (mm) | 4.0 |
| Support length (mm) | 4.0 |
| Free-standing thickness (μm) | 200 |
| Structure thickness (μm)* | 240 |
| PZT thickness (μm)* | 66 |
| PZT length (mm) | 3.0 |

### 5.3.1 Modal analysis

The results from the modal analysis of the encastre beam indicate the resonant frequency is much higher compared to cantilever structure as expected. This is due to the boundary conditions of the structure, which makes it much stiffer.

For example, in the first fundamental mode the frequency was 4.44 kHz and the encastre beam was oscillating in the Y-direction as shown in figure 5.1. The frequency of the encastre beam are 6 times higher compared to cantilever beam at the first mode. The frequency of the second mode of the beam was 6.59 kHz, and this is a torsional mode with both sides of the beam deforming. Figure 5-2(a) and Figure 5-2(b) show the structural deformation for both the fundamental flexural and fundamental torsional modes of the encastre beam.

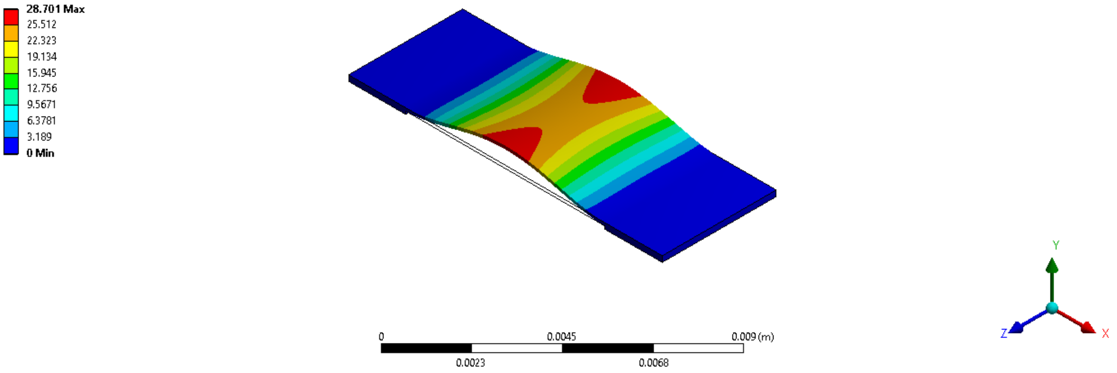

(a)

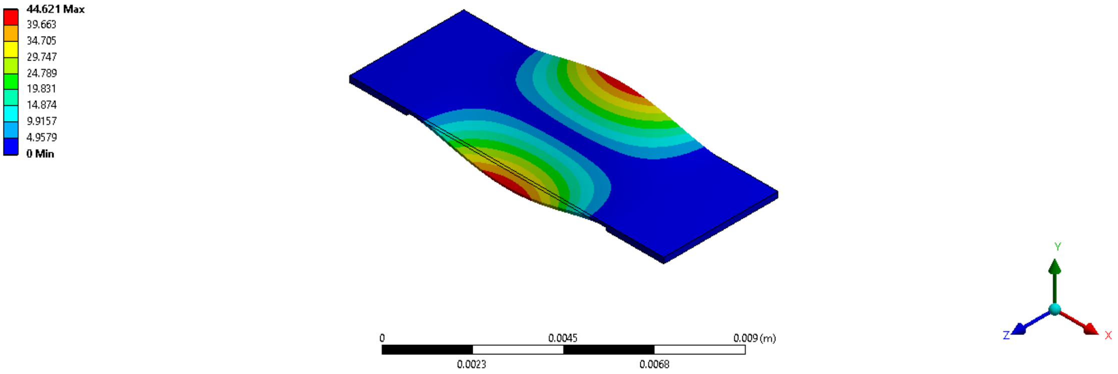

(b)

Figure 5-2: (a) First and (b) second mode of encastre beam.

The third and fourth vibrations happened at 11.62 kHz and 14.55 kHz respectively. The structure deformation of the third vibration is illustrated as a wave-like movement and this is the second order flexural mode. The maximum deformation was focused on the side of the structure as shown in Figure 5-3(a). The fourth mode is the second order torsional mode and the deformation of the structure was more complex as illustrated in Figure 5-3(b).

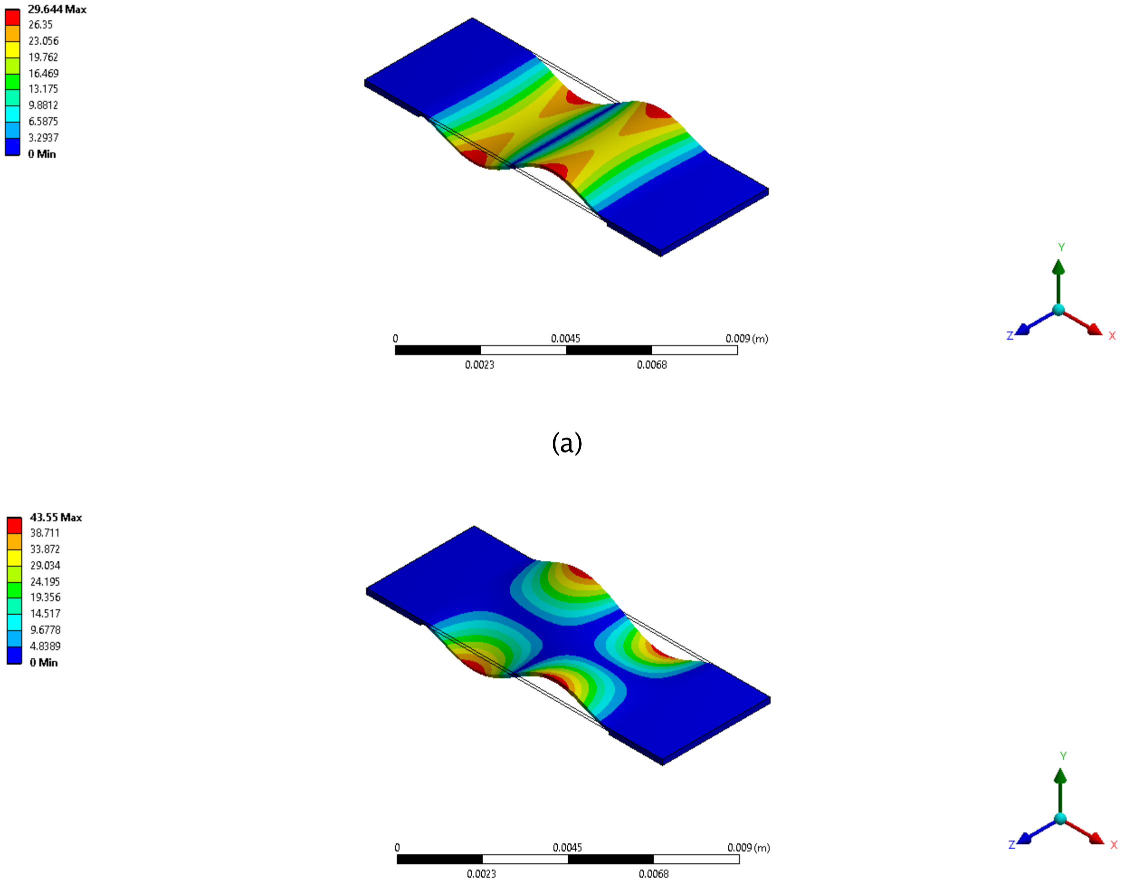

(a)

(b)

Figure 5-3: (a) Third and (b) forth mode of encastre beam.

The optimum position of piezoelectric was evaluated using static finite element analysis and the maximum stress during deformation was found to be near both clamped area as shown in Figure 5-4 as expected. However, the stress decreases along the free-standing encastre beam length on both side until the inflection point. Extending the piezoelectric elements beyond the inflection-points wold result in strain averaging and thus less effective.

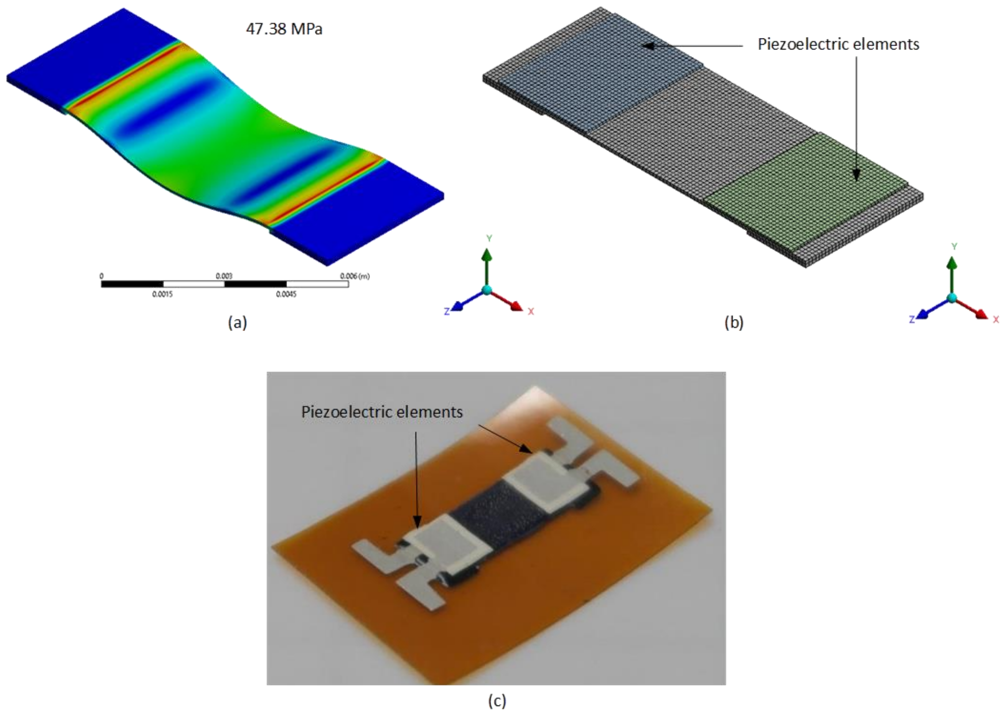

(a)

(b)

(c)

Figure 5-4: (a) Maximum stress in the Y-direction obtained from simulation, (b) illustration of piezoelectric elements and (c) actual fabricated device with piezoelectric elements.

## 5.4 Fabrication

### 5.4.1 Printing process

The fabrication process of encastre beam is the same as that used previously for the cantilever structure. However, the design of the encastre beam is slightly different with piezoelectric layers placed on both ends of the structure as illustrated in Figure 5-5. This matches the simulated structure and creates the excitation and detection mechanisms for the free-standing resonator beam.

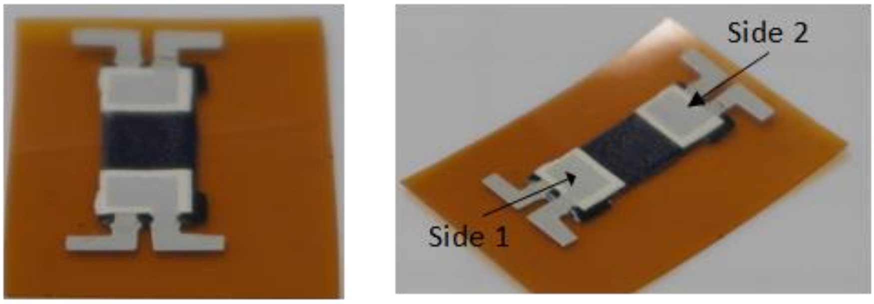

Figure 5-5: Encastre beam with piezoelectric layers on both end of the structure.

The fabrication process on Kapton starts with sacrificial layer deposited and cured at 80ºC for 3 minutes for each layer until the desired thickness is obtained. The PVA sacrificial paste, Fabink-TC-SF 6002, was supplied from Fabinks Ltd. However, if the devices are fabricated on fabric, another layer of interface is needed before sacrificial layer.

Next the Minico dielectric was printed to form the structure of the resonator. This was followed by the bottom electrode. The dielectric and bottom electrode were cured at 80ºC for 10 minutes and 130ºC for 5 minutes in the box oven. The process continues by printing the piezoelectric layer and the top electrodes on the resonator. The piezoelectric layer at each end of the beam is sandwiched by two silver electrodes. The top electrode of the resonator was cured as the same way as the bottom electrode.

There are two types of piezoelectric material used in this work which are ECS-PolyPZT SZ and ECS-PolyPZT SS. The curing process of both piezoelectric layer was also conducted in box oven and cured at 110ºC for 10 minutes and 90ºC for 6 minutes respectively. The paste characteristics and formulation are different and explained more by Ahmed et al [90] and will not be discussed further. The curing parameters of each layer are summarised in the Table 5-2 and the fabrication sequence is as shown in Figure 5-6 and Figure 5-7.

Table 5-2: Curing parameters for encastre beam.

| **Layers** | **Paste** | **Curing parameters** |
|---|---|---|
| Interface layer* | Fabink-IF-39 | UV 60 seconds |
| Sacrificial layer | Fabink-TC-SF 6002 | 80 ºC 3 minutes |
| Structural layer | Minico M 7000 | 80 ºC 10 minutes |
| Electrodes layer | Johnson Matthey S-20 | 130 ºC 5 minutes |
| Piezoelectric layer | ECS-PolyPZT SZ | 110 ºC 10 minutes |
| | ECS-PolyPZT SS | 90 ºC 6 minutes |

*used for printing on fabric

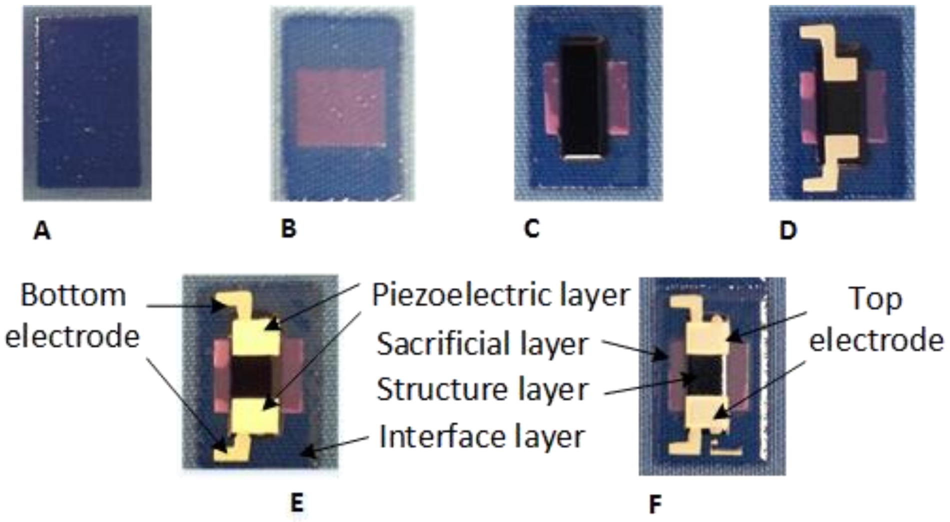

Figure 5-6: Printing sequence for encastre beam on fabric: A. Interface layer, B. Sacrificial layer, C. Structural layer, D. Bottom electrodes, E. Piezoelectric layers, F. Top electrodes.

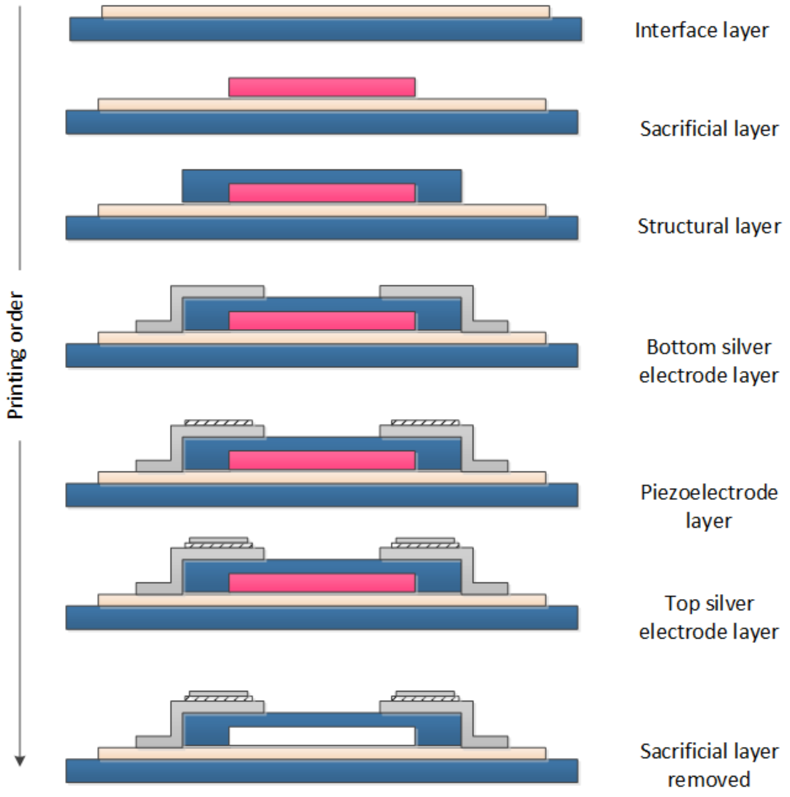

Figure 5-7: Printing sequence for free-standing piezoelectric encastre beam.

Incomplete printing of top electrodes can be observed on both ends of the encastre beam in Figure 5-8 which meant the top electrode was not connected to the contact electrode on the interface layer and in some cases the contact electrode was not printed correctly. This is due to the thickness of the layers which have built up resulting in a large step between the top of the piezoelectric layer and interface layer. This could potentially be improved by extending the structural layer such that the contact electrode sits on the structural layer and not on the interface layer. This will reduce the step height to just the thickness of the piezoelectric layer.

In order to achieve a free-standing encastre beam, the sacrificial layers was removed in 90ºC agitated water. The resonator device before and after the removal process are illustrated in Figure 5-8. No significant deformation such as bending and sagging of the encastre beam was observed. The process also shows that there is no visible change in the fabric.

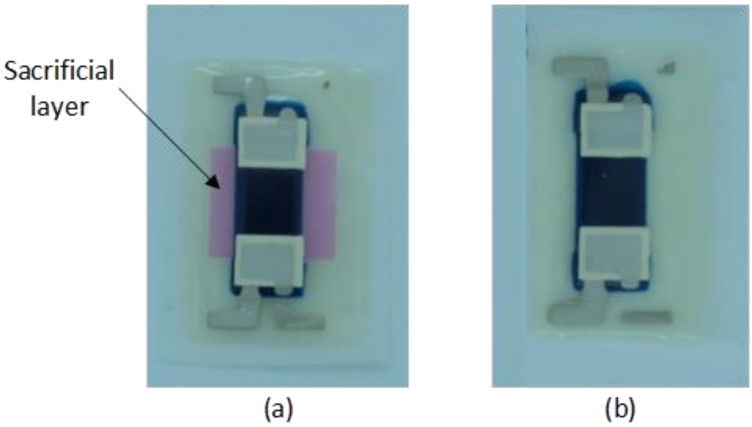

Figure 5-8: Encastre beam (a) before and (b) after removal process.

An SEM image from the side of the device that shows the sacrificial layers has been completely removed and there is no residue remaining as in Figure 5-9. This indicates a free-standing piezoelectric encastre beam had successfully fabricated using solely screen-printing method.

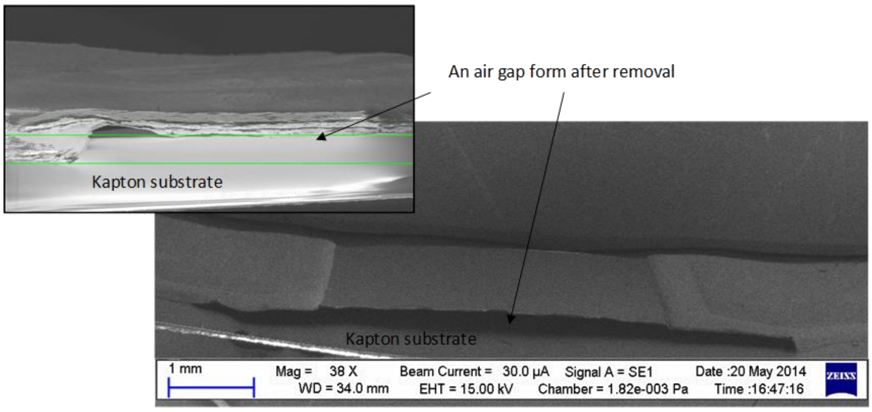

Figure 5-9: Free-standing encastre beam after removal process.

### 5.4.2 Poling process

Wires were connected using a conductive silver epoxy to the contact pads at each end of the encastre beam before the polling process. The poling process was undertaken in a controlled poling rig as described previously in 4.4.1. The device was connected in parallel to a high voltage supply and placed on hotplate as shown in Figure 5-10. The hotplate was heated up to the required temperature (90˚C) while the device was on it and, after the temperature had stabilized to 90˚C, the voltage supply was turned on for the required poling time (6 minutes). At the end of the poling process, the device was allowed to cool down with the voltage being maintained. After poling the $d_{33}$ value was measured at each end of the resonator as described previously in section 4.4.1.

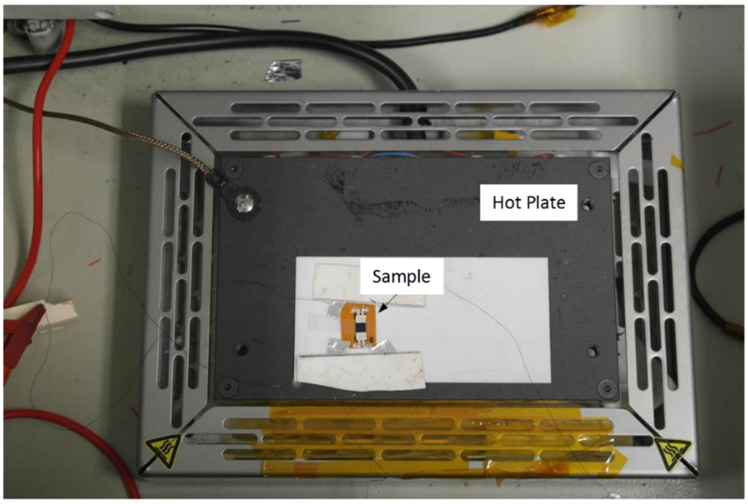

Figure 5-10: Device poled on poling rig.

Figure 5-12 and Figure 5-13 show $d_{33}$ values for ECS-PolyPZT SZ and ECS-PolyPZT SS respectively. The average $d_{33}$ values for ECS-PolyPZT SZ is 16 pC/N and for ECS-PolyPZT SS is 29 pC/N. ECS-PolyPZT SS is the improved polymer PZT paste and this is reflected in the measured $d_{33}$ which is nearly 2 times higher than the $d_{33}$ results from the ECS-PolyPZT SZ. Four samples were successfully poled from both types of piezoelectric elements (e.g. ECS-PolyPZT SZ and ECS-PolyPZT SS) and the measurements were taken from side 1 and side 2 of the piezoelectric elements on each samples as in Figure 5-11. The $d_{33}$ values was measured using the piezometer as described in section 4.4.1.

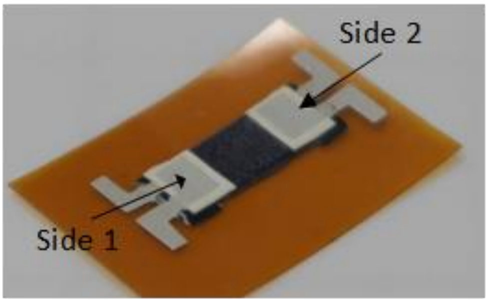

Figure 5-11: Side 1 and side 2 of the piezoelectric elements on the printed sample.

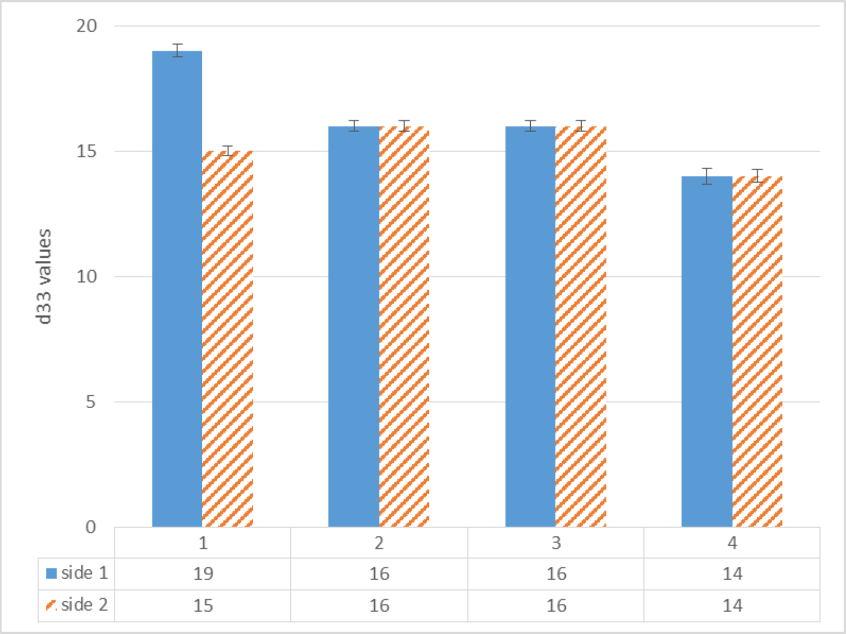

| | 1 | 2 | 3 | 4 |
|---|---|---|---|---|
| ■ side 1 | 19 | 16 | 16 | 14 |
| ▨ side 2 | 15 | 16 | 16 | 14 |

Figure 5-12: $d_{33}$ values for ECS-PolyPZT SZ paste.

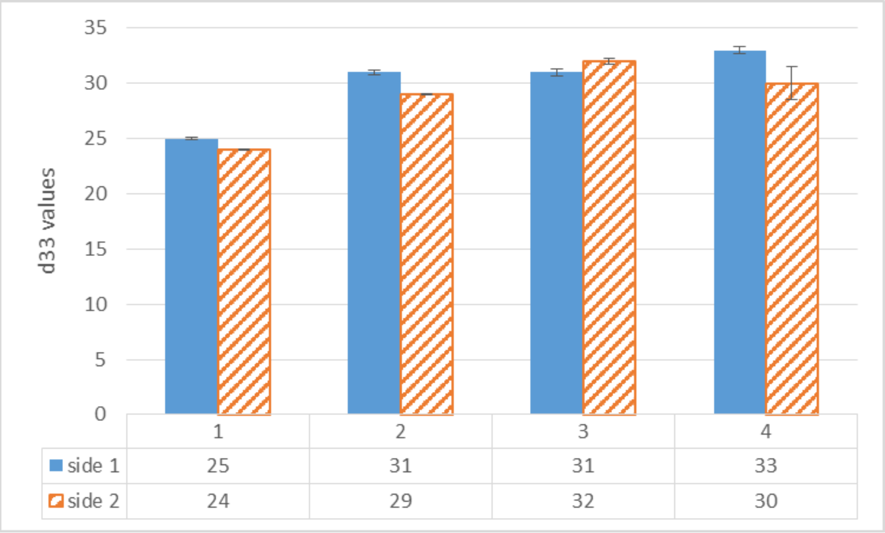

| | 1 | 2 | 3 | 4 |
|---|---|---|---|---|
| ■ side 1 | 25 | 31 | 31 | 33 |
| ▨ side 2 | 24 | 29 | 32 | 30 |

Figure 5-13: $d_{33}$ values for ECS-PolyPZT SS paste.

These results confirmed that the fabrication and poling processes were successful. The mechanical structure has been successfully realised and the piezoelectric elements fabricated without short circuits and have been successfully polarised. This demonstrates the compatibility of these processes with a fabric substrate.

## 5.5 Evaluation

### 5.5.1 Setup

To evaluate the performance of the encastre beam and further check whether the encastre beam was completely released from the substrate, the devices were tested on the shaker rig. The device was placed on an electromechanical shaker as illustrated in Figure 5-14(a) and the piezoelectric elements were connected to a charge amplifier. Figure 5-14(b) shows the schematic diagram of the charge amplifier used to amplify the output from the piezoelectric layer output.

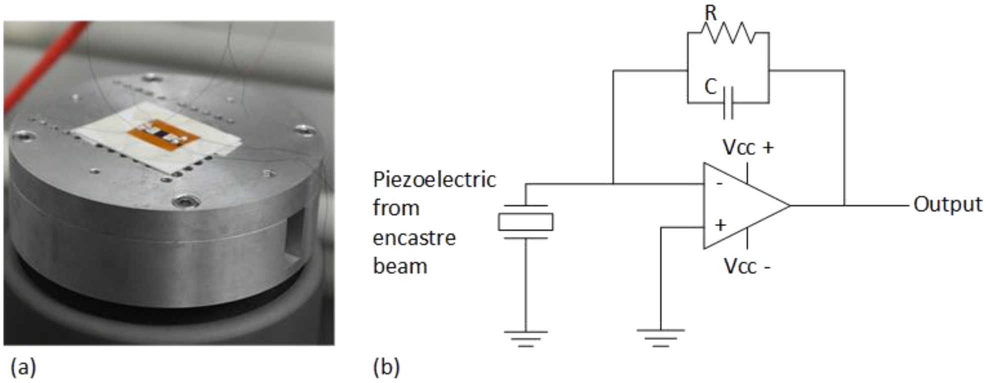

Figure 5-14: (a) device on electromechanical shaker and (b) schematic diagram of charge amplifier.

Initially each piezoelectric element was tested independently the piezoelectric output voltage was measured over a frequency range of 3.7 kHz to 5.0 kHz at different acceleration levels. The piezoelectric elements were then connected in series and the voltage output was recorded.

### 5.5.2 Result

Figure 5-15 shows the root mean square (RMS) voltages from the piezoelectric element (ECS-PolyPZT SZ) at side 1 plotted against frequency over a range of 3.7 kHz to 3.9 kHz with increments of 1 Hz at three different acceleration levels which were 0.49 m/s$^2$,0.98 m/s$^2$, 1.96 m/s$^2$ and 2.94 m/s$^2$.

Figure 5-15: Voltage output of piezoelectric elements in side 1.

The mechanical resonant frequency varied between 3.832 kHz to 3.838 kHz as the acceleration amplitude increased. The voltage output off resonance is approximately 0.15325 V and this increases up to 0.1546 V at resonant frequency and then falls away. The experimentally measured resonant frequency is more than 600 Hz lower compared to the simulation results. This may be due to the uncertain material properties of the encastre beam and the tolerances in the fabrication process leading to variations in layer thicknesses and the position of the piezoelectric elements.

Further experiments were conducted by first, evaluating one-side of the piezoelectric elements on the sample and second, connecting both piezoelectric elements in series on electromechanical shaker. A new sample using ECS-PolyPZT SS paste was evaluated as the $d_{33}$ value was much higher than the previous sample. The sample was first analysed over the same frequency range as previously. However, there was no response from the sample. The frequency was increased and resonance was detected in the frequency range of 4.5 kHz to 4.95 kHz. The frequency shifted from 3.83 kHz (previous sample) to 4.5 kHz due to the variation in thickness printed for the sample. The ECS-PolyPZT SS sample is more than 1.2 times thicker than previous sample. The RMS voltage recorded over this frequency range is illustrated in Figure 5-16 and Figure 5-17 for voltage output on side 1 and with both piezoelectric elements connected in series respectively. The voltage output from one side of piezoelectric element is 0.00018 V at acceleration of 0.491 m/s$^2$. This result however, is very low compared to measurement taken from piezoelectric elements from ECS PolyPZT-SZ at the same acceleration. This result is due to low Q-factor of ECS PolyPZT- SS which is 32 compared to ECS PolyPZT-SZ which is 640. There are several possibilities that contribute to the lower Q-factor such as losses in the materials, the surrounding fluid and also losses through resonator's support. Further evaluation in vacuum chamber to overcome surrounding fluid effect is discussed below.

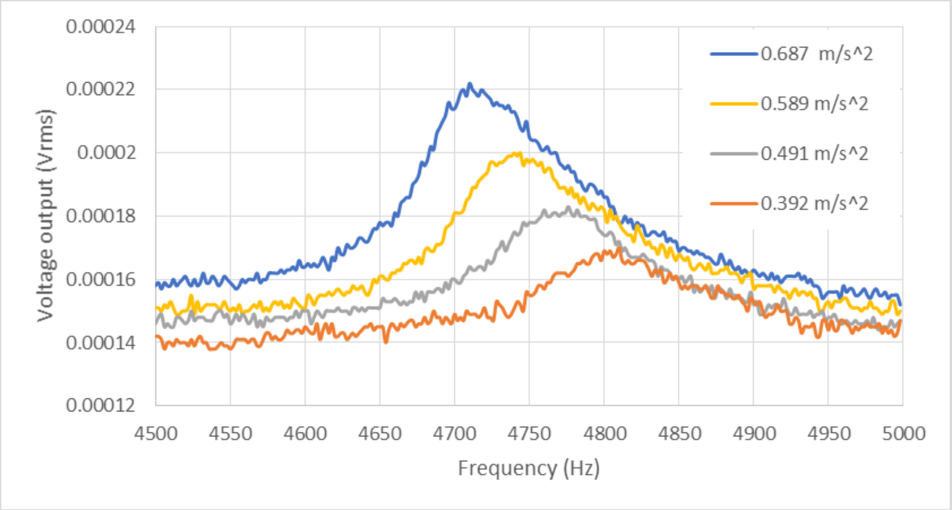

Figure 5-16: Voltage output from ECS-PolyPZT SS on side 1.

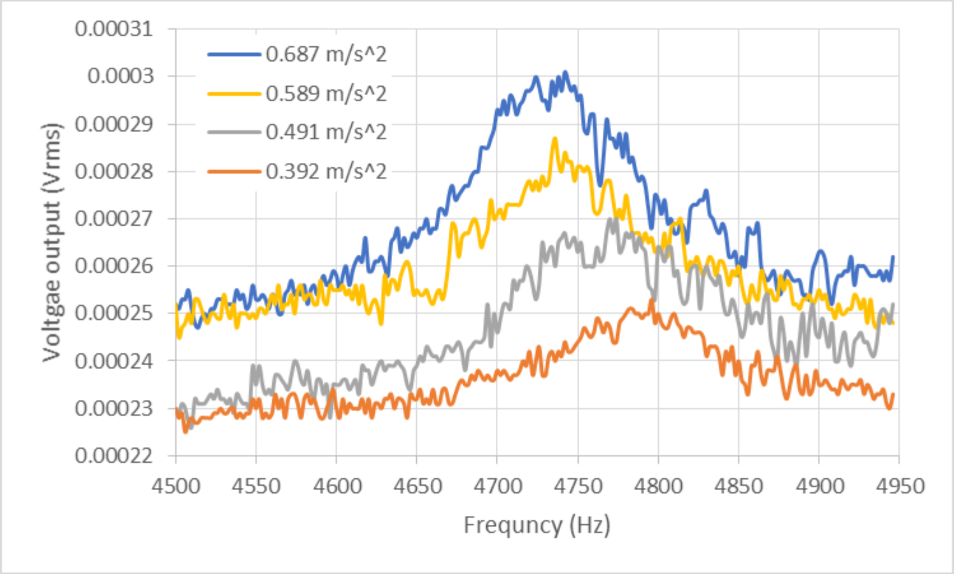

Figure 5-17: Voltage output from piezoelectric elements (ECS-PolyPZT SS) connected in series.

The results of piezoelectric elements connected in series show the voltage increased by 0.0000875 V at resonant frequency compared to measurement on one side of the piezoelectric elements with the same piezoelectric elements (ECS-PolyPZT SS). Both voltages increased as the amplitude of acceleration increases as expected and is shown in Figure 5-18. The resonant frequency occurs between 4722 Hz to 4796 Hz, for example, at acceleration of 0.589 m/s$^2$ the resonant frequency is 4736 Hz. From the results, the encastre beam shows a soft non-linear response as the amplitude of vibration increases and both sides of piezoelectric elements are working.

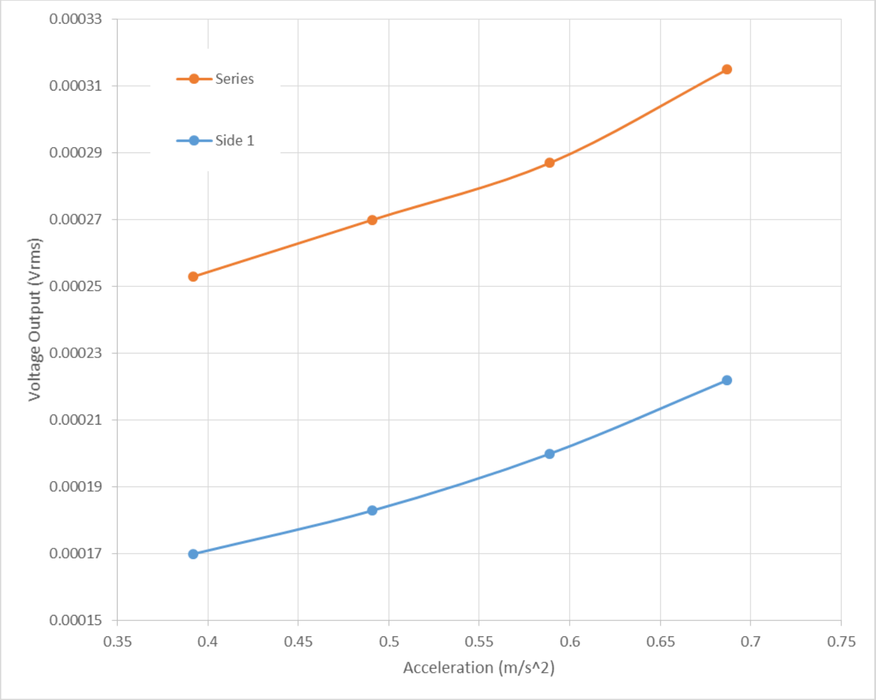

Figure 5-18: Voltage increases as acceleration increases.

The objectives of the encastre beam design were to successfully fabricate a free-standing resonator solely using screen-printing method with printed piezoelectric an excitation and detection mechanisms. The piezoelectric elements were also connected in a feedback loop shown in the block diagram in Figure 5-19. The driving voltage causes the excitation element to vibrate the beam and the deflection of the beam would be detected by the detection element. The detected signal would be a maximum at resonance due to the vibrational amplitude of the beam reaching its peak. This is a more realistic evaluation of actual operation as it allows the resonator maintain resonance as the measurand causes the frequency to change.

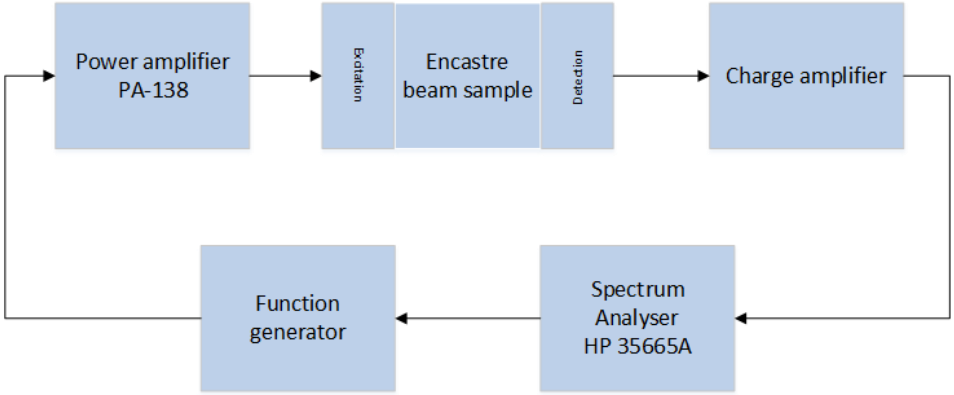

Figure 5-19: Experimental setup for excitation and detection mechanisms in feedback loop.

The resonator was first tested at atmospheric pressure to observe the excitation and detection mechanism. One of the piezoelectric elements on the resonator was used as the excitation element, which was driven by a power amplifier PA-138 from Labworks Inc. The power amplifier is able to produce voltage output up to 25 V. However, in this experiment the maximum voltage applied was 12 V. The piezoelectric elements on the detection mechanism were connected to a charge amplifier and a second stage amplifier. The circuitry was placed in a metal box to external interference and noise. The output from charge amplifier was then connected to a HP 35665A Spectrum Analyser with the tracking generator scanning over a frequency range of 40±120 kHz. The drive voltage was varied between 1 V to 12 V pk-pk to observe the resonant frequency which was believed to happen at the range between 4 kHz to 5.5 kHz as the same sample was used. However, the resonant frequency was not visible. This was due to the signal being too small to be observed which in turn is due to the driving element not delivering sufficient energy to overcome the damping effects.

Since air damping is typically the most significant source of damping, the device was tested in a vacuum. This will reduce the damping effect of the surrounding fluid leading to a higher Q-factor, greater beam displacement and therefore increasing the output signal from the detection element. The resonator was placed in a vacuum chamber as shown in Figure 5-20 and tested using the same setup as shown in Figure 5-19.

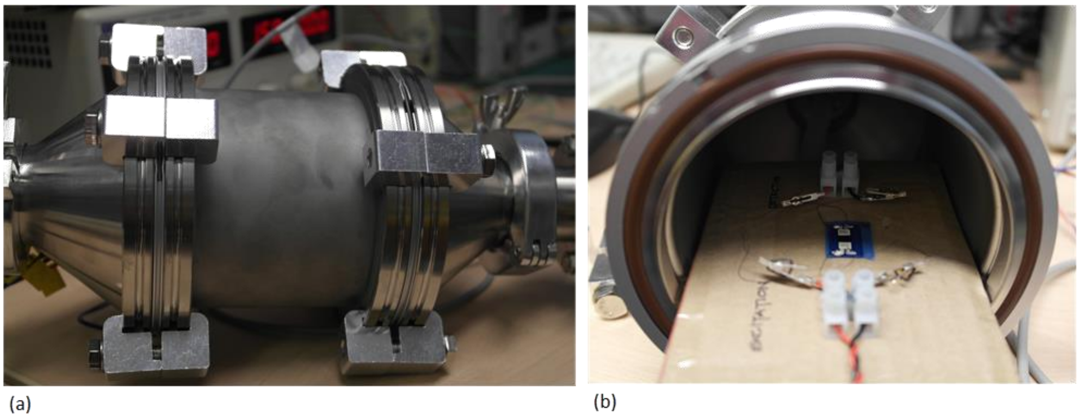

Figure 5-20: Device tested in vacuum chamber.

The peak in the signal occurred at 5 kHz as shown in Figure 5-21. However, a further test was conducted by disconnecting one side of the resonator (detection side) to verify the result. However, it was found that the resonant frequency was not from the mechanical device but interference from the electrical circuitry itself.

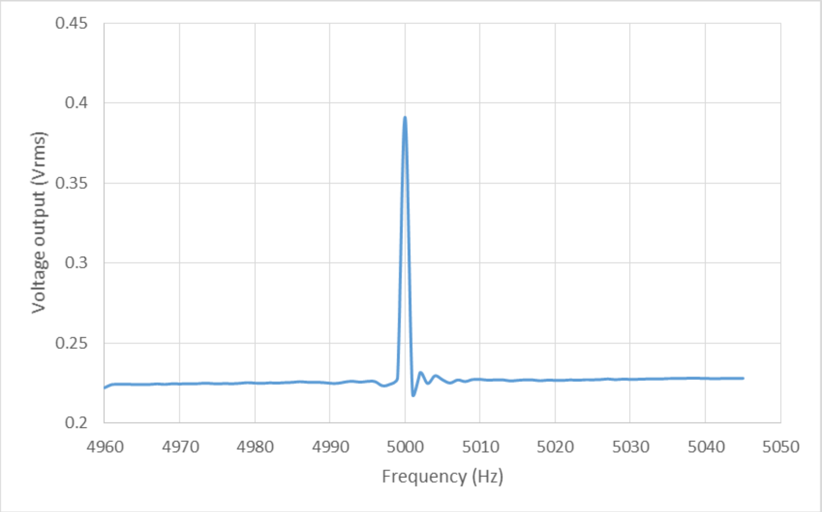

Figure 5-21: Resonator detection circuit response during vacuum test.

The resonant frequency of the encastre beam which is not visible even under vacuum condition is due to the piezoelectric driving elements output being insufficient to achieve a detectable amplitude of beam vibration. Operating in vacuum condition did not help because other sources of damping such as material losses were still too high.

## 5.6 Summary and conclusion

This work has presented a design, fabrication and testing of a free-standing encastre beam resonator fabricated solely using screen-printing method. Based on the simulated result, the piezoelectric elements were placed on the clamping area whereby the maximum stress was produced.

The encastre beam was then tested on one side of piezoelectric elements using the electromechanical shaker and the maximum output generated was 0.1545 volt at natural frequency of 3.835 kHz. The same experiment was repeated with both sides of piezoelectric elements connected in series. However, the output obtained was lower due to different acceleration levels. The same acceleration level could not achieved due to the limitation of the equipment.

The resonator is intended to work in a feedback loop with integrated piezoelectric drive and detection elements. However, the resonant frequency for both test in air and vacuum pressure was not detectable. The device did not respond accordingly possibly because the excitation part did not excite sufficient amplitude in the beam. Alternatively, it might be due to the presence of the piezoelectric elements altering the boundary conditions of the beam. The clamping point on the beam could move due to the presence of the piezoelectric layer. The added stiffness caused by the addition of the piezoelectric element could cause the effective clamping point to move to the edge of the piezoelectric element. This would result in greatly reduced levels of vibration at the locations of the piezoelectric elements. This could be improved by using more flexible piezoelectric material or higher $d_{33}$ values of piezoelectric materials.

# 6. Device 3: Screen-printed free-standing diaphragm

## 6.1 Introduction

This chapter demonstrates the fabrication of a free-standing piezoelectric diaphragm on a flexible substrate using the selected materials. In chapter 4 and chapter 5, a cantilever and encastre beam have been fabricated and tested with each of the structures addressing different applications. In this chapter, additional complexity in terms of design is presented by fabricating diaphragm structure.

Two types of structure which are circular and square diaphragms with two different designs of each are introduced. These structures are simulated and the maximum stresses identified. The piezoelectric elements are placed, based on the simulation results, to maximise the coupling between the piezoelectric elements and the structure.

Unlike the cantilever or encastre beam, the diaphragm structure has all the periphery clamped which may result in difficulty in removing the sacrificial layer. By presenting a channel through the side wall as part of the fabrication process, the removal process is achieved.

There are various types of buzzer or loudspeaker which are fabricated either by conventional microelectromechanical systems (MEMS) technologies or screen-printing. However, to the author's knowledge there are no publication on a screen-printed free-standing piezoelectric diaphragm on fabric. This report will focus on the fabrication process of the device on fabric and the results of the fabricated device.

The evaluation of the free-standing piezoelectric diaphragm was conducted in an anechoic room and the results are discussed and presented.

This chapter contains the following subsections:

- Introduction of a piezoelectric buzzer
- Fabrication and poling process for the diaphragm structure
- Evaluation of the diaphragm structure

## 6.2 Piezoelectric transducer

A piezoelectric transducer converts an electrical voltage or charge into vibrational mechanical energy. The piezoelectric transducer can be categorised by the nature of the vibrational energy it produces and the application to which the energy is applied.

In general, there are three application categories of piezoelectric transducers which produce audible sound, ultrasonic vibrations or ultrasonic signals. Audible sound transducers usually operate at frequencies below 20 kHz and are commonly used as a buzzer. Ultrasonic vibration on the other hand, had frequencies higher than 20 kHz and is used in ultrasonic cleaning equipment. Ultrasonic signals are used as transmitter and receiver for measuring distances in air or liquids. In this chapter, the fabricated device is focusing as an audible device or piezoelectric buzzer on a fabric. This device is possible to be implemented as an alarm for safety fabricated directly on fabric.

A piezoelectric buzzer is also known as a tone generator and is typically suitable for producing a high frequency sound output with small power consumption. The conventional structure of this type of transducer consists of a metal diaphragm bonded to a piezoelectric ceramic disk. When a voltage is applied to the piezoelectric disk, the disk deforms, causing the metal diaphragm to bend simultaneously. A sinusoidal voltage on the diaphragm causes it to vibrate at the resonance frequency and produce sound.

## 6.3 Design and modelling

The piezoelectric buzzer consists of piezoelectric elements sandwiched with top and bottom electrode on a free-standing diaphragm structure. There are two types of diaphragm introduced, these being a circular and square diaphragm which were evaluated. The static analysis was conducted on both of the structures using ANSYS workbench 15.0. The simulation parameters included were the diameter, length, thickness of the diaphragm structure, and force are applied in y-direction of the structure. The physical constants used in the simulations are the elastic modulus, Poisson’s ratio and the density of the material. The simulation parameters and design details of the diaphragm used are as in Table 6-1and Figure 6-1 respectively.

Table 6-1: Diaphragm parameters used in simulation.

| **Parameter** | **Value** |
|---|---|
| Diameter for circle diaphragm (mm) | 9 |
| Width (mm) | 9 |
| Support length (mm) | 4 |
| Free-standing thickness (μm) | 200 |
| Structure thickness (μm)* | 192 |
| PZT thickness (μm)* | 94 |

*values are based on SEM image taken

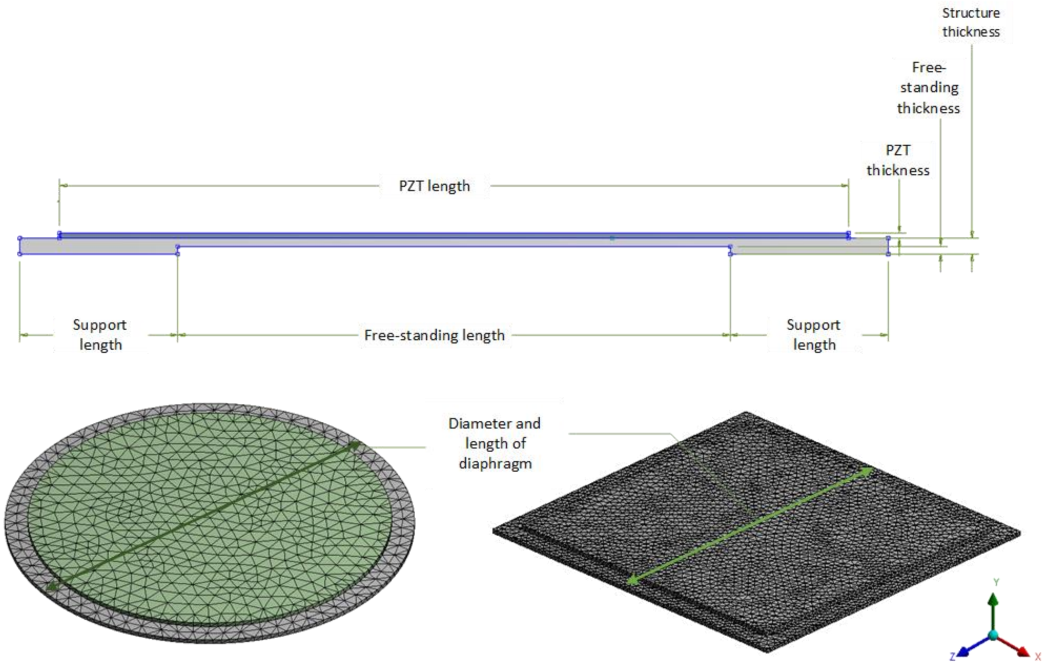

Figure 6-1: The two different designs of the diaphragm.

The thickness of the structure and the piezoelectric elements was confirmed by SEM an images of which are shown in Figure 6-2(a) and Figure 6-2(b) respectively. These values allow a good estimation as the thickness in screen-printing process is hard to control.

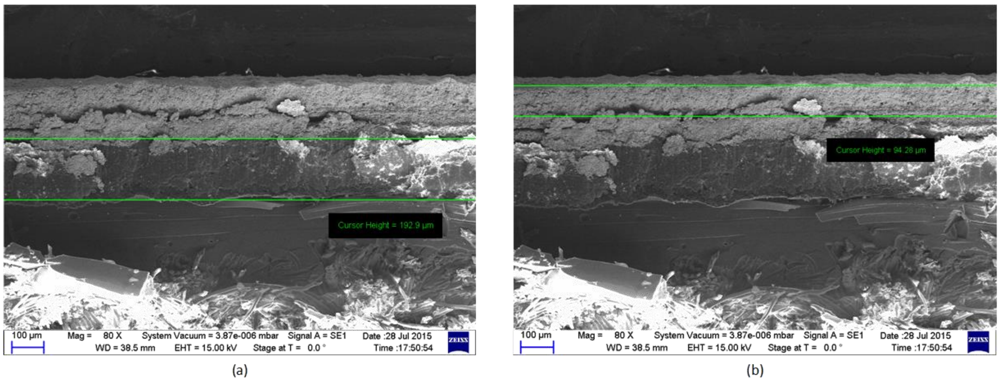

Figure 6-2: SEM image of (a) structural layer and (b) piezoelectric layer.

A force of 1 N was applied in y-direction to the surface of circular and square diaphragms. The stress deformation was formed on the circular structure which shows that the maximum stress was on the centre and around the structure near to the fixed area as illustrated in Figure 6-3(a). However, the stress distribution for the square diaphragm is lower compared to circular diaphragm and the maximum stress is on the side of the structure near to the fixed area rather than on the centre as shown in Figure 6-3(b).

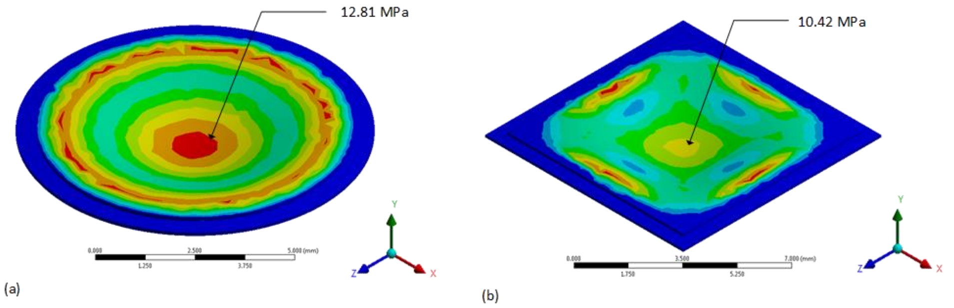

Figure 6-3: Stress distribution on (a) circular and (b) square diaphragm.

Based on the simulation results, the placement of the piezoelectric elements will be optimised to allow maximum coupling of piezoelectric elements with the structure. The design of the structure is as illustrated in Figure 6-4(a) double circular diaphragm and Figure 6-4(b) double square diaphragm. It is however, interesting to evaluate the diaphragm performance with the piezoelectric elements covering the whole diaphragm structure. This design is easily conducted by altering the design of the top electrode which are shown in details in next section.

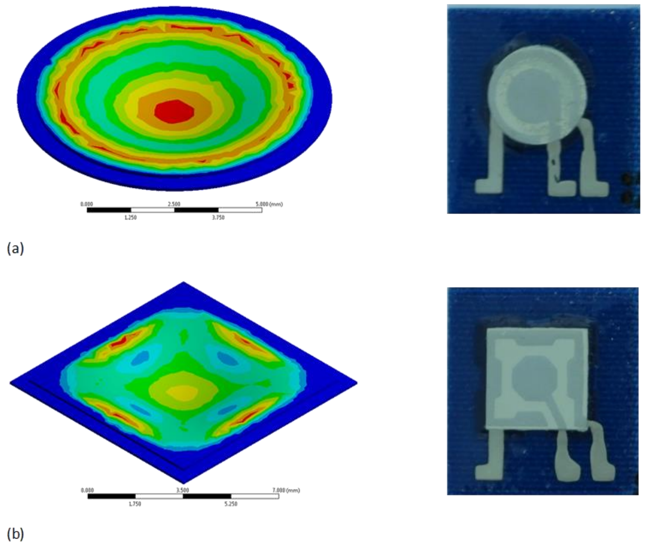

Figure 6-4: Design of the diaphragm structure based on simulation result.

## 6.4 Fabrication

### 6.4.1 Printing process

The printing process for diaphragm structure is more complicated compared to cantilever and encastre beam. This is due to the nature of diaphragm structure in which all the periphery is clamped. However, in this work, four small outlets were created in order to allow the sacrificial layer to be removed, thus making the structure free-standing. Figure 6-5 shows the printing sequence for constructing the outlets in diaphragm structure using sacrificial layer.

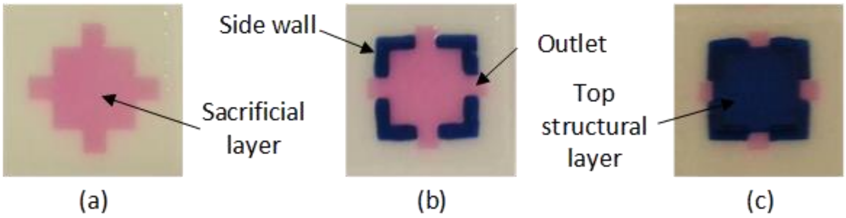

Figure 6-5: Screen-printing for diaphragm structure starting from (a) sacrificial layer followed by (b) side wall and (c) top structure layer.

As in the previous process for cantilever and encastre beam, the Kapton or fabric substrate was first glued on an alumina substrate in order to provide a rigid support. The sacrificial material was then printed until the desired thickness was approximately achieved. The side wall was then printed around the printed sacrificial layer with approximately the same height. Alignment is very crucial at this point to make sure that the side wall was not printed on top of the sacrificial layer. Then, the third layer was printed to achieve the top diaphragm layer. The whole printing process of a free-standing piezoelectric diaphragm consisted of seven printing process. The two types of structure were circular and square diaphragms divided into another two designs as shown in Figure 6-6. These design are implemented by changing the top electrode design. Both of the printing parameters and printing sequence are summarised in Table 6-2 and Figure 6-7.

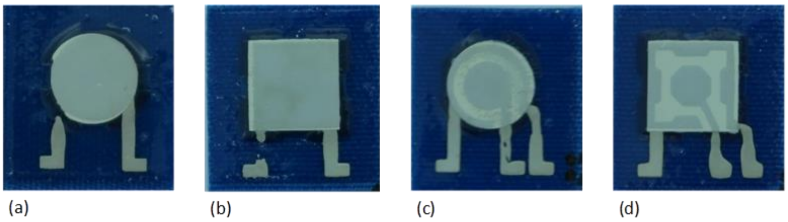

Figure 6-6: different design of free-standing piezoelectric diaphragm (a) circular diaphragm (b) square diaphragm (c) double circular diaphragm and (d) double square diaphragm.

Table 6-2: Printing parameters for diaphragm structure.

| Printing layers | Printing parameters | | |
|---|---|---|---|
| | **Printing Gap** | **Pressure** | **Curing condition** |
| Interface layer | 0.9 mm | 6.0 kg | UV 60 seconds |
| Sacrificial layer | 1.0 mm | 6.5 kg | 80 ºC 3 minutes |
| Side wall | 1.0 mm | 6.0 kg | 80 ºC 10 minutes |
| Top layer | 1.0 mm | 6.0 kg | 80 ºC 10 minutes |
| Bottom electrode | 1.4 mm | 5.0 kg | 130 ºC 5 minutes |
| Piezoelectric layer | 1.4 mm | 6.5 kg | 90 ºC 6 minutes |
| Top electrode | 1.4 mm | 5.0 kg | 130 ºC 5 minutes |

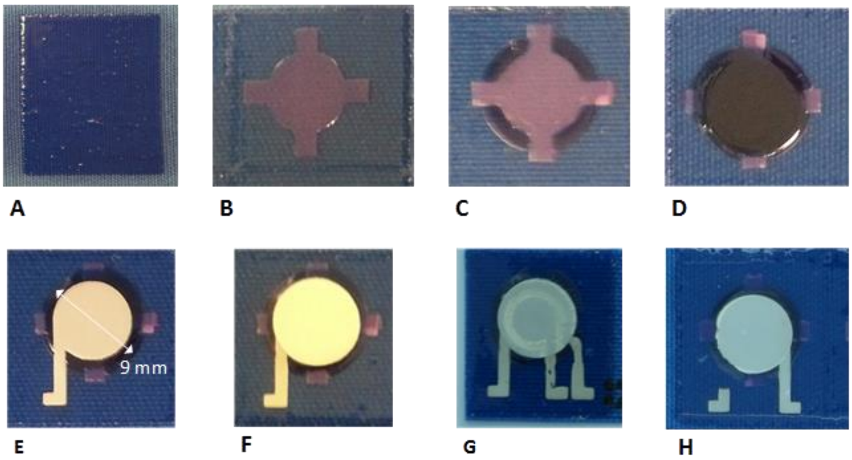

Figure 6-7: Printing process for circle diaphragm starting with (A) interface layer,(B) sacrificial layer, (C) side wall, (D) top layer, (E) silver layer, (F) piezoelectric layer, (G) and (H) are the top silver layers in the two different designs.

The process continues with the removal of the sacrificial layer from underneath the structural layer to release the free-standing structure. The removal process was conducted by submerging the sample in 90˚C agitate water as previous. The wires were connected to each of the electrode pads on diaphragm with silver epoxy before poling process. The device was connected to high voltage supply and placed on a hot plate. The hotplate was heated up to 90˚C while the device was on it and, after the temperature had stabilized, the voltage supply was turned on for 6 minutes to allow the piezoelectric elements to be activated.

Finally, the $d_{33}$ values were measured and Figure 6-8 shows the $d_{33}$ measurements for different diaphragms. It is worth mentioning that the value for design in 1 and 2 had much higher $d_{33}$ values compared to the design in 3 and 4. This is due to the top electrode area in design 1 and 2 being much wider as compared to design 3 and 4, which has resulted in a lot more polymer PZT being activated and poled.

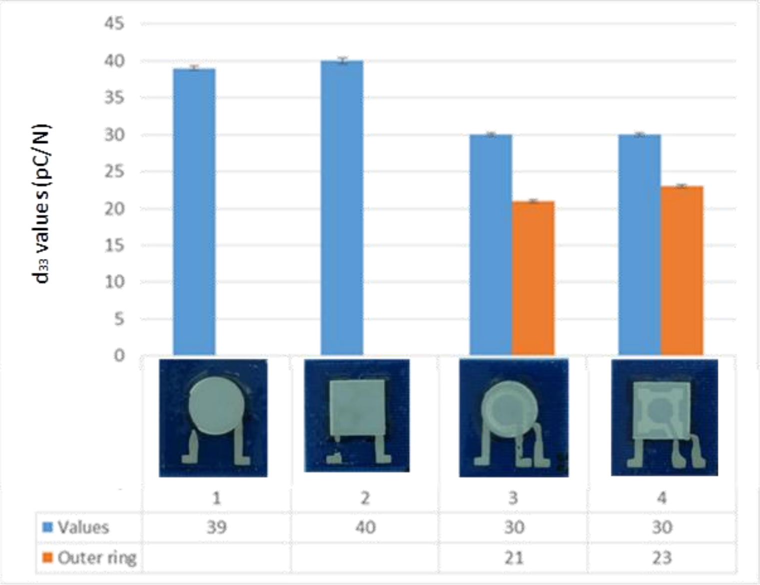

| | 1 | 2 | 3 | 4 |
|---|---|---|---|---|
| ■ Values | 39 | 40 | 30 | 30 |
| ■ Outer ring | | | 21 | 23 |

Figure 6-8: Measured $d_{33}$ values for piezoelectric elements on diaphragms structure.

## 6.5 Evaluation

### 6.5.1 Setup

The free-standing diaphragm structure was tested in an anechoic room to reduce the influence of interference. The frequency response of the emitted sound pressure level (SPL) was measured using an audio system which consisted of a microphone amplifier, a microphone and a mixed signal oscilloscope (MSO7012B) as illustrated in Figure 6-9.

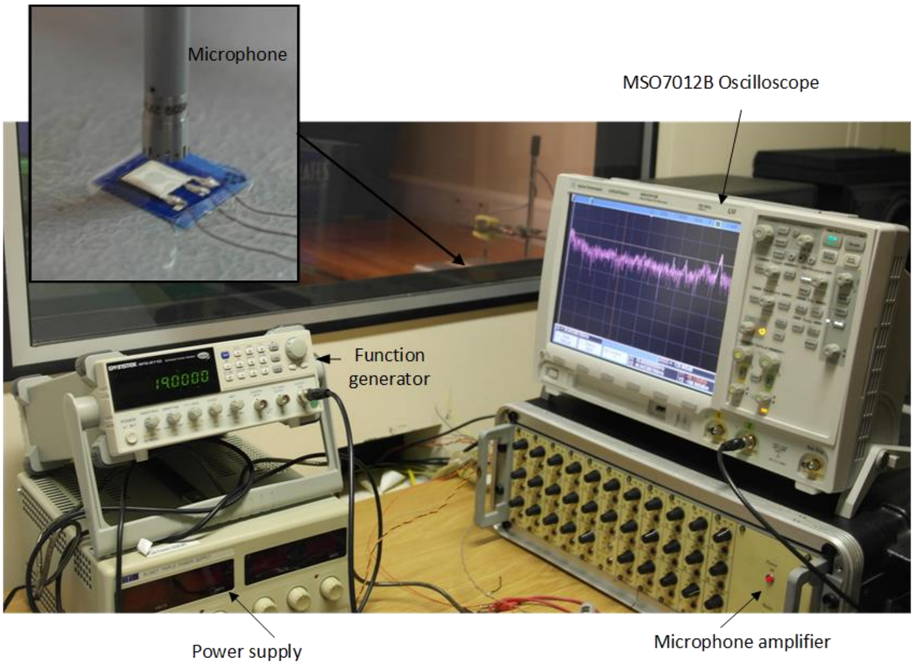

Figure 6-9: The free-standing diaphragm structure tested in anechoic room.

The free-standing diaphragm structure was driven by a 12 volt swept sine signal frequency ranging from 1 kHz to 20 kHz. The output was measured when the microphone was placed 15 mm from the free-standing diaphragm structure. Two types of diaphragm which were circular and square in two different designs were tested and the SPL of each device was recorded.

### 6.5.2 Result

Figure 6-10 shows the sound pressure level of two different circular and square diaphragms. The measurements were taken over a range of 1 kHz to 20 kHz with increments of 500 Hz. This range was selected to correspond to the human hearing range.

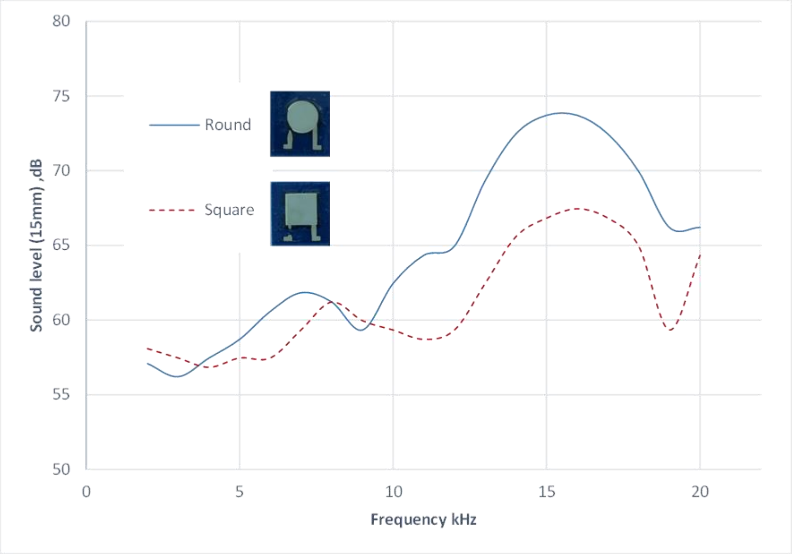

Figure 6-10: Measured sound pressure level for circular and square diaphragm structures.

The results show that the free-standing circular diaphragm structure had a maximum sound pressure level of 74 decibel between the frequencies of 13 to 19 kHz. On the other hand, the free-standing square diaphragm structure shows 7 decibel lower output than the circular diaphragm when the microphone distance was at 15 mm from the diaphragm with the same range of frequency. This result correlates with the simulation results which showed that the circular diaphragm had a higher stress distribution compared to the square diaphragm and hence, maximising the coupling between the piezoelectric elements and the mechanical structure.

A further test was conducted to evaluate the performance of the other two designs. Figure 6-11 shows the measurements taken at the same range of frequency as before. Both of the diaphragm's sound pressure levels increased gradually between the frequencies of 13 to 19 kHz. The double circle diaphragm shows 5 decibel higher compared to the double square diaphragm.

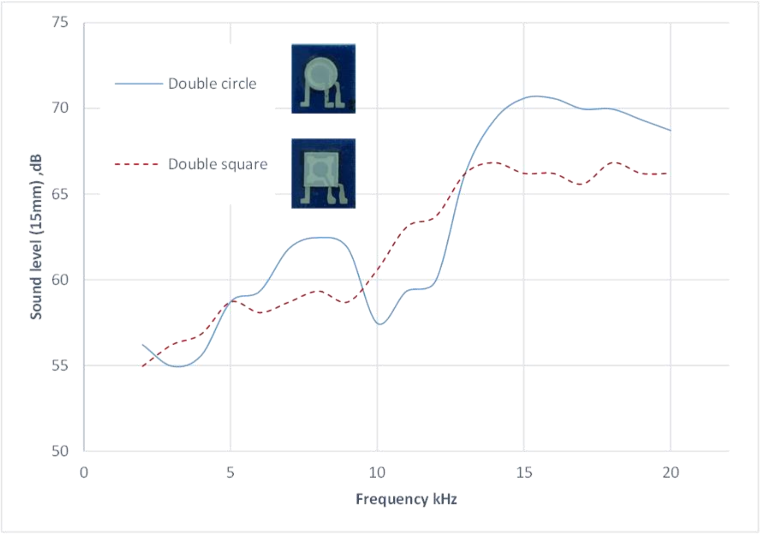

Figure 6-11: Sound pressure level for double circle and square.

Analysing these two different designs shows that in general, the circular diaphragm performed with slightly higher sound pressure level compared to the square diaphragm. The highest sound pressure level achieved was 74 decibel and the lowest was 66 decibel for the circular and double square diaphragms respectively. Both of the diaphragm's sound pressure levels increased in the same range of frequency which was from 13 kHz to 19 kHz. The area and the placement of piezoelectric elements highly influenced the outcome of the results.

A commercially available piezoelectric buzzer was evaluated to compare the performance of the screen-printed free-standing diaphragm structure. The highest sound pressure level was achieved at 128 decibel between the frequencies of 3 kHz to 5 kHz as illustrated in Figure 6-12. The $d_{33}$ value of the buzzer was 5 times higher than the screen-printed diaphragm, which is the reasons for the sound pressure level being much higher.

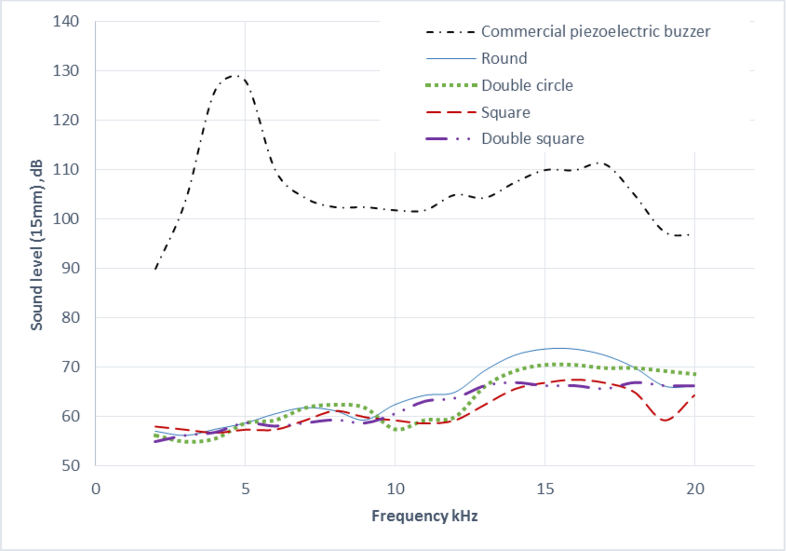

Figure 6-12: Measurement taken with commercially available piezoelectric buzzer.

## 6.6 Summary and conclusions

This chapter presents a fabrication technique to realise a free-standing diaphragm structure with piezoelectric elements solely using screen-printing method. This process was conducted directly on fabric at low temperatures process (<200˚C) to avoid altering the characteristics of the fabric. Based on the simulation result, the piezoelectric elements was placed on the maximum stress produced. This is to allow maximum coupling between piezoelectric elements and mechanical structure.

The fabrication technique for free-standing diaphragm structure is more complicated compared to previously fabricated cantilever and encastre beam structure. This is due to all sides of the diaphragm being fixed to the substrate. However, by introducing side walls and outlets, the sacrificial layer is able to be removed. Thus, a free-standing diaphragm structure with piezoelectric elements is achieved. Another advantage of screen-printing technology is the simplicity of the process and design. Four types of different diaphragm designs were obtained by only changing the design of the top electrodes.

The free-standing diaphragm structure was tested and had successfully demonstrated the highest SPL level of 74 decibel between 12 kHz to 19 kHz with 15mm microphone distance from circular diaphragm structure. The same experiment was conducted using commercially available piezoelectric buzzer and the SPL level was 128 decibel between 3 kHz to 5 kHz. These frequencies were selected as human hearing capabilities are sensitive between 4 kHz to 5 kHz.

This work had shown that screen-printed free-standing diaphragm structure with piezoelectric elements can be achieved on fabric during garment manufacture. It may be possible in future to improve the design to suit the maximum human hearing frequency range and use a higher $d_{33}$ piezoelectric elements. This application can be implemented as alarm system fabricated directly on fabric.

# 7. Conclusion and future work

## 7.1 Conclusion

The objective of the research is to evaluate varieties of free-standing structure using screen-printable materials which are low temperature process and compatible with fabrics. Three structures were successfully fabricated which were cantilever, encastre beam and diaphragm. Each of the structure was tested with different applications to show the possibilities of the process. These have been achieved, and specifically the following technical areas have been investigated in detail:

- Compatibility evaluation between two types of sacrificial material with structural material.
- Demonstrated the feasibility of the process by fabricating three free-standing structures which were cantilever, encastre beam and diaphragm.
- Evaluated the free-standing piezoelectric cantilever device for the application of energy harvesting.
- Preliminary results for encastre beam and diaphragm structure.

The main results and conclusion will be explained in more details in following subsections.

### 7.1.1 Materials and process compatibility

The compatibility between each materials, substrate and also with the process is essential in order to fabricate free-standing structures on fabric. In this research, four types of commercially available structural materials were investigated. The mechanical properties of each materials were tested using indentation method which result in structural material 1 (SU8) and structural material 2 (Minico M 7000) were selected. Structural material 1 had a Young's modulus of 2692 MPa while the modulus of structural material 2 was two times higher with 5523 MPa. A stiff structural material is required in this process as this layer will be the main structure of the design.

Structural material 1 and structural material 2 were then investigated together with two potential sacrificial materials. The sacrificial materials investigated were denoted sacrificial 1 and sacrificial 2 and these were removed using thermal and water based processes respectively. The evaluation on both sacrificial materials on fabric showed the sacrificial 2 (water removed) are more suitable and compatible with both structural materials. Printing pattern definition as small as 500µm was easily achieved without any misalignment. However, when cured at temperature higher than 120ºC, it caused high gas pressure underneath the structural layer which resulted in a rough structural layer surface after the curing process.

The sacrificial 1 (thermally removed) on the other hand, showed chemical reactions with structural material 2 which resulted in the structural layer adhereing to the substrate but no reaction occurred with structural material 1. However, some residues of sacrificial layer 1 were observed after the removal process. The sacrificial 1 had poor pattern definition with wavy edge especially on small printed structure (500µm line).

From the evaluation, the combination between structural material 2 (Minico M 7000) and sacrificial material 2 (water removed) are selected. As there is no reaction between both materials, the temperature process is compatible with fabric and is able to fabricate with screen-printing method.

### 7.1.2 Device fabrication

The integration of screen-printing and surface micromachining concept allows these free-standing structures to be achieved. The simplicity of the screen-printing process allows design freedom and the capability to produce arrays of printed device simultaneously enabling mass production. It also provides a cost effective approached compared to conventional MEMS fabrication which need clean room facilities. Though, this technique is not a replacement for conventional silicon MEMS and e-textile such as knitting or weaving techniques, it offers a unique fabrication process which could not be achieved by other methods.

In general, the fabrication process started with the preparation of the substrate. A polyester cotton or a Kapton sheet was cut and glued according to the desired alumina tiles and placed on the substrate holder on the screen-printer machine. Then, the paste was loaded on top of the screen with an appropriate gap. A stainless steel flood blade on the screen-printer would spread the paste over the screen. A polyurethane printing squeegee was then applied with appropriate pressure and speed to force the paste through the opening areas of the design. The printing process should provide a complete pattern on the substrate. Finally, the screen was lifted off from the substrate, leaving the printed pattern behind. The substrate was then dried at appropriate temperature and the printing processes were repeated until the desired thickness were achieved.

### 7.1.3 Device evaluation

The objective of this work is to successfully fabricate a free-standing piezoelectric devices with different structures using only screen-printing method. Three different boundary conditions of structure were selected to demonstrate the feasibility of the screen-printing process. Each of the structures represented different possibility of applications and demonstrated the diversity of the process.

The first structure demonstrated was a free-standing piezoelectric cantilever device. The cantilever was 11 mm long and 4 mm wide with one end of the structure was fixed on the substrate. The cantilever device was tested as an energy harvester on fabric and the results showed that the natural frequency of the cantilever was 1544 Hz which was considered too high. A tungsten mass was then added to improve the coupling between the structure and the piezoelectric element. The natural frequency was successfully reduced to 201 Hz with a power output of 13.9 nW at acceleration of 8.829 $m/s^2$. Low frequency application (<250 Hz) is important for the device to work in applications such as handheld tools, car compartment and refrigerator which are possible vibration sources.

The second structure implemented using screen-printed free-standing process was an encastre beam or a bridge structure. The device was fabricated in the same size as cantilever with an air gap of 119μm, created by selectively removing the sacrificial layer. A sandwiched piezoelectric elements were placed on both end of the encastre beam as illustrated in chapter 5. The encastre beam was intended to work as a piezoelectric excitation and detection device. A preliminary test was conducted on each side of piezoelectric elements using the electromechanical shaker and the maximum output generated was 0.1545 volt at natural frequency of 3.835 kHz. Thus, conforming the piezoelectric elements were working. The evaluation was then continued by testing the encastre beam in air and vacuum pressure as the excitation and detection device. However, the resonant frequency for both test was not visible. No response was detected, possibly because the excitation part did not vibrate as expected. Alternatively, it might be due to the boundary condition shifting from free-standing piezoelectric side to the structure layer part, which had resulted in no vibration on piezoelectric elements.

The third structure fabricated using screen-printing method was a free-standing piezoelectric diaphragm. Two structures which are circle and square diaphragms were presented. The fabrication and removal process of these structures were more complicated as all peripheries were fixed. A side wall with a small outlet was introduced in order to allow the sacrificial layer to be removed. Different designs of top electrode produced varieties of diaphragm simultaneously. The diaphragm structure was tested in an anechoic room to demonstrate its application as a sounder. The results showed the sound pressure level at 5 kHz for both circle and square diaphragm was about 58 dB. However, the sound pressure level increased dramatically between 12 kHz to 19 kHz. A comparison experiment was also conducted with commercially available piezoelectric buzzer. The result shows that the commercial buzzer had higher sound pressure level (128 dB) focusing on human hearing frequency which is between 3 kHz to 5 kHz.

## 7.2 Contributions of the research

### 7.2.1 Statement of novelty

The outcome of this research work had demonstrated the following improvements over the state-of-the-art:

- Identification of and improved structural material which is compatible with fabric, the process and other materials (Section 3.4).
- Evaluation and comparison of two potential sacrificial materials with the structure layer. Identified the strength and weakness of each sacrificial material (Section 3.3).
- Identify the optimum printing parameters for the structural material to achieve a cantilever (Chapter 4), encastre beam (Chapter 5) and diaphragm structure (Chapter 6).
- Demonstrated a fully screen-printed free-standing piezoelectric cantilever on fabric for use in an energy harvesting application (Chapter 4).
- Successfully fabricated a free-standing encastre beam on kapton (Chapter 5).
- Using the fabrication method to obtain the first reported fully screen-printed free-standing diaphragm on fabric and presented the preliminary result of the device (Chapter 6).

### 7.2.2 Publications resulted from this research

N. Jamel, D. Zhu, A. Almusallam, R. Torah, K. Yang, S. P. Beeby, *et al.*, "Screen Printed Free-standing Resonator with Piezoelectric Excitation and Detection on Flexible Substrate," *Procedia Engineering,* vol. 87, pp. 947-950, 2014.
DOI:10.1016/j.proeng.2014.11.313

Nursabirah Jamel, Ahmed Almusallam, Dibin Zhu, Russel Torah, Kai Yang, John Tudor, *et al.*, "Screen-printed free-standing piezoelectric devices using low temperature process," presented at the Design, Test, Integration and Packaging of MEMS/MOEMS (DTIP),IEEE Conference Publications, Pages 1- 4 2015. DOI: 10.1109/DTIP.2015.7160968

## 7.3 Future work

The experimental results presented in this thesis demonstrated the screen-printing process incorporated with piezoelectric material and sacrificial layer to produce the free-standing structures. Three potential applications had successfully presented with different structure. However, there is still room of improvement especially in terms of piezoelectric material used and devices design so that the devices are more application specified.

### 7.3.1 Materials evaluation

The evaluations conducted in chapter 3 showed that structural material 2 is compatible with the process and other material used in screen-printing. However, the curing temperature of the structural material affected the removal process of sacrificial layer. Therefore, UV curable structural material with a rapid curing process and higher mechanical stiffness (>5500 MPa) are more desirable. A more active polymer PZT with a higher $d_{33}$ value will also improve the output of devices implemented. This could be achieved by implementing isostatic pressing to the printed structure to decrease the porosity of printed PZT layer hence increasing the $d_{33}$ value.

### 7.3.2 Screen-printed free-standing piezoelectric cantilever optimisation

Screen-printing a multilayer piezoelectric can further improved the electrical output of the device. Evaluations of different sizes of cantilever will also broaden the operation bandwidth, hence, increasing the possibility of the device to work in desire frequency. Long term evaluation of the device will allow better understanding in terms of performance and capability of the device as energy harvesting on fabric.

### 7.3.3 Design improvement of encastre beam

In chapter 5, an encastre beam with piezoelectric printed on both side had been tested. However, the device did not work possibly because the excitation part did not excite sufficient amplitude in the beam. The improvement that can be implemented is by increasing the size of the piezoelectric pad on both excitation and detection part. The size of piezoelectric pad should cover between the maximum stress produced by the simulation and the free-standing structure area. Alternatively, it might be due to the presence of the piezoelectric elements altering the boundary conditions of the beam. The clamping point on the beam could move due to the presence of the piezoelectric layer. The added stiffness caused by the addition of the piezoelectric element could cause the effective clamping point to move to the edge of the piezoelectric element. This would result in greatly reduced levels of vibration at the locations of the piezoelectric elements. This could be improved by using more flexible piezoelectric material or higher $d_{33}$ values of piezoelectric materials. In addition, an encapsulation of the whole device will prevent the device from damage and possibly reduce the noise introduced by the wires connection.

### 7.3.4 Diaphragm piezoelectric and design improvement

As demonstrated in chapter 6, the free-standing piezoelectric diaphragms were successfully fabricated. However, the sound pressure level of the device was not focusing on human sensitive frequency range which is from 2 kHz up to 5 kHz. By designing the diaphragm in this range, a piezoelectric buzzer on fabric could be achieved. Furthermore, implementing a piezoelectric material which is compatible with the process and also has a higher $d_{33}$ could possibly increase the sound pressure level of the device, hence, broadening the application of free-standing piezoelectric diaphragm as an alarm system which integrated directly on fabric.

# Appendix 1:

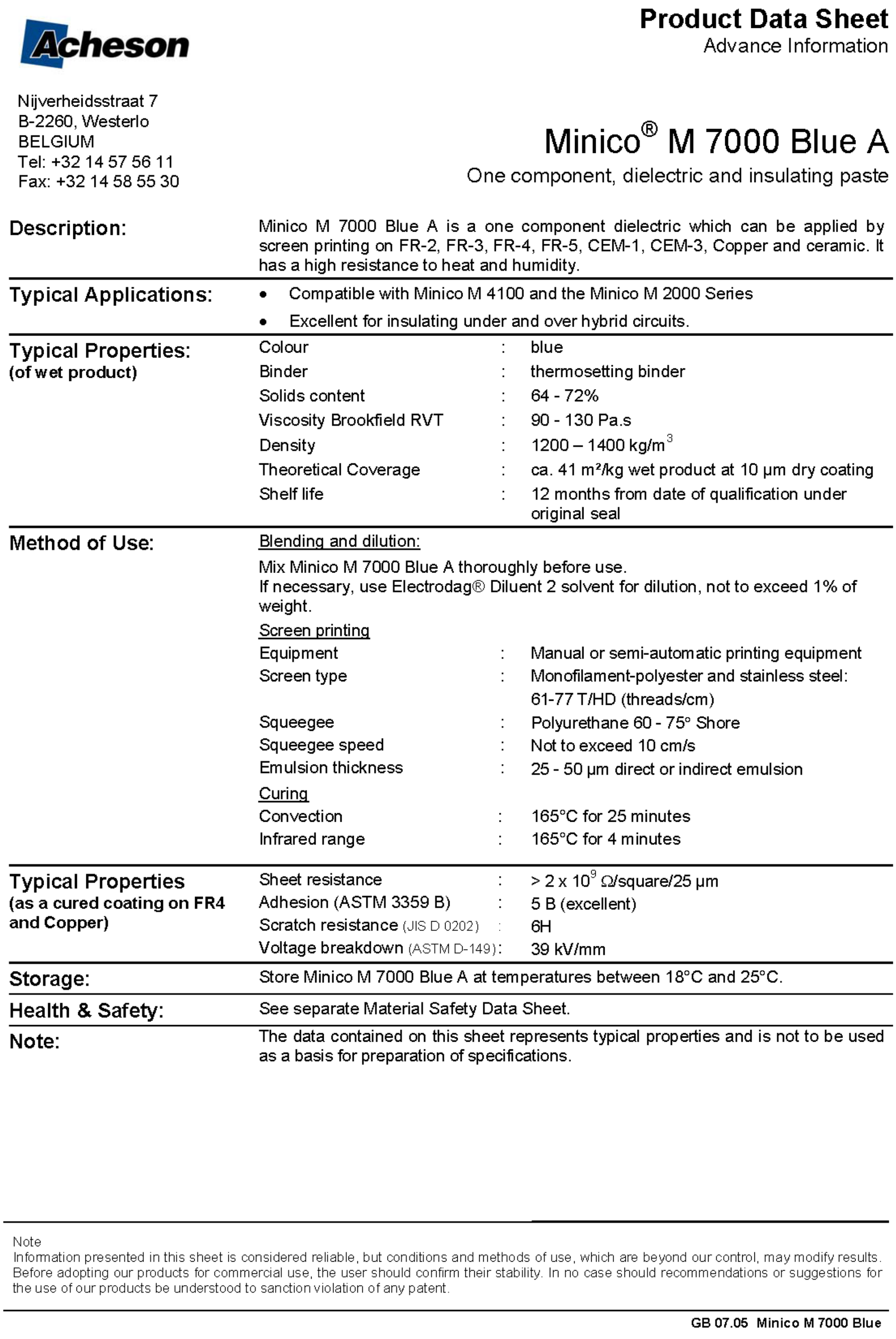

Acheson

## Product Data Sheet
Advance Information

Nijverheidsstraat 7
B-2260, Westerlo
BELGIUM
Tel: +32 14 57 56 11
Fax: +32 14 58 55 30

## Minico® M 7000 Blue A
One component, dielectric and insulating paste

**Description:**

Minico M 7000 Blue A is a one component dielectric which can be applied by screen printing on FR-2, FR-3, FR-4, FR-5, CEM-1, CEM-3, Copper and ceramic. It has a high resistance to heat and humidity.

**Typical Applications:**

- Compatible with Minico M 4100 and the Minico M 2000 Series
- Excellent for insulating under and over hybrid circuits.

**Typical Properties:**
**(of wet product)**

Colour : blue
Binder : thermosetting binder
Solids content : 64 - 72%
Viscosity Brookfield RVT : 90 - 130 Pa.s
Density : 1200 – 1400 kg/m$^3$
Theoretical Coverage : ca. 41 m²/kg wet product at 10 µm dry coating
Shelf life : 12 months from date of qualification under original seal

**Method of Use:**

Blending and dilution:

Mix Minico M 7000 Blue A thoroughly before use.
If necessary, use Electrodag® Diluent 2 solvent for dilution, not to exceed 1% of weight.

Screen printing

Equipment : Manual or semi-automatic printing equipment
Screen type : Monofilament-polyester and stainless steel: 61-77 T/HD (threads/cm)
Squeegee : Polyurethane 60 - 75° Shore
Squeegee speed : Not to exceed 10 cm/s
Emulsion thickness : 25 - 50 µm direct or indirect emulsion

Curing

Convection : 165°C for 25 minutes
Infrared range : 165°C for 4 minutes

**Typical Properties**
**(as a cured coating on FR4 and Copper)**

Sheet resistance : > 2 x $10^9$ Ω/square/25 µm
Adhesion (ASTM 3359 B) : 5 B (excellent)
Scratch resistance (JIS D 0202) : 6H
Voltage breakdown (ASTM D-149): 39 kV/mm

**Storage:**

Store Minico M 7000 Blue A at temperatures between 18°C and 25°C.

**Health & Safety:**

See separate Material Safety Data Sheet.

**Note:**

The data contained on this sheet represents typical properties and is not to be used as a basis for preparation of specifications.

**GB 07.05 Minico M 7000 Blue**

# Appendix 2:

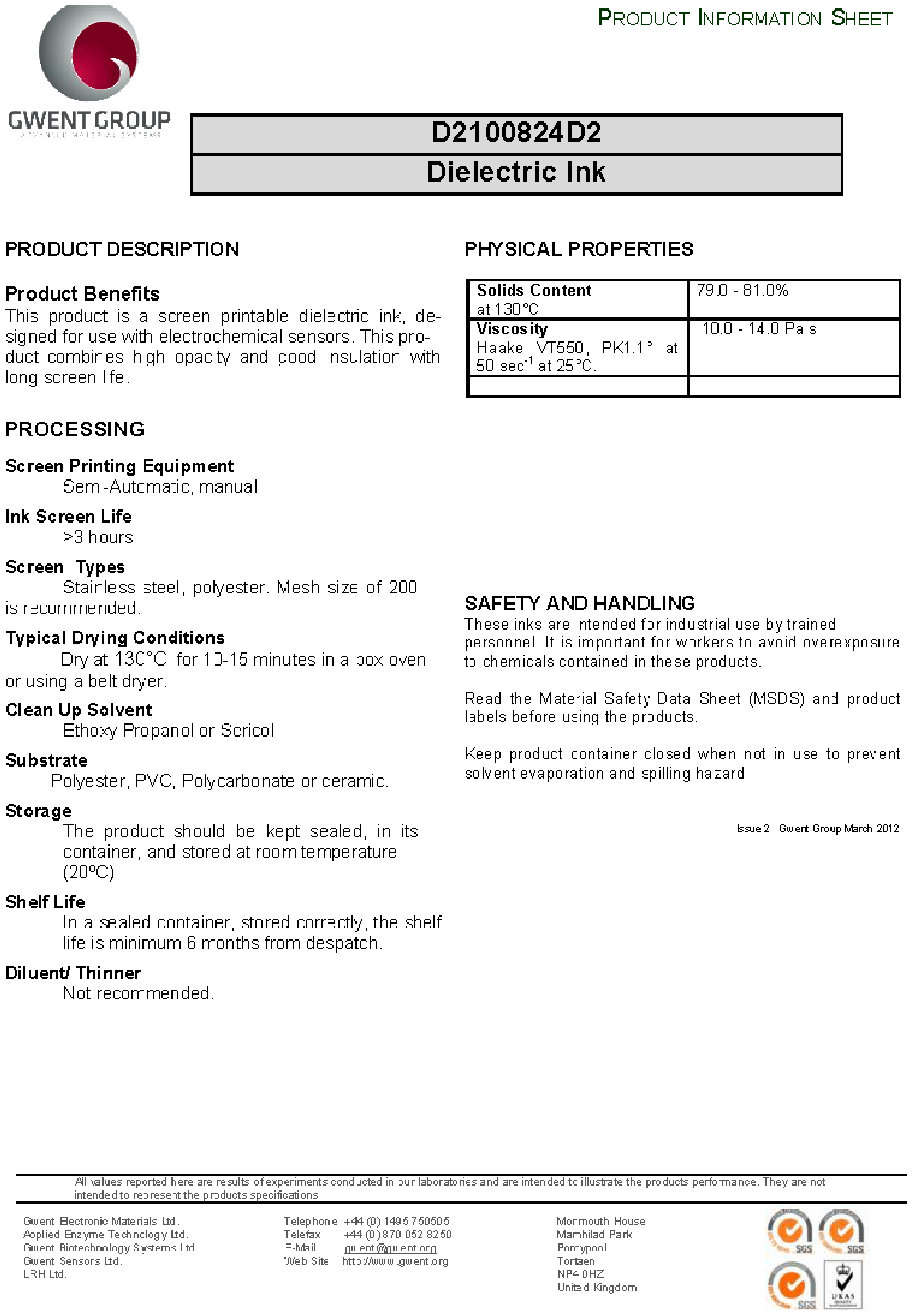

PRODUCT INFORMATION SHEET

## D2100824D2

## Dielectric Ink

### PRODUCT DESCRIPTION

**Product Benefits**
This product is a screen printable dielectric ink, designed for use with electrochemical sensors. This product combines high opacity and good insulation with long screen life.

### PROCESSING

**Screen Printing Equipment**
Semi-Automatic, manual

**Ink Screen Life**
>3 hours

**Screen Types**
Stainless steel, polyester. Mesh size of 200 is recommended.

**Typical Drying Conditions**
Dry at 130°C for 10-15 minutes in a box oven or using a belt dryer.

**Clean Up Solvent**
Ethoxy Propanol or Sericol

**Substrate**
Polyester, PVC, Polycarbonate or ceramic.

**Storage**
The product should be kept sealed, in its container, and stored at room temperature (20°C)

**Shelf Life**
In a sealed container, stored correctly, the shelf life is minimum 6 months from despatch.

**Diluent/ Thinner**
Not recommended.

### PHYSICAL PROPERTIES

| | |
|---|---|
| **Solids Content**<br>at 130°C | 79.0 - 81.0% |
| **Viscosity**<br>Haake VT550, PK1.1° at 50 $sec^{-1}$ at 25°C. | 10.0 - 14.0 Pa s |
| | |

### SAFETY AND HANDLING

These inks are intended for industrial use by trained personnel. It is important for workers to avoid overexposure to chemicals contained in these products.

Read the Material Safety Data Sheet (MSDS) and product labels before using the products.

Keep product container closed when not in use to prevent solvent evaporation and spilling hazard

Issue 2 Gwent Group March 2012

All values reported here are results of experiments conducted in our laboratories and are intended to illustrate the products performance. They are not intended to represent the products specifications

Gwent Electronic Materials Ltd.
Applied Enzyme Technology Ltd.
Gwent Biotechnology Systems Ltd.
Gwent Sensors Ltd.
LRH Ltd.

Telephone +44 (0) 1495 750505
Telefax +44 (0)870 052 8250
E-Mail gwent@gwent.org
Web Site http://www.gwent.org

Monmouth House
Mamhilad Park
Pontypool
Torfaen
NP4 0HZ
United Kingdom

# List of References

[1] M. C. Lina and B. F. Alison, "Smart fabric sensors and e-textile technologies: a review," *Smart Materials and Structures,* vol. 23, 2014.

[2] S. Mann, "Wearable computing: a first step toward personal imaging," *Computer,* vol. 30, pp. 25-32, 1997.

[3] A. Latour. (2000, August 22, 2012). *Philips and Levi Strauss Team Up To Create Ready-to-Wear Electronics*. Available: http://online.wsj.com/article/SB966795198702775516.html#

[4] M. Suh, K. Carroll, and N. Cassill, "Critical Review on Smart Clothing Product Development," *Journal of Textile and Apparel, Technology and Management,* vol. 6, pp. 1-18, 2010.

[5] D. Meoli, "Interactive Electronic Textiles: Technologies, Applications, Opportunities, and Market Potential," Master of Science Thesis, North Carolina State University, Rayleigh, NC, USA, 2002.

[6] VivoMetric. (10 December 2013). *Lifeshirt*. Available: http://www.virtualworldlets.net/Shop/ProductsDisplay/VRInterface.php?ID=49

[7] K. Yongsang, K. Hyejung, and Y. Hoi-Jun, "Electrical Characterization of Screen-Printed Circuits on the Fabric," *Advanced Packaging, IEEE Transactions on,* vol. 33, pp. 196-205, 2010.

[8] S. Ikegami, "CdS/CdTe solar cells by the screen-printing-sintering technique: Fabrication, photovoltaic properties and applications," *Solar Cells,* vol. 23, pp. 89-105, 1// 1988.

[9] T. world. (29 August 2012). *E-Textiles For Wearability: Review Of Integration Technologies*. Available: http://www.textileworld.com/Articles/2010/April/Issue/Etextiles_Feature.html

[10] K. Yang, R. Torah, Y. Wei, S. Beeby, and J. Tudor, "Waterproof and durable screen printed silver conductive tracks on textiles," *Textile research* pp. 1-10, July 12, 2013.

[11] J. M. Bustillo, R. T. Howe, and R. S. Muller, "Surface micromachining for microelectromechanical systems," *Proceedings of the IEEE,* vol. 86, pp. 1552-1574, 1998.

[12] B. Ariyatum, R. Holland, D. Harrison, and T. Kazi, "The future design direction of Smart Clothing development," *Journal of Textile Institute,* pp. 199-212, 2004.

[13] A. Tuck. (2000, 05 december 2013). *The ICD+ jacket*. Available: http://www.independent.co.uk/news/business/analysis-and-features/the-icd-jacket-slip-into-my-office-please-694074.html

[14] E. R. Post and M. Orth, "Smart fabric, or "wearable clothing"," in *Wearable Computers, 1997. Digest of Papers., First International Symposium on*, 1997.

[15] H. Zhang, X. Tao, T. Yu, and S. Wang, "Conductive knitted fabric as large-strain gauge under high temperature," *Sensors and Actuators A: Physical,* vol. 126, pp. 129-140, 2006.

[16] M. Orth, R. Post, and E. Cooper, "Fabric Computing Interfaces," in *Conference Summary on Human Factors in Computing Systems*, New York, US, 1998.

[17] M. Klemm, I. Locher, and G. Troster, "A novel circularly polarized textile antenna for wearable applications," in *Wireless Technology, 2004. 7th European Conference on*, 2004.

[18] H. Shahariar, H. Soewardiman, and J. S. Jur, "Fabrication and packaging of flexible and breathable patch antennas on textiles," in *SoutheastCon 2017*, 2017.

[19] F. Carpi and D. D. Rossi, "Electroactive polymer-based devices for e-textiles in biomedicine," *IEEE Transactions on Information Technology in Biomedicine,* vol. 9, pp. 295-318, 2005.

[20] A. Bonfiglio, D. D. Rossi, T. Kirstein, I. R. Locher, F. Mameli, R. Paradiso, *et al.*, "Organic field effect transistors for textile applications," *IEEE Transactions on Information Technology in Biomedicine,* vol. 9, pp. 319-324, 2005.

[21] R. Wijesiriwardana, K. Mitcham, and T. Dias, "Fibre-meshed transducers based real time wearable physiological information monitoring system," in *Wearable Computers, 2004. ISWC 2004. Eighth International Symposium on*, 2004.

[22] Y. Wei, R. Torah, K. Yang, S. Beeby, and J. Tudor, "Screen printing of a capacitive cantilever-based motion sensor on fabric using a novel sacrificial layer process for smart fabric applications," *Measurement Science and Technology,* vol. 24, pp. 1-12, 2013.

[23] Y. Li, R. Torah, S. Beeby, and J. Tudor, "An all-inkjet printed flexible capacitor on a textile using a new poly(4-vinylphenol) dielectric ink for wearable applications," in *2012 IEEE Sensors*, 2012.

[24] W. Yang, T. Russel, Y. Kai, B. Steve, and T. John, "A novel fabrication process to realize a valveless micropump on a flexible substrate," *Smart Materials and Structures,* vol. 23, 2014.

[25] M. d. Vos, R. Torah, and J. Tudor, "A novel pneumatic dispenser fabrication technique for digitally printing electroluminescent lamps on fabric," in *2015 Symposium on Design, Test, Integration and Packaging of MEMS/MOEMS (DTIP)*, 2015.

[26] A. O. Komolafe, R. N. Torah, K. Yang, J. Tudor, and S. P. Beeby, "Durability of screen printed electrical interconnections on woven textiles," in *2015 IEEE 65th Electronic Components and Technology Conference (ECTC)*, 2015.

[27] G. Cai, M. Yang, Z. Xu, J. Liu, B. Tang, and X. Wang, "Flexible and wearable strain sensing fabrics," *Chemical Engineering Journal,* vol. 325, pp. 396-403,2017.

[28] I. Jeerapan, J. R. Sempionatto, A. Pavinatto, J.-M. You, and J. Wang, "Stretchable biofuel cells as wearable textile-based self-powered sensors," *Journal of Materials Chemistry A,* vol. 4, pp. 18342-18353, 2016.

[29] A. Almusallam, R. N. Torah, D. Zhu, M. J. Tudor, and S. P. Beeby, "Screen-printed piezoelectric shoe-insole energy harvester using an improved flexible PZT-polymer composites," presented at the PowerMEMS, 2013.

[30] Z. Cao, M. J. Tudor, R. N. Torah, and S. P. Beeby, "Screen Printable Flexible BiTe-SbTe-Based Composite Thermoelectric Materials on Textiles for Wearable Applications," *IEEE Transactions on Electron Devices,* vol. 63, pp. 4024-4030, 2016.

[31] P. Gordon, T. Russel, Y. Kai, B. Steve, and T. John, "An investigation into the durability of screen-printed conductive tracks on textiles," *Measurement Science and Technology,* vol. 25, p. 025006, 2014.

[32] Y. Wei, R. Torah, K. Yang, S. Beeby, and J. Tudor, "Screen Printed Capacitive Free-standing Cantilever Beams used as a Motion Detector for Wearable Sensors," *Procedia Engineering,* vol. 47, pp. 165-169,2012.

[33] B. Karaguzel, "Printing Conductive Inks on Nonwovens: Challenges and Opportunities," Fiber and polymer science, North Carolina State University, Raleigh, North Carolina, 2006.

[34] E. R. Post, M. Orth, P. R. Russo, and N. Gershenfeld, "E-broidery: Design and fabrication of textile-based computing," *IBM System Journal,* vol. 39, 2000.

[35] J. J. Licari and L. R. Enlow. (1998). *Hybrid Microcircuit Technology Handbook (2nd Edition)*. Available: http://www.knovel.com/web/portal/browse/display?_EXT_KNOVEL_DISPLAY_bookid=388

[36] S. Datta, K. Keller, D. L. Schulz, and D. C. Webster, "Conductive Adhesives From Low-VOC Silver Inks for Advanced Microelectronics Applications," *Components, Packaging and Manufacturing Technology, IEEE Transactions on,* vol. 1, pp. 69-75, 2011.

[37] N. M. White, N. R. Harris, K. Swee Leong, and M. J. Tudor, "Novel thick-film piezoceramic micro-generator based on free-standing structures," in *Electronics System-Integration Technology Conference, 2008. ESTC 2008. 2nd*, 2008.

[38] J. J. Sniegowski and M. S. Rodgers, "Multi-layer enhancement to polysilicon surface-micromachining technology," in *Electron Devices Meeting, 1997. IEDM '97. Technical Digest., International*, 1997.

[39] A. Partridge, D. Pullen, and D. Allen, "Structural materials," 2009.

[40] H. Debeda, P. Clement, E. Llobet, and C. Lucat, "One-step firing for electroded PZT thick films applied to MEMS," *Smart Materials and Structures,* vol. 24, p. 8,2015.

[41] S. L. Kok, A. R. Othman, and A. Shaaban, "Screen-Printed Ceramic Based MEMS Piezoelectric Cantilever for Harvesting Energy," *Advances in Science and Technology,* vol. 90, pp. 84-92,2014.

[42] S. L. Kok, "Design, fabrication and characterisation of freestanding thick-film piezoelectric cantilevers for energy harvesting," Doctor of Philosophy, University of Southampton, 2010.

[43] R. Lakhmi, H. Debeda, I. Dufour, and C. Lucat, "Force Sensors Based on Screen-Printed Cantilevers," *Sensors Journal, IEEE,* vol. 10, pp. 1133-1137, 2010.

[44] C. B. Sippola and C. H. Ahn, "A hermetic thick film screen-printed ceramic cavity for harsh environment sensing applications," *Ieee Transactions on Components and Packaging Technologies,* vol. 30, pp. 439-443, 2007.

[45] A. Rivadeneyra, J. Fernández-Salmerón, M. Agudo-Acemel, J. A. López-Villanueva, L. F. Capitan-Vallvey, and A. J. Palma, "Improved manufacturing process for printed cantilevers by using water removable sacrificial substrate," *Sensors and Actuators A: Physical,* vol. 235, pp. 171-181,2015.

[46] K. Yang, R. Torah, Y. Wei, S. Beeby, and J. Tudor, "Water based PVA sacrificial material for low temperature MEMS fabrication and applications on e-textiles," presented at the Eurosensors, 2014.

[47] N. Serra, T. Maeder, C. Jacq, Y. Fournier, and P. Ryser, "Screen-printed polymer-based microfluidic and micromechanical devices based on evaporable compounds," in *Microelectronics and Packaging Conference, 2009. EMPC 2009. European*, 2009.

[48] Y. Wei, R. Torah, K. Yang, S. Beeby, and J. Tudor, "A Novel Fabrication Process to Realise Piezoelectric Cantilever Structures for Smart Fabric Sensor Applications," 2012.

[49] C. Lucat, P. Ginet, C. Castille, H. Debéda, and F. Ménil, "Microsystems elements based on free-standing thick-films made with a new sacrificial layer process," *Microelectronics Reliability,* vol. 48, pp. 872-875, 2008.

[50] Y. Wei, R. Torah, K. Yang, S. Beeby, and J. Tudor, "A novel fabrication process for capacitive cantilever structures for smart fabric applications," *Symposium on Design, Test, Integration & Packaging of MEMS/MOEMS 2012, Cannes,* 2012.

[51] H. Debéda, R. Lakhmi, C. Lucat, and I. Dufour, "Use of the longitudinal mode of screen-printed piezoelectric cantilevers coated with PEUT for toluene detection: Comparison with silicon cantilevers," *Sensors and Actuators B: Chemical,* vol. 187, pp. 198-203,2013.

[52] C. B. Sippola and H. A. Chong, "A thick film screen-printed ceramic capacitive pressure microsensor for high temperature applications," *Micromechanics and Microengineering,* vol. 16, pp. 1086-1091, 2006.

[53] C. B. Sippola and C. H. Ahm, "A ceramic capacitive pressure microsensor with screen-printed diaphragm," in *Sensors, 2005 IEEE*, 2005.

[54] H.-B. Fang, J.-Q. Liu, Z.-Y. Xu, L. Dong, L. Wang, D. Chen*, et al.*, "Fabrication and performance of MEMS-based piezoelectric power generator for vibration energy harvesting," *Microelectronics Journal,* vol. 37, pp. 1280-1284,2006.

[55] R. Xu, A. Lei, C. Dahl-Petersen, K. Hansen, M. Guizzetti, K. Birkelund*, et al.*, "Screen printed PZT/PZT thick film bimorph MEMS cantilever device for vibration energy harvesting," *Sensors and Actuators A: Physical,* vol. 188, pp. 383-388,2012.

[56] T. Zawada, K. Hansen, R. Lou-Moeller, E. Ringgaard, T. Pedersen, and E. V. Thomsen, "High-performance piezoelectric thick film based energy harvesting micro-generators for MEMS," *Procedia Engineering,* vol. 5, pp. 1164-1167,2010.

[57] P. h. Wang, S. w. Shi, and H. j. Du, "Fabrication and performance of ZnO piezoelectric cantilever for vibration energy harvesting," in *Piezoelectricity, Acoustic Waves, and Device Applications (SPAWDA), 2015 Symposium on*, 2015.

[58] D. Zhu, "Vibration Energy Harvesting: Machinery Vibration, Human Movemnet and Flow Induced Vibration," in *Sustainable Energy Harvesting Technologies - Past, Present and Future*, Y. K. Tan, Ed., ed. InTech, 2011.

[59] G. Zhang, V. Chu, and J. P. Conde, "Conductive Blended Polymer MEMS Microresonators," *Journal of Microelectromechanical Systems,* vol. 16, pp. 329-335, 2007.

[60] J. Olivares, E. Iborra, M. Clement, L. Vergara, J. Sangrador, and A. Sanz-Hervás, "Piezoelectric actuation of microbridges using AlN," *Sensors and Actuators A: Physical,* vol. 123–124, pp. 590-595,2005.

[61] Y. Mafinejad, A. Z. Kouzani, M. Nassabi, Y. Lim, and K. Mafinezhad, "Characterization and optimization to improve uneven surface on MEMS bridge fabrication," *Displays,* vol. 37, pp. 54-61,2015.

[62] R. Dejaeger, F. Casset, B. Desloges, G. Le Rhun, P. Robert, S. Fanget*, et al.*, "Development and Characterization of a Piezoelectrically Actuated MEMS Digital Loudspeaker," *Procedia Engineering,* vol. 47, pp. 184-187, 2012.

[63] W. S. Lee and S. S. Lee, "Piezoelectric microphone built on circular diaphragm," *Sensors and Actuators A: Physical,* vol. 144, pp. 367-373, 2008.

[64] P. J. Holmes and R. G. Loasby, *Handbook of Thick Film technology*: Electrochemical Publication Limited, 1976.

[65] K. P. Materials. (July). *Kapton polymide film*. Available: http://www.katco.eu/kapton.htm

[66] BBC. (June ). *GCSE Bitesize : Fabrics*. Available: http://www.bbc.co.uk/schools/gcsebitesize/design/textiles/fabricsrev1.shtml

[67] A. Komolafe, "Reliability and interconnections for printed circuits on fabrics," Doctoral Thesis, Faculty of Physical Sciences and Engineering, Univeristy of Southampton, Southampton, 2016.

[68] J. Timmermans, "Plastic crystals: A historical review," *Journal of Physics and Chemistry of Solids,* vol. 18, pp. 1-8, 1961.

[69] V. Goodship, *Rapra Review Reports : Polyvinyl Alcohol : Materials, Processing and Application (1)*. Shrewsbury, US: iSmithers Rapra Publishing, 2009.

[70] J.-H. Feng and F. Dogan, "Aqueous processing and mechanical properties of PLZT green tapes," *Materials Science and Engineering: A,* vol. 283, pp. 56-64,2000.

[71] J. Lenz and A. S. Edelstein, "Magnetic sensors and their applications," *Sensors Journal, IEEE,* vol. 6, pp. 631-649, 2006.

[72] Y. Yuan and T. R. Lee, "Contact Angle and Wetting Properties," in *Surface Science Techniques*, G. Bracco and B. Holst, Eds., ed Berlin, Heidelberg: Springer Berlin Heidelberg, 2013.

[73] A. Rudawska and E. Jacniacka, "Analysis for determining surface free energy uncertainty by the Owen–Wendt method," *International Journal of Adhesion and Adhesives,* vol. 29, pp. 451-457,2009.

[74] C. Y. Poon and B. Bhushan, "Comparison of surface roughness measurements by stylus profiler, AFM and non-contact optical profiler," *Wear,* vol. 190, pp. 76-88,1995.

[75] T. R. Thomas, *Rough surfaces*: Imperial College Press, 1982.

[76] K. E. Petersen, "Silicon as a mechanical material," *Proceedings of the IEEE,* vol. 70, pp. 420-457, 1982.

[77] D. Westberg, O. Paul, G. I. Andersson, and H. Baltes, "Surface micromachining by sacrificial aluminium etching," *Journal of Micromechanics and Microengineering,* vol. 6, pp. 376-384,1996.

[78] V. Linder, B. D. Gates, D. Ryan, B. A. Parviz, and G. M. Whitesides, "Water-Soluble Sacrificial Layers for Surface Micromachining," *Small,* vol. 1, pp. 730-736, 2005.

[79] N. Ferrell, J. Woodard, and D. Hansford, "Fabrication of polymer microstructures for MEMS:sacrificial layer micromolding and patterned substrate micromolding," *Biomed Microdevices,* 2007.

[80] L. Kiesewetter, J. M. Zhang, D. Houdeau, and A. Steckenborn, "Determination of Young's moduli of micromechanical thin films using the resonance method," *Sensors and Actuators A: Physical,* vol. 35, pp. 153-159, 1992.

[81] "Plastics — Determination of tensile properties," ed, May 1996.

[82] X. Li and B. Bhushan, "A review of nanoindentation continuous stiffness measurement technique and its applications," *Materials Characterization,* vol. 48, pp. 11-36, 2002.

[83] K. E. Petersen and C. R. Guarnieri, "Young's modulus measurements of thin films using micromechanics," *Journal of Applied Physics,* vol. 50, pp. 6761-6766, 1979.

[84] A. D. Campo and C. Greiner, "SU-8: a photoresist for high-aspect-ratio and 3D submicron lithography," *Journal of Micromechanics and Microengineering,* vol. 17, pp. R81-R95, 2007.

[85] H. Lorenz, M. Despont, N. Fahrni, N. LaBianca, P. Renaud, and P. Vettiger, "SU-8: a low-cost negative resist for MEMS," *Journal of Micromechanics and Microengineering,* vol. 7, pp. 121-124, 1997.

[86] M. S. Chemicals. (2001, January). *EPON RESIN SU8 DATA SHEET*. Available: http://www.momentive.com/Products/TechnicalDataSheet.aspx?id=3603

[87] M. Mionic, "Preparation and Physical Characterization of Carbon Nanotubes-SU8 Composites," Doctoral studies, 2011.

[88] J. Zhang, M. B. Chan-Park, and C. M. Li, "Network properties and acid degradability of epoxy-based SU-8 resists containing reactive gamma-butyrolactone," *Sensors and Actuators B: Chemical,* vol. 131, pp. 609-620, 2008.

[89] J. J. Bernstein, J. Bottari, K. Houston, G. Kirkos, R. Miller, B. Xu*, et al.*, "Advanced MEMS ferroelectric ultrasound 2D arrays," in *Ultrasonics Symposium, 1999. Proceedings IEEE*, 1999.

[90] A. Almusallam, K. Yang, D. Zhu, R. N. Torah, A. Komolafe, J. Tudor*, et al.*, "Clamping effect on the piezoelectric responses of screen-printed low temperature PZT/Polymer films on flexible substrates," *Smart Materials and Structures,* vol. 24, p. 115030, 2015.

[91] Q.M. Wang, Q. Zhang, B. Xu, R. Liu, and L. E. Cross, "Nonlinear piezoelectric behavior of ceramic bending mode actuators under strong electric fields," *Journal of Applied Physics,* vol. 86, pp. 3352-3360, 1999.

[92] M. J. Tudor and S. P. Beeby, "Resonant sensors: Fundamentals and state of the art," *Sensor and materials,* vol. 9, pp. 1.-15, 1997.

[93] F. R. Blom, S. Bouwstra, J. H. J. Fluitman, and M. Elwenspoek, "Resonating silicon beam force sensor," *Sensors and Actuators,* vol. 17, pp. 513-519, 1989.

[94] G. Stemme, "Resonant silicon sensors," *Journal of Micromechanics and Microengineering,* vol. 1, 1991.

[95] S. Beeby, G. Ensel, and M. Kraft, *MEMS Mechanical Sensors*. Norwood, MA, USA: Artech House, 2004.